



**Politecnico  
di Torino**

## Politecnico di Torino

Master's degree in Automotive Engineering

A.y. 2024/2025

Graduation Session March 2025

# **Improving automated driving performance through in-depth vehicle dynamics stability analysis.**

**Supervisor :**

Prof. Enrico Galvagno

Eng. Luca Zerbato

**Candidate:**

Enrico Zebito



*A nonna Lucia esempio di amore puro ed incondizionato.*

*A nonno Franco esempio di onestà e professionalità.*

# Abstract

The future of driving systems is strongly oriented towards autonomous driving, and consequently, safety control systems aimed at ensuring the safety of the driver, passengers, and the surrounding environment are becoming increasingly present in modern vehicles. At the core of these systems is the necessary and solid development of cutting-edge control systems, but equally important is the understanding of the dynamics of the system to be controlled, which is crucial for achieving safety objectives. In this regard, the work developed within this document aims to study the dynamics of road vehicles, specifically their characterization in both linear and non-linear domains, by examining the effects that various parameters have on axle characteristics and, therefore, on the stability zone. The challenge in defining such zones lies precisely in the non-linear nature of the system under consideration. The basic approach has been to conduct simulations and develop a robust method for defining the stability and instability zones as vehicle operating conditions change, with the goal of defining stability maps on the phase plane and implementing them within a vehicle model equipped with a model-based predictive controller for complex autonomous driving scenarios in highway environments.



## Abstract in Italiano

Il futuro dei sistemi di guida è fortemente proiettato verso la guida autonoma e conseguentemente sempre più presenti nei veicoli moderni sono i sistemi di controllo mirati alla sicurezza del conducente, dei passeggeri e dell'ambiente circostante. Alla base di questi sistemi c'è sicuramente una necessaria e solida capacità di sviluppo di sistemi di controllo sempre più all'avanguardia, ma non solo, la conoscenza della dinamica del sistema che si intende controllare è di altrettanta importanza per la riuscita dell'obiettivo di sicurezza. A tal proposito il lavoro sviluppato all'interno di questo documento si prefigge di studiare la dinamica dei veicoli stradali, in particolare della loro caratterizzazione sia in campo lineare che non lineare, attraverso lo studio degli effetti che svariati parametri hanno sulle caratteristiche degli assi e dunque sulla zona di stabilità. La difficoltà nella definizione di tali zone sta proprio nella natura non lineare del sistema in esame. L'approccio di base è stato quello di condurre simulazioni e di sviluppare un metodo solido per la definizione delle zone di stabilità e di instabilità al variare delle condizioni di esercizio del veicolo con l'obiettivo di definire delle mappe di stabilità sul piano delle fasi e di implementarle all'interno di un modello di veicolo dotato di un controllore predittivo basato su modelli di veicolo per scenari complessi di guida autonoma in ambiente autostradale.



# Contents

<b>Abstract</b> .....	<b>iii</b>
<b>Abstract in Italiano</b> .....	<b>v</b>
<b>Contents</b> .....	<b>vii</b>
<b>Introduction</b> .....	<b>11</b>
Structure of the thesis.....	14
Methodology .....	16
Document Outline .....	17
<b>1 Vehicle Models and Tools</b> .....	<b>18</b>
1.1. Vehicle Models .....	18
1.1.1. Single-track model .....	18
1.1.2. Single-track model: Linearization around its fixed points.....	21
1.1.3. Double-track model .....	25
1.1.4. Vehicle model and Controller .....	29
1.2. Tools.....	32
1.2.1. Map-based Axial Cornering Stiffness tool .....	32
1.2.2. Phase Portrait and Bifurcation Analysis.....	35
<b>2 Vehicle Characterization</b> .....	<b>39</b>
2.1. Vehicle Data .....	39
2.2. Type of manoeuvres .....	40
2.3. Ramp Steer .....	40
2.3.1. Vehicle's responses .....	41
2.3.2. Lateral Force and Cornering Stiffness.....	42
2.3.3. Steady State Turning .....	44
2.3.4. Gain .....	47
2.4. Cornering stiffness linearization around a fixed point. ....	49
2.5. Impact of road inclination on lateral dynamic. ....	56
2.5.1. Implementation within the vehicle model. ....	56
2.5.2. Effects on Critical Speed .....	57
2.5.3. Effect of negative slopes.....	59
2.5.4. Effect on an Understeering vehicle.....	62

2.6.	Impact of longitudinal acceleration on lateral dynamic.....	64
2.6.1.	Implementation within the vehicle model. ....	64
2.6.2.	Effect on cornering stiffness .....	64
2.6.3.	Combined effect of negative acceleration and negative road inclination.....	67
2.7.	Impact of friction coefficient on lateral dynamic.....	68
2.8.	Characteristic of the axles through the tire model .....	72
2.8.1.	Results.....	72
2.8.2.	Longitudinal Slip.....	76
2.8.3.	Toe Angle .....	77
2.8.4.	Camber Angle.....	78
2.9.	Yaw Moment Control.....	79
2.9.1.	Objective.....	79
2.9.2.	Method.....	79
<b>3</b>	<b>Phase Plane.....</b>	<b>87</b>
3.1.1.	Bifurcation.....	89
3.2.	Open-Loop Stability region definition.....	95
3.3.	Closed-Loop Stability region definition .....	98
3.3.1.	Method.....	98
3.3.2.	Simulation Scenario .....	98
3.3.3.	Disturbance Implementation.....	99
3.4.	Steering Dynamics .....	101
3.5.	Results: OverSteering Vehicle .....	102
3.5.1.	“Fast steering” Results .....	102
3.5.2.	“Slow Steering” Results .....	104
3.5.3.	Effect of Steering Actuation Delay .....	107
3.5.4.	Comparison of vehicle stability zone in closed loop and open loop	110
3.6.	Results: UnderSteering Vehicle.....	111
3.6.1.	“Fast steering” Results .....	111
3.6.2.	“Slow Steering” Results .....	114
3.6.3.	Effect of Steering Actuation Delay .....	116
3.6.4.	Comparison of vehicle stability zone in closed loop and open loop	117
3.7.	Oversteering vs Understeering .....	118
3.8.	Simulation Scenario: Constant Curved trajectory.....	119
3.8.1.	“Slow Steering” Results .....	120

3.8.2.	Comparison of vehicle stability zone in closed loop and open loop	123
<b>4</b>	<b>Complete Model performance</b>	<b>124</b>
4.1.	Scenario: Straight road double overtaking	124
4.1.1.	Scenario description	124
4.2.	Analysed cases	125
4.3.	Results	126
<b>5</b>	<b>Conclusions</b>	<b>131</b>
5.1.	Future developments	132
	<b>Bibliography</b>	<b>135</b>
	<b>List of Figures</b>	<b>141</b>
	<b>List of Tables</b>	<b>145</b>



## Introduction

Vehicle dynamics is the study of how vehicles respond to driver inputs, external forces, and environmental conditions. It plays a critical role in understanding and improving vehicle stability, handling, ride comfort, and safety. As described by *Milliken & Milliken (1995)* [1] and *Genta & Genta (2017)* [2], vehicle dynamics is a multidisciplinary field that involves tire mechanics, chassis dynamics, aerodynamics, and control systems, all of which contribute to the overall behaviour of a vehicle in different operating conditions.

As stated by the physicist Albert Einstein, “...the supreme goal of all theory is to make the irreducible basic elements as simple and as few as possible without having to surrender the adequate representation of a single datum of experience.” This philosophy is directly applicable to vehicle dynamics modeling, where the goal is to simplify the model as much as possible while retaining the essential behaviors that accurately reflect real-world performance. In vehicle dynamics, a simple yet effective model allows for easier computation, faster simulations, and applicability in real-time systems, making it crucial for both engineering design and practical applications in areas such as active safety systems, autonomous vehicles, and driver assistance technologies.

This brings us to a key perspective shared by statistician and engineer George E.P. Box, who famously said, “*All models are wrong, but some are useful.*” This statement underscores the inherent limitations of all models. Every model, no matter how sophisticated, approximates reality and thus contains inaccuracies. However, if the inaccuracies are small enough and do not significantly affect the key predictions of the system, models remain incredibly powerful tools. In the context of vehicle dynamics, even simplified models—despite their inherent inaccuracies—can provide valuable insights that guide vehicle design, performance testing, and safety analysis, while also offering considerable cost and time efficiencies in the development process.

The challenge, however, lies in the trade-off between simplicity and accuracy. While a simplified model reduces computational demands, there is always the risk that certain complexities of real-world vehicle behavior may be neglected. In these situations, a careful balance must be struck between a model's simplicity and its ability to produce effective results that closely match real-world observations.

The simple models also prove to be highly practical for real-time applications. Such models enable fast computations, making them ideal for real-time systems such as active suspension control, stability management, and autonomous vehicle navigation, where decisions need to be made in fractions of a second. However, simplifying the model too much—by omitting phenomena like roll motion, relaxation length, or cornering stiffness variation—can lead to inaccuracies in predicting the vehicle's true behavior, which can impact safety or performance.

Moreover, these simple vehicle models can be effectively implemented in MATLAB for simulation and testing. MATLAB offers a flexible environment for rapidly developing and refining vehicle dynamics models, and the results of such simulations can be directly compared with real vehicle tests. This comparison allows for the validation and refinement of the simplified model, ensuring that its predictions align closely with actual vehicle behavior.

Additionally, these simple models can be compared with more complex vehicle dynamics tools such as AdamsCar or other multibody simulation tools. These advanced tools provide detailed, high-fidelity simulations of vehicle behavior, accounting for complex interactions between components such as suspension, tire, and chassis. By comparing the results from simple models with those from more complex tools, engineers can evaluate the effectiveness and accuracy of the simplified model in predicting real-world behavior. This comparison also helps to identify the specific areas where simplifications may have compromised accuracy, allowing for further refinement or enhancement of the model. A structured approach to comparing simple and multibody models has been proposed by *Galvagno et al. (2021)* [3], who developed a methodology for parameter estimation of nonlinear single-track models using data from full-vehicle multibody simulations. Their research provides a framework for systematically extracting key parameters from multibody simulations and comparing them with simplified models. By leveraging the findings of *Galvagno et al. (2021)* [3], simple vehicle models can be refined and validated against multibody simulations and experimental data, making them more reliable tools for preliminary vehicle design and control strategy development.

A fundamental challenge in vehicle dynamics is that it deals with nonlinear system, meaning that small changes in initial conditions, inputs, or system parameters can lead to disproportionately large variations in behaviour. As emphasized in *S. H. Strogatz's (2015)* [4] work on nonlinear dynamics and chaos, many real-world systems, including vehicle dynamics, exhibit nonlinear characteristics that require appropriate modelling approaches. Although vehicle dynamics is fundamentally nonlinear, linearized models can still provide accurate predictions of system behavior under certain

conditions. By linearizing the equations of motion around a fixed operating point, it is possible to analyze local stability, handling characteristics, and control system design. Linearized models remain essential tools for control strategies and real-time applications, as they allow for simpler mathematical treatment while still capturing critical system dynamics.

However, when studying large-scale dynamic responses, limit handling, or transient behaviors, a nonlinear approach may be necessary to avoid losing key dynamic effects. In such cases, phase plane analysis, phase portraits, and bifurcation analysis provide deeper insights into vehicle stability and control limits.

Phase plane analysis is a powerful tool in nonlinear vehicle dynamics that allows for a graphical representation of system trajectories in state space. The study by *Zhang et al. (2011)* [5] explores the phase plane representation of vehicle handling and stability, illustrating how critical state transitions can be detected by analyzing system trajectories in terms of yaw rate and sideslip angle.

This approach is further expanded in *Wang et al. (2023)* [6], who investigate vehicle steering and braking stability regions. Their study shows how stability boundaries can be determined in phase space, providing a clear distinction between stable and unstable operating conditions. This analysis is crucial for understanding limit behavior in emergency maneuvers, where sudden changes in tire forces or road conditions can push the vehicle into an unstable regime.

Additionally, *Tian et al. (2023)* [7] examine the impacts of pavement rutting, road alignment, and adverse weather on vehicle lateral stability. Their research highlights how external disturbances, such as uneven road surfaces or sudden friction changes, influence the phase trajectories, potentially leading to loss of control. This reinforces the need for robust vehicle stability control systems that can adapt to varying operating conditions.

Beyond phase plane analysis, bifurcation theory is essential for understanding how vehicle stability changes as system parameters vary. A bifurcation occurs when a small change in a parameter (e.g., steering angle, speed, or road friction) causes a sudden qualitative change in vehicle behavior, such as transitioning from stable cornering to complete loss of control.

The study by *Della Rossa, Mastinu, and Piccardi (2012)* [8] performs a bifurcation analysis of an automobile negotiating a curve, identifying critical thresholds beyond which the vehicle becomes unstable. Their findings are particularly relevant for designing stability control systems, as they help

define safe operating regions and critical intervention points for active control strategies.

Moreover, *Mastinu et al. (2024)* [9] present an extensive investigation into how drivers lose control of their vehicles, emphasizing that the stability of an open-loop vehicle system is highly influenced by driver actions. This research demonstrates that even a vehicle that is inherently stable can become unstable due to improper driver inputs or delayed corrective actions.

These findings underline the fact that a realistic vehicle stability analysis must consider driver behavior. Consequently, closed-loop stability, where the driver (or an autonomous control system) interacts with the vehicle, must be analyzed alongside open-loop stability studies. This is especially important for autonomous vehicle control, where stability limits must be well-defined for automated decision-making.

Ultimately The key to effective vehicle dynamics modeling is to find the optimal trade-off between simplicity and accuracy. A simplified model that includes critical phenomena like roll motion, relaxation length, and cornering stiffness variation ensures computational efficiency while still providing reliable predictions of real-world vehicle behavior. Since vehicle dynamics is inherently nonlinear, relying solely on linear approximations may lead to inaccurate predictions, making nonlinear studies crucial for high-fidelity analysis.

Despite their inherent limitations, simplified models remain powerful tools for vehicle development, cost efficiency, and reduced time-to-market. By implementing these models in MATLAB, validating them with real vehicle tests, and comparing them with multibody simulation tools like AdamsCar, engineers can ensure that simplified models provide meaningful and actionable insights into vehicle dynamics, making them indispensable in modern automotive engineering.

## Structure of the thesis

In the first chapter, the models used for simulations and subsequently for the post-processing of data will be presented, utilizing a linearized and simplified model of the equations of motion. This chapter will also include a discussion on the linearization of the system around its equilibrium points to study its stability. This analysis will later allow us to define the variation of critical vehicle speeds as lateral acceleration conditions change. In addition, a new model for defining the characteristics of axles will be introduced in this chapter, as well as the basic theory used to define phase diagrams.

In the second chapter, the maneuvers and related results will be introduced to characterize the examined vehicle across its entire operating range, considering the influence of various parameters that may alter its characteristics. This chapter is particularly important since, ultimately, the vehicle's directional behavior is strongly dependent on the characteristics of the two axles and their variation under different operating conditions. The variations in axle characteristics will be used as known data for a model-based predictive system, which, through these modifications, will be able to determine the "real" capacity of both axles to generate lateral forces based on surrounding environmental data (such as road inclination, adhesion coefficients...) and the vehicle's operating conditions (including lateral acceleration...). Two methods for defining axle characteristics will be considered: the first relies on a full vehicle model implemented in Simulink and the use of well-known maneuvers in the literature, such as the ramp steer maneuver for vehicle characterization; the second is a model that requires only knowledge of tire and vehicle parameters (such as suspension parameters). The second approach allows for the estimation of axle characteristics without requiring a full vehicle simulation, thus offering greater computational efficiency compared to the first method. The results of both models will be analyzed in this document.

In the third chapter, the discussion will focus on the nonlinear analysis of the vehicle system, with particular attention to the effectiveness of representing stability regions in the phase plane. The development of this tool, aimed at studying nonlinear dynamics and the variation of equilibrium points under different operating conditions, will enable us to validate the critical speed diagram as a function of lateral acceleration, developed using the linearized vehicle model around its equilibrium points. This represents a significant additional contribution to the numerous studies already present in the literature on vehicle stability. Furthermore, the stability regions evaluated in an open-loop configuration will serve as a starting point for further analysis aimed at identifying the effects of the driver (or alternatively, a model-based predictive controller) on the stability region. In this case, we can discuss the closed-loop stability of the system. It will be highlighted how the driver's (or controller's) preparedness and reaction times play a crucial role in stability; these factors can significantly modify the stability region of the standalone vehicle system (i.e., in open loop), even potentially leading to instability in understeering vehicles, which are, by definition, stable. Once identified and parameterized, these stability regions can be used by the trajectory planner in autonomous driving environments to assess the feasibility of generated trajectories in terms of dynamic stability.

Chapter 4 will highlight the contribution of this work to the study of vehicle dynamics through example cases in simulation, with a particular focus on the effective benefits that the analyzed methods bring to the complete autonomous driving model.

## Methodology

The basic methodology was to analyze the vehicle system, first in open loop and in a second phase in closed loop, through simulations.

The first analysis to be examined is an analysis of the vehicle's characteristics as a series of parameters vary, such as road inclination, adhesion coefficients, and characteristic tire angles. Two approaches for defining the axle characteristics will be analysed: the first requires a full simulation of the vehicle model and thus the definition of a manoeuvre scenario widely used in the literature, namely the ramp steer manoeuvre, while the second will use tire and vehicle data to estimate the characteristics and therefore does not require a full simulation of the entire vehicle. A flowchart summarizes the main steps carried out.

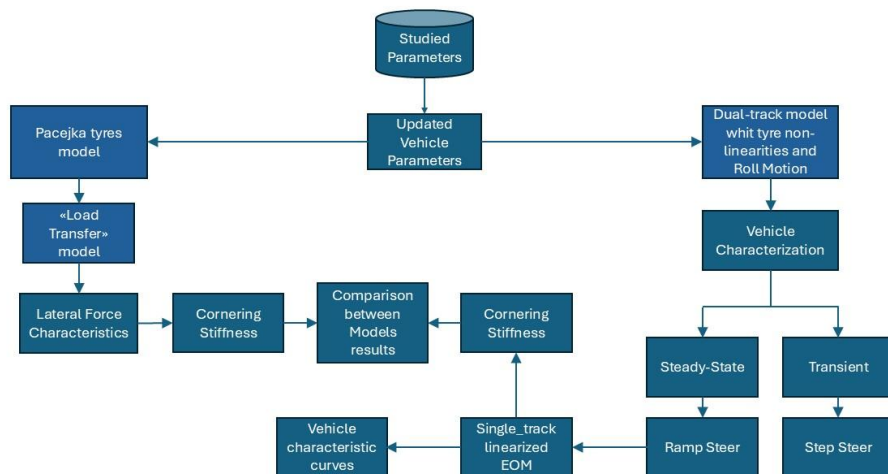


Figure 0.1:Flow chart cornering stiffness computation

Once the axle characteristics have been defined, a linearization model of these characteristics around the equilibrium points will be developed with the aim of defining the vehicle's characteristics as, for example, the lateral acceleration varies. This will make it possible to determine critical speeds and understeer

gradients not only around the system's origin but also for initial conditions different from this.

Below, the logic behind the study of the open-loop stability of equilibrium points, around which the system is linearized, is briefly presented.

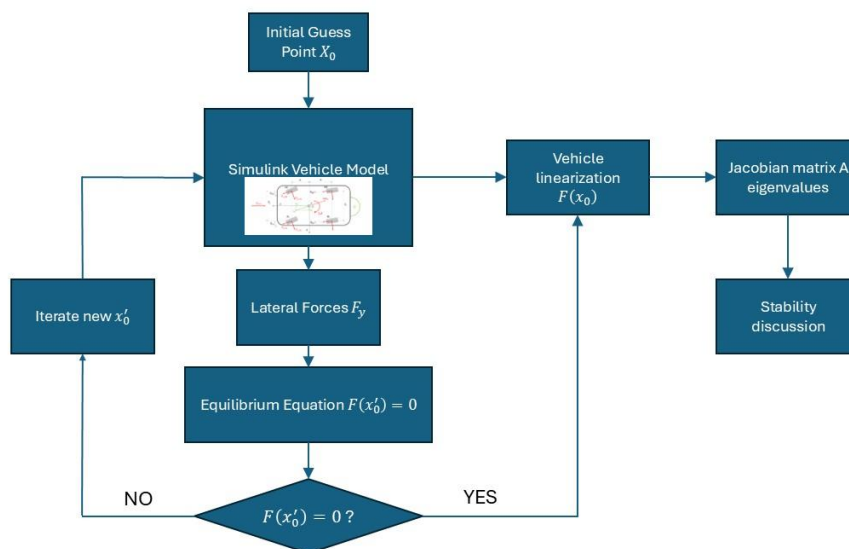


Figure 0.2: Flow chart equilibrium points open-loop stability analysis

## Document Outline

Briefly summarize the outline of the following thesis work.:

- Linearized models remain valuable tools for understanding local stability and developing real-time control strategies, especially when analyzing small perturbations around equilibrium points.
- Phase plane analysis helps visualize vehicle stability and instability regions, offering insights into how external disturbances or extreme maneuvers push the vehicle beyond safe limits.
- Bifurcation analysis reveals critical stability thresholds, identifying transition points between controllable and uncontrollable behavior.
- The open-loop stability of a vehicle is significantly affected by driver/controller behavior, making closed-loop analysis essential for realistic stability assessments, especially in autonomous vehicle development.

# 1 Vehicle Models and Tools

In this first chapter, an analysis of the models used to obtain the simulation results and thus to generate the relevant data will be carried out. First, the adopted vehicle models will be presented, and subsequently, the tool capable of analysing vehicle stability in the nonlinear domain will be introduced.

## 1.1. Vehicle Models

### 1.1.1. Single-track model

To study the behaviour of the vehicle in stationary conditions, a vehicle model called single-track model is used, of which the main equations are given below with reference to the following free body diagram.

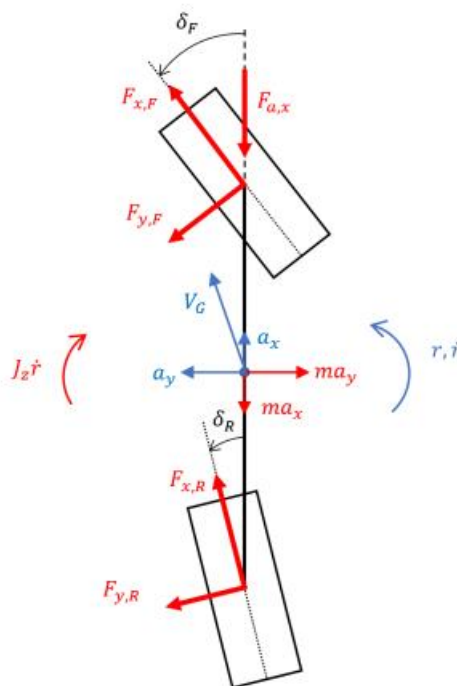


Figure 1.1: Free-body diagram of the single-track model

The dynamic equations are:

$$\sum_i^N X_i = ma_x ; \quad \sum_i^N Y_i = ma_y ; \quad \sum_i^N M_{zG,i} = J_z \dot{r}$$

Where  $X_i$  and  $Y_i$  are the force component along the longitudinal and lateral axis of the vehicle, in particular:

$$\begin{cases} F_{x_F} \cos \delta_F + F_{x_R} \cos \delta_r - F_{y_F} \sin \delta_f - F_{y_R} \sin \delta_r - F_{a_x} = m a_x \\ F_{y_F} \cos \delta_f + F_{y_R} \cos \delta_r + F_{x_F} \sin \delta_f + F_{x_R} \sin \delta_r = m a_y \\ F_{y_F} \cos \delta_f a - F_{y_R} \cos \delta_r b + F_{x_F} \sin \delta_f a - F_{x_R} \sin \delta_r b = J_z \dot{r} \end{cases}$$

Where  $F_{x_i}$  and  $F_{y_i}$  are the longitudinal and lateral force of the  $i$ -th axle with respect to the wheel reference frame and  $F_{x_a}$  is the aerodynamic drag force. Assuming small steering angle:

$$\sin \delta_f = 0 \quad ; \quad \cos \delta_f = 1$$

In our case we are considering a RWD and front steering vehicle so that:

$$\delta_r = 0 \quad ; \quad F_{x_r} \neq 0 \quad ; \quad F_{x_f} = 0$$

In this condition and considering  $V_G = \text{const}$  the second and third equations in () are decoupled from the first one so that we are decoupling the longitudinal motion of the vehicle with respect to the lateral one. The dynamic equations that describe the lateral motion became:

$$\begin{cases} F_{y_F} + F_{y_R} = m a_y \\ F_{y_F} a - F_{y_R} b = J_z \dot{r} \end{cases}$$

Such a system of equations is now linearized, except for the term expressing the lateral forces. To address this, the linear axle model is introduced:  $F_{y_i} = C_{\alpha_i} \cdot \alpha_i$

$$\begin{cases} C_{\alpha_f} \alpha_f + C_{\alpha_r} \alpha_r = m a_y \\ C_{\alpha_f} \alpha_f a - C_{\alpha_r} \alpha_r b = J_z \dot{r} \end{cases}$$

To eliminate the slip angle and to express the equation in terms of state variable  $\beta$  and  $\psi$ , we can introduce the congruence equation:

$$\alpha_f = \delta_f - \frac{v + r \cdot a}{u} \quad ; \quad \alpha_r = \delta_r - \frac{v - r \cdot b}{u}$$

$$\begin{cases} C_{\alpha_f} \left( \delta_f - \frac{v + r \cdot a}{u} \right) + C_{\alpha_r} \left( -\frac{v - r \cdot b}{u} \right) = m(\dot{v} + ur) \\ C_{\alpha_f} \left( \delta_f - \frac{v + r \cdot a}{u} \right) a - C_{\alpha_r} \left( -\frac{v - r \cdot b}{u} \right) b = J_z \dot{r} \end{cases}$$

Where  $u$  and  $v$  are the longitudinal and lateral component of  $V_G$ , in particular:

$$\vec{V}_G = ui + vj$$

Defining  $\beta$  as the angle between  $\mathbf{i}$  and  $\vec{V}_G$ , assuming small  $\beta$  angle

$$V_G = u = \text{const.}; \beta = \arctan\left(\frac{v}{u}\right) = \frac{v}{u}; \dot{\beta} = \frac{\dot{v}}{u}$$

The equation of motion ( ) can be rewritten in a state-space form:

$$\begin{cases} \frac{1}{mV} \left[ (-C_{\alpha_f} - C_{\alpha_r}) \beta + \left( \frac{C_{\alpha_r} \cdot b - C_{\alpha_f} \cdot a}{V} - mV \right) r + C_{\alpha_f} \cdot \delta \right] = \dot{\beta} \\ \frac{1}{J_z} \left[ (-C_{\alpha_f} \cdot a + C_{\alpha_r} \cdot b) \beta + \left( \frac{-C_{\alpha_f} \cdot a^2 - C_{\alpha_r} \cdot b^2}{V} \right) r + C_{\alpha_f} \cdot a \cdot \delta \right] = \dot{r} \end{cases}$$

We can define the simplified expression of the so-called *derivatives of stability* as:

$$Y_r = -\frac{aC_{\alpha_f} - bC_{\alpha_r}}{V}; Y_\beta = -(C_{\alpha_f} + C_{\alpha_r}); Y_\delta = C_{\alpha_f}$$

$$N_r = -\frac{a^2C_{\alpha_f} + b^2C_{\alpha_r}}{V}; N_\beta = -(aC_{\alpha_f} - bC_{\alpha_r}); N_\delta = aC_{\alpha_f};$$

In matrix form,

$$\begin{bmatrix} \dot{\beta} \\ \dot{r} \end{bmatrix} = \begin{bmatrix} \frac{Y_\beta}{mV} & \frac{Y_r}{mV} - 1 \\ \frac{N_\beta}{I_z} & \frac{N_r}{I_z} \end{bmatrix} \begin{bmatrix} \beta \\ r \end{bmatrix} + \begin{bmatrix} \frac{Y_\delta}{mV} \\ \frac{N_\delta}{I_z} \end{bmatrix} \delta_f$$

### 1.1.2. Single-track model: Linearization around its fixed points

With reference to [3], The objective of this part is to explain the mathematical model used to obtain the linearization of the system around its equilibrium points.

At the beginning of the stability study a simple model was used to express the contributions of lateral forces in linear field, but now it is our wish to deepen the analysis of system stability also in non-linear field, this is then done by studying the stability of the system around its equilibrium points.

We recall the EOM of the single-track model in the following form

$$\begin{cases} F_{y_f} + F_{y_r} = mu(\dot{\beta} + r) \\ F_{y_f} \cdot a - F_{y_r} \cdot b = J_z \cdot \dot{r} \end{cases} \quad (A.1)$$

We introduce the expressions useful to express the system in variational terms

$$\begin{cases} \beta = \bar{\beta} + d\beta \\ r = \bar{r} + dr \\ \delta = \bar{\delta} + d\delta \end{cases}$$

Replacing A.1 we get

$$\begin{cases} F_{y_f} + F_{y_r} = mu(d\dot{\beta} + \bar{r} + dr) \\ F_{y_f} \cdot a - F_{y_r} \cdot b = J_z \cdot dr \end{cases}$$

To derive the constant terms, that is the contributions of lateral forces to equilibrium, we set the variations of the states to zero, thus obtaining:

$$\begin{cases} F_{y_f} + F_{y_r} = mu\bar{r} \\ F_{y_f} \cdot a = F_{y_r} \cdot b \end{cases}$$

We then introduce the relation that allows us to linearize the contributions of lateral forces by a truncated Taylor polynomial at first order.

$$F_{y_i} = F_{y_i|\alpha=\bar{\alpha}} + \left( \frac{\partial F_{y_i}}{\partial \alpha_i} \right)_{|\alpha=\bar{\alpha}} \cdot (\alpha_i - \bar{\alpha}_i) \quad (\text{A.2})$$

Where

- subscript  $i$  refers to the axle considered: *front* o *rear*;
- terms  $\bar{\alpha}_i$  is the value at the equilibrium point of the drift angle for the  $i$ -th axle, therefore it is a constant value.
- term  $F_{y_i|\alpha=\bar{\alpha}}$ , and it is constant, it represents the value of lateral forces for the  $i$ -th axle at the equilibrium point  $\alpha_i$ . From now on writing will be simplified as  $\bar{F}_{y_i}$ .
- $C_{\bar{\alpha}_i} = \left( \frac{\partial F_{y_i}}{\partial \alpha_i} \right)_{|\alpha=\bar{\alpha}}$

Considering also the following expressions of drift angles:

$$\alpha_f = \delta_f - \frac{v+r \cdot a}{u} \quad ; \quad \alpha_r = -\frac{v-r \cdot b}{u} \quad (\text{A.3})$$

Replacing the expressions of lateral forces (A.2) and side slip angle(A.3) inside (A.1), we get

$$\left\{ \begin{array}{l} \left[ \bar{F}_{y_f} + C_{\bar{\alpha}_f} \cdot \delta_f - \frac{C_{\bar{\alpha}_f} \cdot v + C_{\bar{\alpha}_f} \cdot r \cdot a}{u} - C_{\bar{\alpha}_f} \cdot \bar{\alpha}_f \right] + \left[ \bar{F}_{y_r} - \frac{C_{\bar{\alpha}_r} \cdot v - C_{\bar{\alpha}_r} \cdot r \cdot b}{u} - C_{\bar{\alpha}_r} \cdot \bar{\alpha}_r \right] = mu(d\beta + r_o + dr) \\ \left[ \bar{F}_{y_f} + C_{\bar{\alpha}_f} \cdot \delta_f - \frac{C_{\bar{\alpha}_f} \cdot v + C_{\bar{\alpha}_f} \cdot r \cdot a}{u} - C_{\bar{\alpha}_f} \cdot \bar{\alpha}_f \right] \cdot a - \left[ \bar{F}_{y_r} - \frac{C_{\bar{\alpha}_r} \cdot v - C_{\bar{\alpha}_r} \cdot r \cdot b}{u} - C_{\bar{\alpha}_r} \cdot \bar{\alpha}_r \right] \cdot b = J_z \cdot \dot{dr} \end{array} \right. \quad (\text{A.4})$$

Considering also the following expressions:

$$\beta = \frac{v}{u} \quad ; \quad u = \text{const.} = V \quad ; \quad \dot{\beta} = \frac{\dot{v}}{V}$$

$$\left\{ \begin{array}{l} mVr_o + C_{\bar{\alpha}_f} \left( \bar{\delta}_f + d\delta_f - \bar{\beta} - d\beta - \frac{\bar{r} \cdot a}{V} - \frac{dr \cdot a}{V} - \bar{\alpha}_f \right) + C_{\bar{\alpha}_r} \left( -\bar{\beta} - d\beta + \frac{\bar{r} \cdot b}{V} + \frac{dr \cdot b}{V} - \bar{\alpha}_r \right) = mu(d\beta + r_o + dr) \\ C_{\bar{\alpha}_f} \left( \bar{\delta}_f + d\delta_f - \bar{\beta} - d\beta - \frac{\bar{r} \cdot a}{V} - \frac{dr \cdot a}{V} - \bar{\alpha}_f \right) \cdot a - C_{\bar{\alpha}_r} \left( -\bar{\beta} - d\beta + \frac{\bar{r} \cdot b}{V} + \frac{dr \cdot b}{V} - \bar{\alpha}_r \right) \cdot b = J_z \cdot \dot{dr} \end{array} \right.$$

Replacing the constant contributions of lateral forces as previously stated and also clarifying the terms  $\bar{\alpha}_f$  and  $\bar{\alpha}_r$  as

$$\bar{\alpha}_f = \bar{\delta}_f - \frac{\bar{v} + \bar{r} \cdot a}{V} \quad ; \quad \bar{\alpha}_r = -\frac{\bar{v} - \bar{r} \cdot b}{V}$$

Where terms  $\bar{\delta}_f$ ,  $\bar{v}$ ,  $\bar{r}$  represent the steady state (constant) values for a given lateral acceleration, and replacing within EOM it is possible to express the system in terms of variation with respect to equilibrium conditions, obtaining the following system

$$\left\{ \begin{array}{l} d\dot{\beta} = \frac{1}{mV} \left[ (-C_{\bar{\alpha}_f} - C_{\bar{\alpha}_r}) d\beta + \left( \frac{C_{\bar{\alpha}_r} \cdot b - C_{\bar{\alpha}_f} \cdot a}{V} - mV \right) dr + C_{\bar{\alpha}_f} \cdot d\delta \right] \\ d\dot{r} = \frac{1}{J_z} \left[ (-C_{\bar{\alpha}_f} \cdot a + C_{\bar{\alpha}_r} \cdot b) d\beta + \left( \frac{-C_{\bar{\alpha}_f} \cdot a^2 - C_{\bar{\alpha}_r} \cdot b^2}{V} \right) dr + C_{\bar{\alpha}_f} \cdot a \cdot d\delta \right] \end{array} \right. \quad (\text{A.6})$$

It is now possible to express the system in the state space.

$$\dot{\mathbf{x}} = \bar{A}\mathbf{x} + \bar{B}\mathbf{u}$$

$$\dot{\mathbf{x}} = \{d\beta, dr\}^T ; \mathbf{x} = \{d\beta, dr\}^T ; \mathbf{u} = \{d\delta_f\}^T$$

Matrices A and B correspond to linearized matrices in the equilibrium point introno. These matrices are now coefficients for ease of writing.

$$\bar{A} = \begin{bmatrix} a_{11} & a_{12} \\ a_{21} & a_{22} \end{bmatrix} \quad \bar{B} = \begin{bmatrix} b_{11} \\ b_{21} \end{bmatrix}$$

The following coefficients:

$$\begin{aligned} a_{11} &= \frac{1}{mV} (-C_{\bar{\alpha}_f} - C_{\bar{\alpha}_r}) \\ a_{12} &= \frac{1}{mV} \left( \frac{C_{\bar{\alpha}_r} \cdot b - C_{\bar{\alpha}_f} \cdot a}{V} - mV \right) \\ a_{21} &= \frac{1}{J_z} (-C_{\bar{\alpha}_f} \cdot a + C_{\bar{\alpha}_r} \cdot b) \\ a_{22} &= \frac{1}{J_z} \left( \frac{-C_{\bar{\alpha}_f} \cdot a^2 - C_{\bar{\alpha}_r} \cdot b^2}{V} \right) \\ b_{11} &= \frac{1}{mV} C_{\bar{\alpha}_f} \\ b_{21} &= \frac{1}{J_z} C_{\bar{\alpha}_f} \cdot a \end{aligned}$$

We obtain the same matrices as in the case of the linear field study. The stability study is reduced to the study of the eigenvalues of the updated A matrix with drift stiffnesses, this time evaluated by simulations at different lateral acceleration values, such as:

$$C_{\bar{\alpha}_i} = - \left( \frac{\partial F_{y_i}}{\partial \alpha_i} \right)_{|\alpha=\bar{\alpha}}$$

### 1.1.3. Double-track model

Finally, the complete model used in the simulations is presented below. This model, known in the literature as the double-track model, is augmented with the contributions of roll motion, which adds an additional degree of freedom to the system and increases the model's accuracy compared to the real vehicle system. A general overview of the blocks implemented in Simulink is provided below.

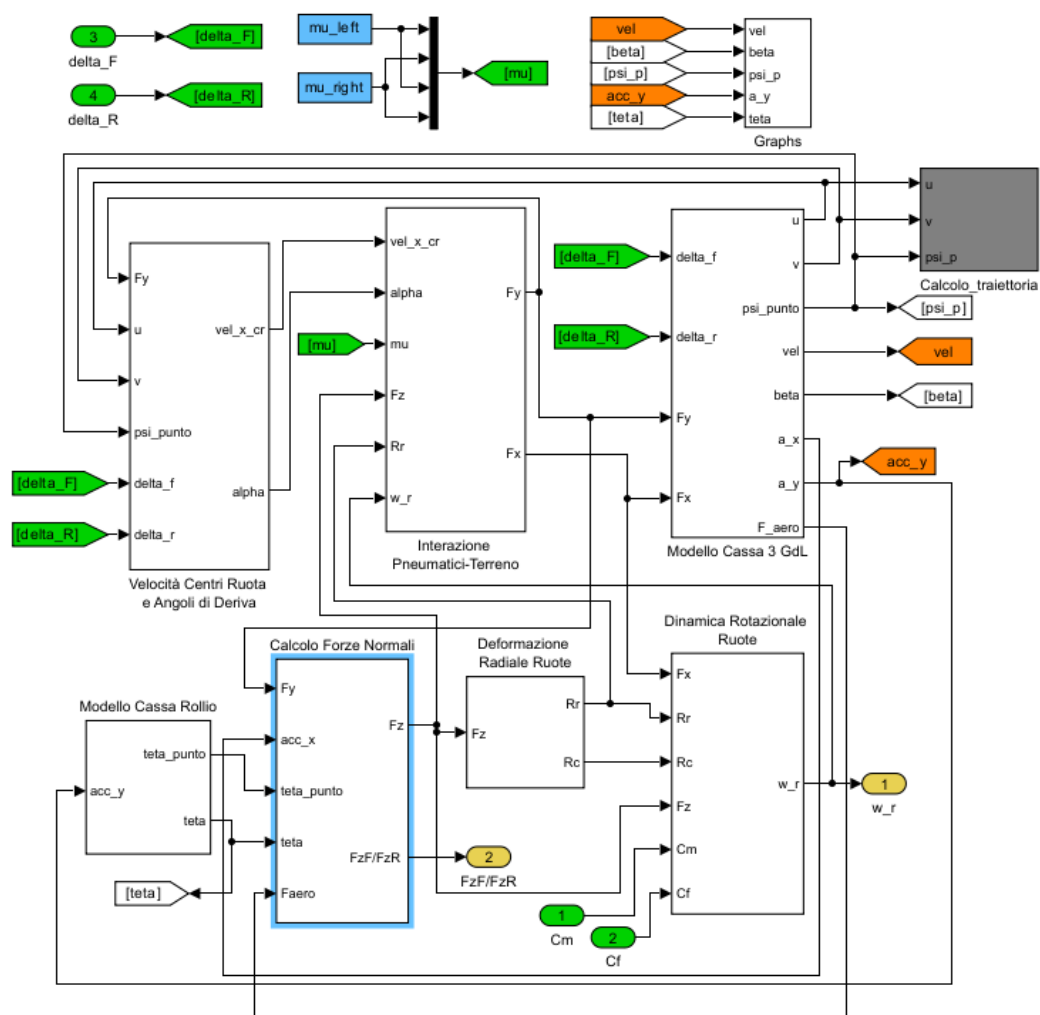
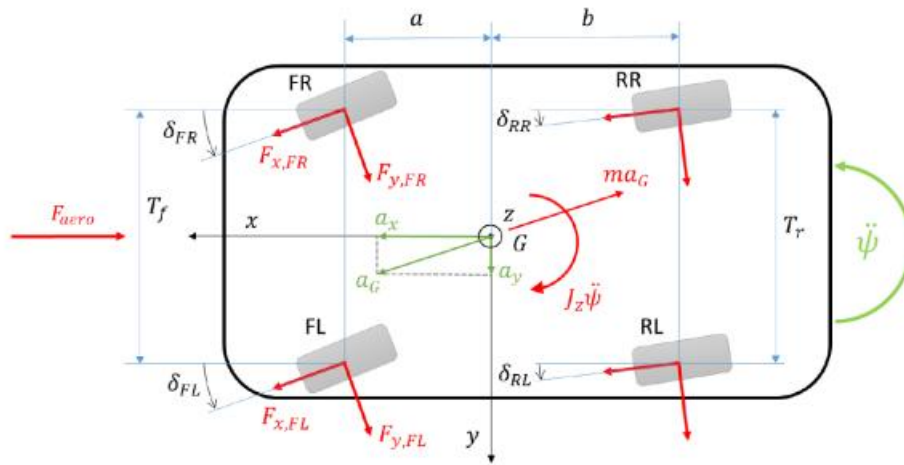


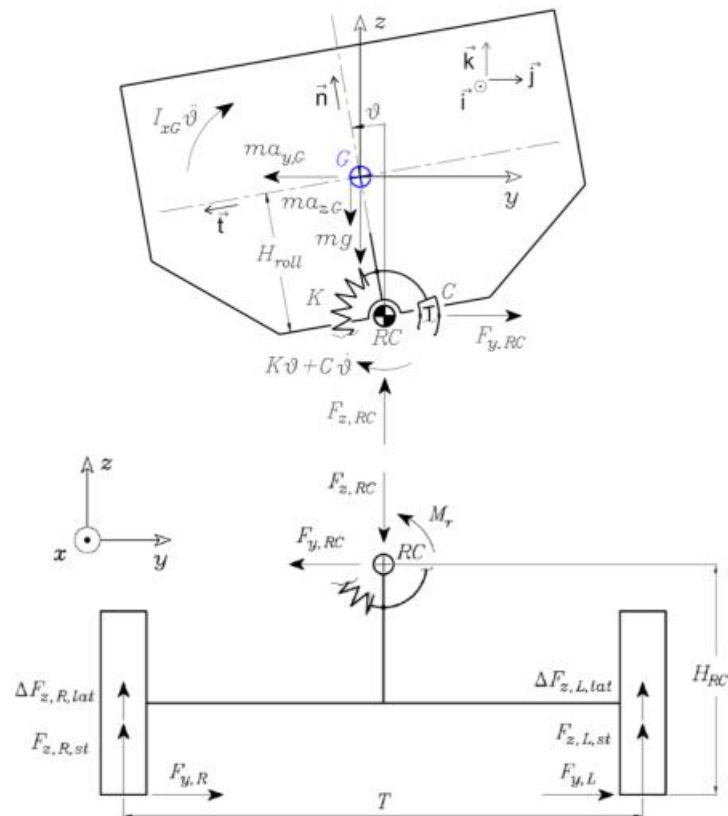
Figure 1.2 : Simulation Model Block Diagram

The free-body diagrams of the system and the main governing equations are provided below



$$\left\{ \begin{array}{l} a_x = \frac{1}{m} \left[ (F_{x,FL} + F_{x,FR}) \cos \delta_F + (F_{x,RL} + F_{x,RR}) \cos \delta_R - (F_{y,FL} + F_{y,FR}) \sin \delta_F - (F_{y,RL} + F_{y,RR}) \sin \delta_R - \frac{1}{2} A_f \rho C_x u^2 \right] \\ a_y = \frac{1}{m} \left[ (F_{x,FL} + F_{x,FR}) \sin \delta_F + (F_{x,RL} + F_{x,RR}) \sin \delta_R - (F_{y,FL} + F_{y,FR}) \cos \delta_F - (F_{y,RL} + F_{y,RR}) \cos \delta_R \right] \\ \ddot{\psi} = \frac{1}{J_z} \left[ (F_{x,FL} - F_{x,FR}) \frac{t_f}{2} \cdot \cos \delta_F + (F_{x,RL} - F_{x,RR}) \frac{t_r}{2} \cdot \cos \delta_R + (F_{x,FL} + F_{x,FR}) a \cdot \sin \delta_F + (F_{x,RL} + F_{x,RR}) a \cdot \sin \delta_R + \right. \\ \left. + (F_{y,FL} + F_{y,FR}) a \cdot \cos \delta_F - (F_{y,RL} + F_{y,RR}) b \cdot \cos \delta_R - (F_{y,FL} - F_{y,FR}) \frac{t_f}{2} \cdot \sin \delta_F + (F_{x,RL} - F_{x,RR}) \frac{t_r}{2} \cdot \sin \delta_R \right] \end{array} \right.$$

One of the critical phenomena that must be accounted for in even the simplest vehicle models is roll motion, which describes the lateral tilting of the vehicle body during cornering. Roll motion has a significant impact on stability, handling, and comfort. If ignored, the model might fail to reflect important aspects of vehicle behavior such as weight transfer, tire grip, and vehicle stability during high-speed cornering. Including roll motion in a simple model ensures that these behaviors are captured without overwhelming the system with unnecessary complexity.



$$\ddot{\theta} = \frac{1}{(I_{x_g} + mh_{rc}^2)} [ma_y h_{rc} \cos\theta + mgh_{rc} \sin\theta - K_{roll}\theta - C_{roll}\dot{\theta}]$$

Similarly, the relaxation length -the delay between the application of longitudinal/lateral forces (such as braking or acceleration) and the resulting tire response- must also be considered. The relaxation length reflects the time it takes for the tire to respond fully to changes in longitudinal/lateral forces due to factors such as tire deformation and road surface friction. In real-world driving, this delay can significantly affect vehicle handling, particularly during transient maneuvers such as braking or acceleration in corners. Neglecting the relaxation length in a simplified model could lead to inaccuracies in predicting the vehicle's response to such inputs. Including this phenomenon, even in a simplified form, allows the model to more accurately reflect the vehicle's dynamic response and improves the relevance of the model for real-time applications such as stability control and anti-lock braking systems.

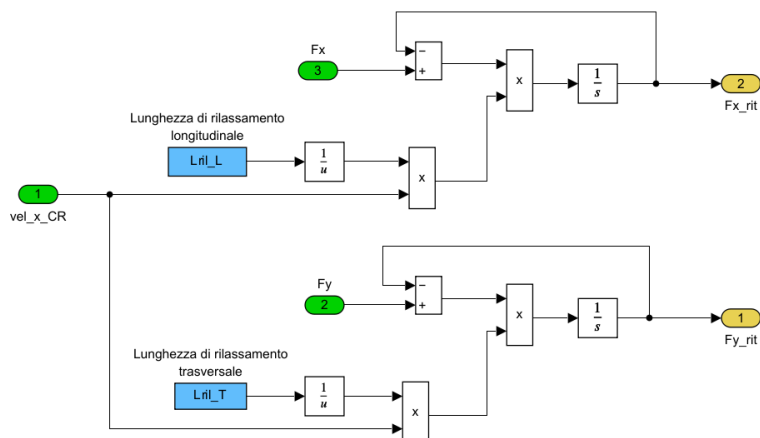


Figure 1.3 : Relaxation Length block Diagram

Furthermore, the tire model used will be presented in more detail in **Errore. L'origine riferimento non è stata trovata.** This model is employed to account for the nonlinearity of the tire characteristics, a choice that is crucial for an accurate comparison between the simulation model and the actual vehicle behaviour.

### 1.1.4. Vehicle model and Controller

The goal of this thesis work is to leverage the developed axle characteristics and closed-loop stability maps to enhance the performance of the controller in autonomous driving scenarios. Below, the complete vehicle model equipped with a path generator and a model-based predictive controller will be briefly introduced. For further details, please refer to the reference [10].

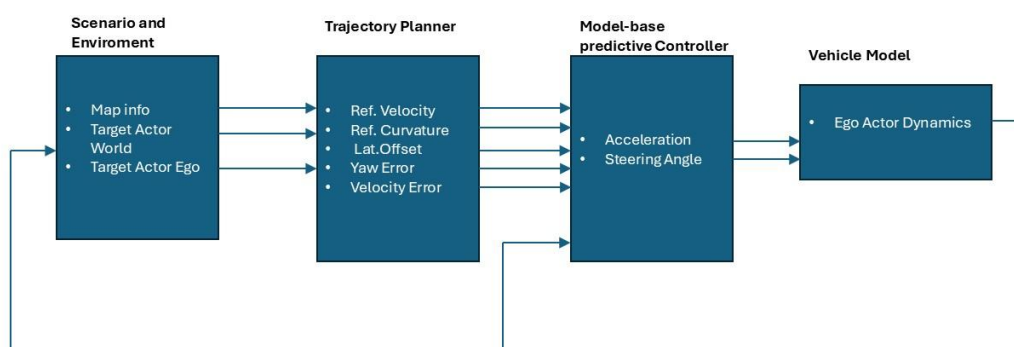


Figure 1.4 : Flow Chart Controller Model

For the analysis of the trajectory planner and controller blocks, reference is made to the "Highway Lane Change Planner" model available within Matlab's "Automated Driving Toolbox." For a more detailed analysis of these blocks, please refer to the documentation available in Matlab. However, it is important to specify the two most significant modifications introduced within these blocks.

#### Trajectory Planner upgrade

The trajectory planning block is responsible for generating and evaluating a set of feasible trajectories for the vehicle. However, in the baseline model available in Matlab's toolbox, feasibility analyses did not include any verification of the system's dynamic stability.

To address this, this thesis introduces this functionality by leveraging stability maps of the controlled vehicle in the phase plane. This verification aims to assess, based on the velocity and curvature parameters of the trajectory under consideration, the possible future state conditions of the system using updated axle characteristic maps according to the vehicle's operating conditions.

The significance of this update will be analyzed in greater detail in Chapter 4, which focuses on simulation test

## Adaptive MPC Controller

A general adaptive MPC flow chart is presented below. This type of controller is a flexible approach to nonlinear system control. The general concept is that for each time-step a *prediction* over a well-defined *time horizon* is computed using a model of the plant, starting from the actual measured output and control moves. The command input selected is then chosen as the one that leads the plant to the closest desired behavior by means of some on-line optimization algorithm.

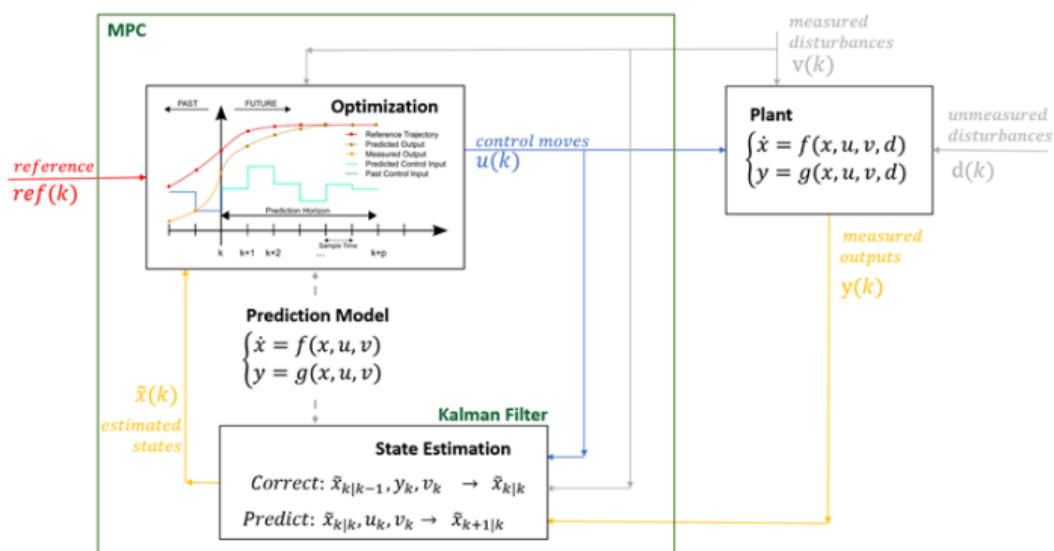


Figure 1.5 :Adaptive MPC flow chart

In our specific case, the model underlying the state estimator is a combination of a single-track model, like the one analyzed in 1.1.1, and an adaptive cruise control model

Whit reference to Matlab documentation [[Path Following Control System](#)], the combined model is described below.

### Adaptive Cruise Control Predictive Model

The predictive state-space model for adaptive cruise control in matrix form is:

$$x(t) = \begin{bmatrix} a_{x_{out}} \\ v_{x_{out}} \end{bmatrix}; y(t) = v_{x_{out}}; u(t) = a_{x_{in}}$$

$$A_1 = \begin{bmatrix} 1 & 0 \\ -\frac{1}{\tau} & 0 \end{bmatrix}; B_1 = \begin{bmatrix} 1 \\ \tau \end{bmatrix}; C_1 = [0 \ 1]; D_1 = 0$$

Here,  $\tau$  is the Longitudinal acceleration tracking time constant parameter.

The input to this model is the longitudinal acceleration, and the output is the longitudinal velocity.

### Lane-Keeping Predictive Model

The predictive state-space model for lane keeping in matrix form is:

$$x(t) = \begin{bmatrix} v_y \\ \dot{\psi} \end{bmatrix}; y(t) = \begin{bmatrix} v_y \\ \dot{\psi} \end{bmatrix}; u(t) = \delta_f$$

$$A_2 = \begin{bmatrix} -\frac{(C_f + C_r)}{mv_x} & -\frac{(C_f a - C_r b)}{mv_x} - v_x \\ -\frac{(C_f a - C_r b)}{J_z v_x} & -\frac{(C_f a^2 + C_r b^2)}{J_z v_x} \end{bmatrix}; B_2 = \begin{bmatrix} \frac{1}{m} \\ \frac{a}{J_z} \end{bmatrix};$$

$$C_2 = \begin{bmatrix} 1 & 0 \\ 0 & 1 \end{bmatrix}; D_2 = [0 \ 0]^T$$

Here:

- $v_y$  is the lateral velocity.
- $\dot{\psi}$  is the yaw rate.
- $\delta_f$  Steering wheel angle at the front tires.
- 

In this model, the update of the cornering stiffness values  $C_f$  and  $C_r$  has been implemented to account for variations in the vehicle's operating conditions and the characteristics of the scenario (such as road inclination and adhesion coefficients).

### Combined Path-Following Predictive Model

The Path Following Control System block combines these models as follows:

$$x(t) = \begin{bmatrix} a_{xout} \\ v_{xout} \\ v_y \\ \dot{\psi} \end{bmatrix}; u(t) = \begin{bmatrix} a_{xout} \\ \delta_f \end{bmatrix}$$

$$A = \begin{bmatrix} A_1 & 0 \\ 0 & A_2 \end{bmatrix}; B = \begin{bmatrix} B_1 & 0 \\ 0 & B_2 \end{bmatrix};$$

$$C = \begin{bmatrix} C_1 & 0 \\ 0 & C_2 \end{bmatrix}; D = \begin{bmatrix} D_1 & 0 \\ 0 & D_2 \end{bmatrix}$$

## 1.2. Tools

### 1.2.1. Map-based Axial Cornering Stiffness tool

This section will consider a different method for axle characterization. This model involves using only the block related to the tire-ground interaction, within which the semi-empirical Pacejka '96 model is implemented.

Please note that the tire contact model used is the same adopted in previously described model.

$$F_y = D \cdot \text{sen}(C \cdot \text{atan}(B\alpha - E(B\alpha - \text{atan}B\alpha)))$$

Where B,C,D,E, are empirical coefficients. An example of nonlinear characteristics is reported in the following figure.

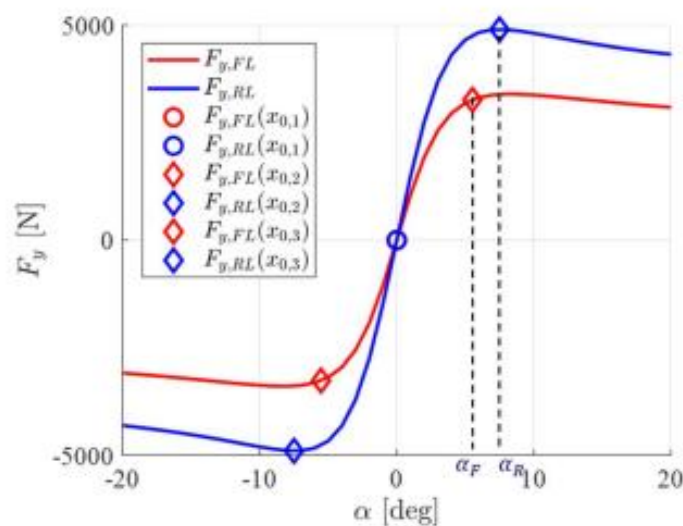


Figure 1.6: Example of non-linear tire characteristics

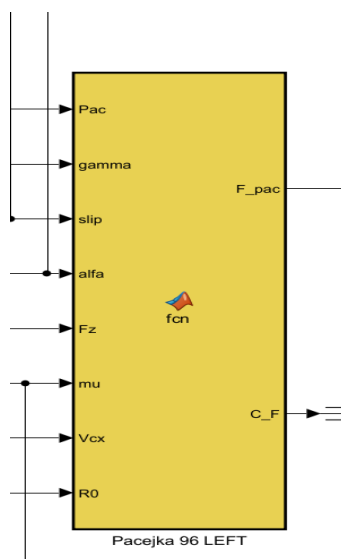


Figure 1.7 : Pacejka 96 model

The model requires the following inputs:

**Pac:** These represent the various coefficients present in the semi-empirical formula.

**Gamma:** Represents the camber angle, which is considered zero in the simulations performed in this section.

**Slip:** The longitudinal slip of the individual tire. By varying this parameter, it is possible to estimate its influence on the axle characteristics.

**Alpha:** Slip angles.

**Fz:** Normal forces on the tire. As with slip, assigning different Fz values allows for simulating various conditions of lateral load transfer (and thus lateral accelerations).

**Mu:** Tire-ground friction coefficient.

**Vcx:** Velocity of the wheel center.

**R0:** Radius of the undeformed tire.

In the following discussion, the steps used within the algorithm for computing the cornering stiffness will be explained. By varying the previously described parameters, it will also be possible to estimate the influence these parameters have on the magnitude of forces the tire can exchange with the ground, which define the dynamic behavior of a vehicle.

The validation tool will therefore be the characteristics previously determined for the vehicle under analysis through the ramp steer maneuvers in 2.3.2.

## Method

The following outlines the method used to obtain the characteristics of a single axle point by point, starting from the characteristics of the individual wheels on the same axle. This method assumes the validity of the following hypothesis: the wheels on the same axle are subjected to the same slip angle.

Now, let us introduce some parameters that will be useful later:

$q_r$ : Height from the ground to the roll center at the rear axle.

$q_f$ : Height from the ground to the roll center at the front axle.

$q$ : Height from the ground to the roll center at the vehicle's center of gravity.

$K_{Rf}$ : Overall roll stiffness of the front axle.

$K_{Rv}$ : Overall roll stiffness of the vehicle.

$G_r$ : Roll gradient, defined as the ratio between the roll angle and lateral acceleration, which can be expressed as:

$$G_r = \frac{m \cdot (h - q)}{K_{Rv} - mg \cdot (h - q)}$$

Through the force and moment equilibrium expressions for the individual axles, the following expressions can be derived:

$$\Delta F_{zF} = \frac{m \cdot a_y}{t_f} \cdot \left( \frac{b}{L} \cdot q_f + \frac{G_r}{m} \cdot K_{Rf} \right) = \eta_f \cdot m \cdot a_y$$

$$\Delta F_{zR} = \frac{m \cdot a_y}{t_r} \cdot \left( \frac{a}{L} \cdot q_r + \frac{G_r}{m} \cdot K_{Rr} \right) = \eta_r \cdot m \cdot a_y$$

By decomposing the lateral force contribution for the front and rear axles, the following expression can be defined, which will then be useful for characterizing the axle as the load transfer varies.

$$\Delta F_{zF} = \eta_f \cdot \frac{L}{b} \cdot F_{yF}$$

$$\Delta F_{zR} = \eta_r \cdot \frac{L}{a} \cdot F_{yR}$$

The following steps are now outlined for the axle characterization:

**Step 1:** Test the individual tire (both inner and outer during a turn) under the effect of symmetric and opposite load transfer.

**Step 2:** Sum the lateral forces of the inner and outer tires for each vertical load condition examined.

**Step 3:** Evaluate the lateral forces developed under the given vertical load condition using the coefficients  $\eta_f$  and  $\eta_r$ .

**Step 4:** Compare the lateral force value obtained in Step 3 and select the corresponding value according to the curves plotted in Step 2.

The curve obtained by interpolating the data derived in Step 4 will correspond to the actual operating condition of the axle under the specific lateral load transfer conditions (or alternatively, the lateral acceleration).

## 1.2.2. Phase Portrait and Bifurcation Analysis

### 1.2.2.1. Phase Plane theoretical background

There are mainly three causes of non-linearity of the vehicle system: the trigonometric functions which cannot be approximated to linear (small angles) in all operating conditions, the product of variables, and finally the most relevant one: the non-linear characteristics of the axles (in this model the tyres characteristic is computed by the Pacejka empirical formula). Since picture are more helpful than formula for analysing nonlinear system, we now introduce a method to describe and interpret the nonlinear equation, and thus the stability of the vehicle, through the use of vector fields. A generic system can be seen as a vector field in the form

$$\dot{\mathbf{x}} = f(\mathbf{x})$$

Where  $\mathbf{x}$  is the states vector and  $f(\mathbf{x})$  is the non-linear function that describes the state evolution. In the analysed case, the following states of the system are defined as the side slip angle and the yaw rate.

$$\mathbf{x} = [\beta, \psi]^T$$

To describe the *trajectory* of this state we can start from a generic initial condition, known as *phase point*,  $\mathbf{x}_o = [\beta_o, \psi_o]^T$  and follow its variation according to  $f(\mathbf{x})$ . Unfortunately, the analytical solution of a nonlinear system is really hard to find analytically, and a quantitative solution is needed, so we can proceed by numerical integration of the equation. The most important property of a nonlinear continuous and differentiable system is that the existence and uniqueness theorem:

“Considering the initial value problem  $\dot{\mathbf{x}} = f(\mathbf{x}), \mathbf{x}(0) = \mathbf{x}_o$ , suppose that  $f$  is continuously differentiable system then for  $\mathbf{x}_o$  the initial value problem has a unique solution  $\mathbf{x}(t)$ . “

Furthermore, this theorem led to state that all the different trajectories never intersect each other. A graph that shows the different trajectory of the system starting from any possible initial condition is defined as *phase portrait*. The shape of this type of graph are governed by same particularly interesting point known as *equilibrium solution* or *fixed point* such that  $\dot{\mathbf{x}} = [0 \ 0]^T$ . It is also possible to define two main categories of equilibrium point:

- **Stable:** if any sufficiently small disturbances away from that point leads to a trajectory that ends in the same equilibrium point. We say that this type of point shows an *attractive* nature.
- **Unstable:** if any sufficiently small disturbances from that point grow up in time. We say that this type of point shows a *repulsive* nature.

However, the concept of “small disturbances” is complex to be define and we can generalize the above definition by saying that a stable equilibrium point is locally stable and not globally stable.

An extremely important tool to study the nature of equilibrium point is the linearization around a fixed point, in fact the nature of the equilibrium point studied throughout linearization coincide whit the real nature of the equilibrium points of the nonlinear system. So, the main concept is that we can approximate the phase portrait near a fixed point by that of a corresponding linear system. The linearization of a system can be expressed by formulating the Taylor series expansion. In particular, whit respect to a generic two-dimensional system like one needed to describe the lateral behaviour of the vehicle:

$$\dot{x}_1 = f(x_1, x_2)$$

$$\dot{x}_2 = g(x_1, x_2)$$

it is possible to write:

$$f(x_1, x_2) = f(x_{0,1}, x_{0,2}) + \frac{\partial f}{\partial x_1}(x_{0,1}, x_{0,2}) \cdot (x_1 - x_{0,1}) + \frac{\partial f}{\partial x_2}(x_{0,1}, x_{0,2}) \cdot (x_2 - x_{0,2}) + O(x_1^2, x_2^2, x_1 x_2)$$

$$g(x_1, x_2) = g(x_{0,1}, x_{0,2}) + \frac{\partial g}{\partial x_1}(x_{0,1}, x_{0,2}) \cdot (x_1 - x_{0,1}) + \frac{\partial g}{\partial x_2}(x_{0,1}, x_{0,2}) \cdot (x_2 - x_{0,2}) + O(x_1^2, x_2^2, x_1 x_2)$$

Where partial derivatives are to be evaluated at the fixed point  $(x_{0,1}, x_{0,2})$ , and by the definition of fixed point we can say that  $f(x_{0,1}, x_{0,2}) = 0$  and  $g(x_{0,1}, x_{0,2}) = 0$

In a matrix form

$$\begin{pmatrix} \dot{x}_1 \\ \dot{x}_2 \end{pmatrix} = \begin{bmatrix} \frac{\partial f}{\partial x_1} & \frac{\partial f}{\partial x_2} \\ \frac{\partial g}{\partial x_1} & \frac{\partial g}{\partial x_2} \end{bmatrix}_{(x_{0,1}, x_{0,2})} \begin{pmatrix} x_1 \\ x_2 \end{pmatrix} + \text{quadratic terms}$$

Where  $A = \begin{bmatrix} \frac{\partial f}{\partial x_1} & \frac{\partial f}{\partial x_2} \\ \frac{\partial g}{\partial x_1} & \frac{\partial g}{\partial x_2} \end{bmatrix}_{(x_{0,1}, x_{0,2})}$  is the *Jacobian* matrix of the system at the fixed

point  $(x_{0,1}, x_{0,2})$ . If the Quadratic terms are negligible, we obtain the linearized system:

$$\begin{pmatrix} \dot{x}_1 \\ \dot{x}_2 \end{pmatrix} = \begin{bmatrix} \frac{\partial f}{\partial x_1} & \frac{\partial f}{\partial x_2} \\ \frac{\partial g}{\partial x_1} & \frac{\partial g}{\partial x_2} \end{bmatrix}_{(x_{0,1}, x_{0,2})} \begin{pmatrix} x_1 \\ x_2 \end{pmatrix}$$

It is now possible to discuss the classification of the fixed point of the linearized system, based on matrix  $A$ , as a function of the sign of the trace, determinant, and discriminant of  $A$ .

If  $A = \begin{bmatrix} a & b \\ c & d \end{bmatrix}$  by definition:

$$\text{Trace}(A): \tau = a+d;$$

$$\text{Det}(A): \Delta = ad - bc$$

$$\text{Discriminant of general solution: } \Delta_d = \tau^2 - 4\Delta$$

It is now possible to show all the different types of fixed point on a single graph.

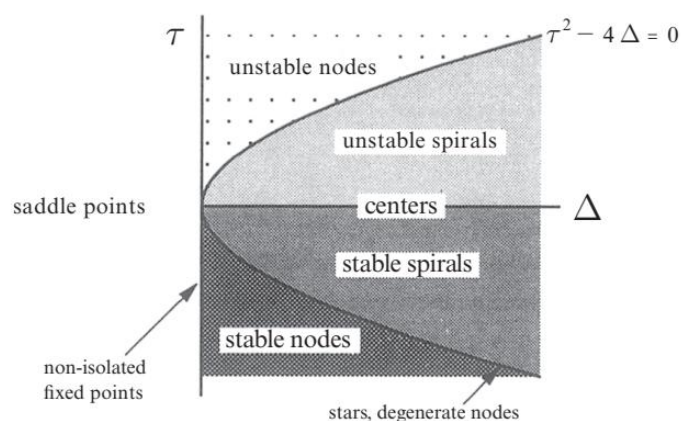


Figure 1.8: Fixed Point Classification

With reference to Figure 1.8: Fixed Point Classification, it is possible to see that the majority of fixed points belong to the category of *saddle points*, *nodes* and *spirals*. The other type of classification are *borderline cases* that occur typically in frictionless system, and they are not evaluated in this work. For further insights on the topic, refer to [4].

#### 1.2.2.2. Bifurcation

What has been discussed so far is useful for determining the stability region of the vehicle system in the nonlinear domain through the linearization of the system around its equilibrium points. However, this stability region is actually valid only under specific operating conditions of the vehicle. Looking at Figure 3.2 and Figure 3.3 it is possible to see that a variation in steering angle changes the shape of the phase portrait and can also lead to equilibrium point destruction. The method by which it is possible to parameterize the behaviour of equilibrium points as certain operating conditions and parameters change is called *bifurcation analysis*. Bifurcation is the fundamental mechanism by which equilibrium points are created or destroyed, or change their nature (stable, unstable) as the parameters of the nonlinear system vary. In Chapter 2, several parameters will be analysed that can alter the vehicle's behaviour, even making an understeering vehicle behave as if it were oversteering. This is a critical aspect when attempting to parameterize the stability conditions of the vehicle to avoid instability phenomena.

## 2 Vehicle Characterization

The aim of this chapter is to characterize the vehicle model used to obtain a clear understanding of its behaviour. The vehicle whose data is listed in Table 2.1: Vehicle Data has been subjected to specific maneuvers as described in 2.2 for this purpose.

### 2.1. Vehicle Data

The data of the analyzed vehicle is given below. It is useful to pay attention to the values of static load distribution, percentage of distribution of anti-roll bar stiffness for front axle and type of traction (RWD), because these parameters have been specially chosen to study the characterization of a vehicle tending to oversteer behaviour, and therefore unstable above a certain critical speed threshold.

Table 2.1: Vehicle Data

	value	unit
<b>m</b>	1600	[kg]
<b>L</b>	2.6	[m]
<b>Jz</b>	2860	[kg · m <sup>2</sup> ]
<b>a</b>	1.56	[m]
<b>b</b>	1.04	[m]
<b>Hg</b>	0.65	[m]
<b>K</b>	$1.3 \cdot 10^5$	[Nm/rad]
<b>%ARB front</b>	30 %	
<b>Rs</b>	13	
<b>TBR</b>	1	
<b>Ro</b>	$3.28 \cdot 10^{-1}$	[m]
<b>Toe Front</b>	-0.1	[deg]
<b>Toe Rear</b>	0.1	[deg]
<b><math>H_{rcfront}</math></b>	40	[mm]
<b><math>H_{rcrear}</math></b>	100	[mm]
<b>Traction</b>	RWD	[-]

## 2.2. Type of manoeuvres

The types of manoeuvres that have been examined are well-known in literature and are referred to as:

- *Ramp steer*
- *Step steer*

The first of these is particularly suitable for tracing the understeering and side slip characteristics of the vehicle with good approximation in linear field, while the second one is used to analyse the transient behaviour of the vehicle.

## 2.3. Ramp Steer

Table 2.2: Ramp Steer parameters.

	value	unit
<b>Steering angle slope</b>	5	[deg/s]
<b>Vehicle speed</b>	50	[Km/h]

The maneuver consists of maintaining the vehicle's speed and gradually increasing, with a constant rate, the steering: the increase in steering angle does not occur too quickly in order to maintain the study of vehicle dynamics as a progressive succession of equilibrium states.

The parameters for speed, lateral acceleration and applied steering angle are given below

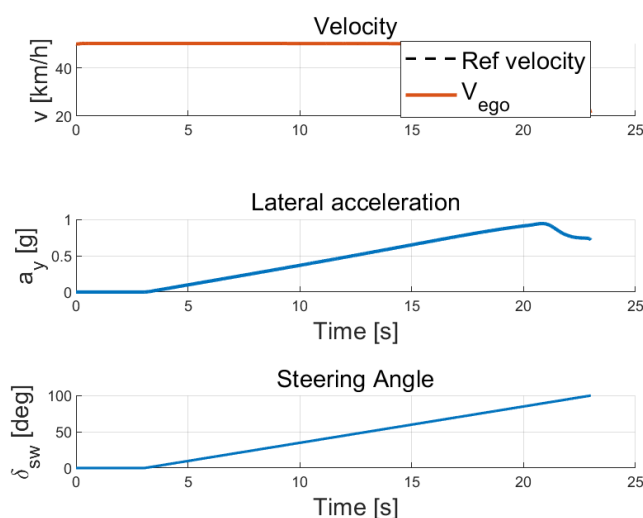


Figure 2.1: Input Ramp Steer

### 2.3.1. Vehicle's responses

The vehicle's responses are provided here in terms of side slip angle and yaw rate as function of time. The choice of this type of maneuver is driven by the objective of characterizing the behaviour of the axles as the lateral acceleration varies, up to its maximum limit.

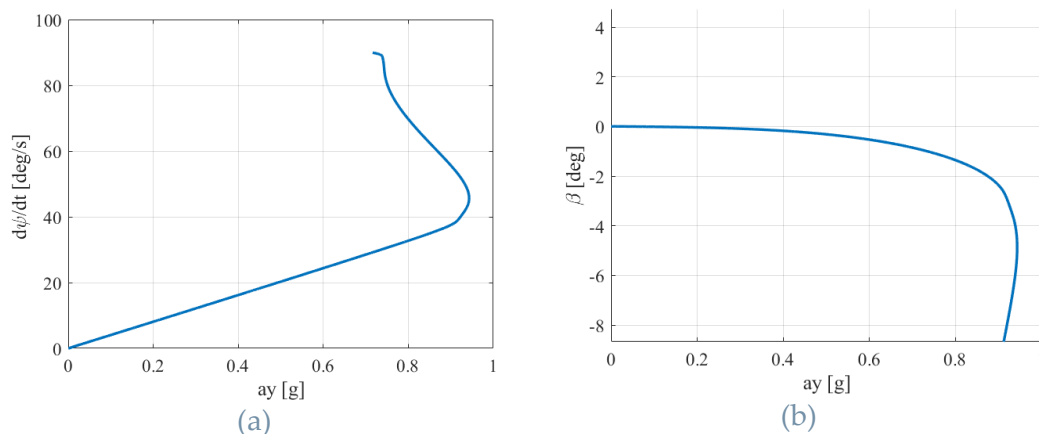


Figure 2.2: (a) Yaw rate (b) Side slip as function of  $a_y$ .

From the simulation data, it is also possible to evaluate the kinematic sideslip angle  $\beta_0$  as:

$$\beta_0 = \frac{b}{R} = b \cdot \frac{\dot{\psi}}{V}$$

From this value and the computed value of the sideslip angle  $\beta$ , it is already possible to visualize  $\beta$  and  $\beta_0$  as a function of lateral acceleration.

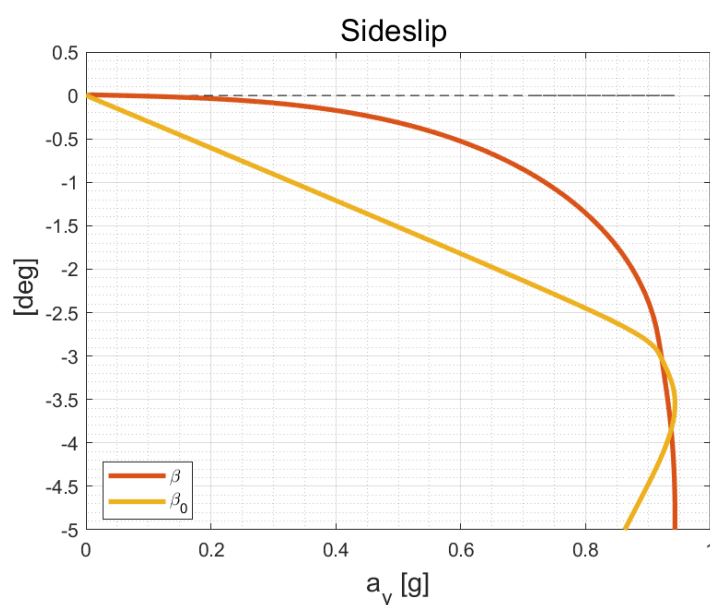


Figure 2.3: Side Slip vs Kinematic Side Slip

### 2.3.2. Lateral Force and Cornering Stiffness

The values of lateral forces and slip angles in output to the vehicle model are shown below. These values were then used to estimate the cornering stiffness of each axis.

Figure 2.4: (a) Lateral Forces (b) Slip Angle as function of time

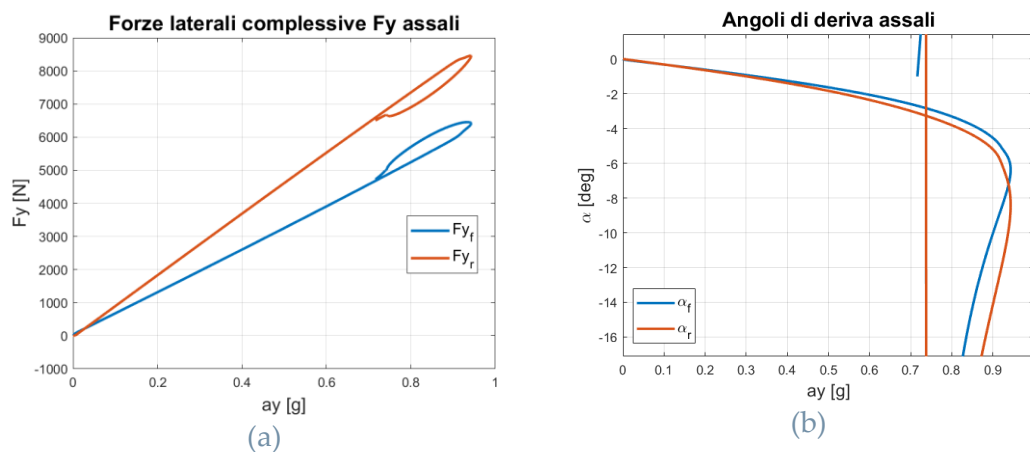
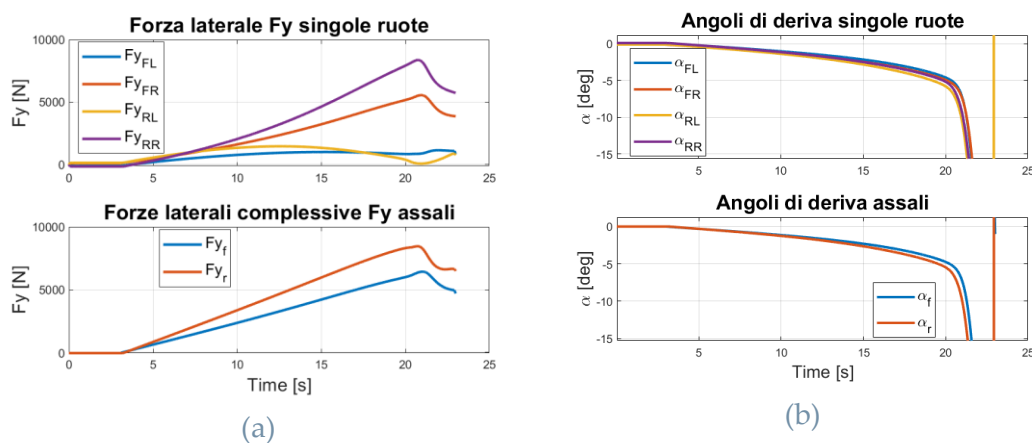


Figure 2.5:(a) Lateral Forces (b) Slip Angle as function of  $a_y$

Based on the data of lateral forces and slip angles, the cornering stiffness values were calculated as the derivative of the lateral force with respect to the slip angle, thus as the slope of the characteristic in the  $[\alpha-F_y]$  plane.

$$C_{\alpha_i} = -\frac{\partial F_{y_i}}{\partial \alpha_i}$$

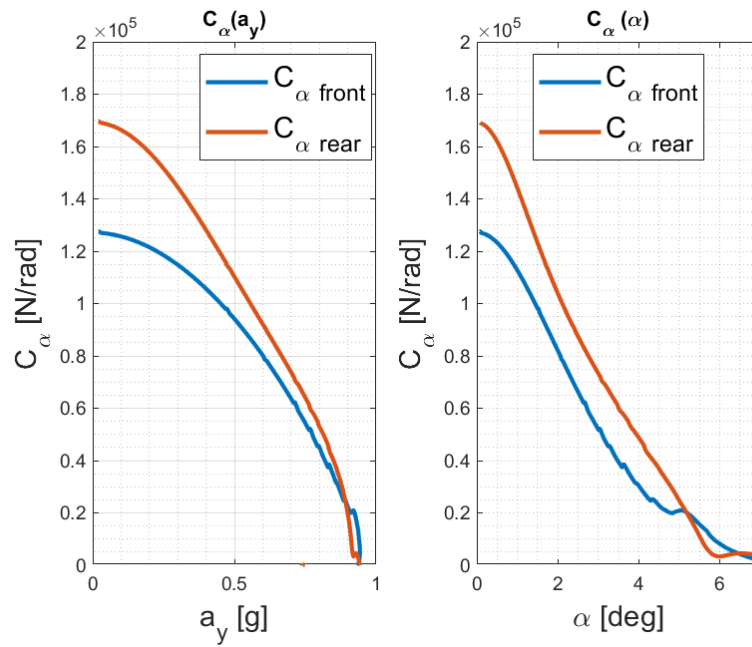


Figure 2.6: Cornering Stiffness

The selected values of cornering stiffness (approximation in linear field) around the origin are as follows:

$$C_{\alpha, f} = 1.2756 \cdot 10^5 \text{ N/rad}$$

$$C_{\alpha, r} = 1.6969 \cdot 10^5 \text{ N/rad}$$

### 2.3.3. Steady State Turning

It is important to note that, by assuming constant velocity, and thus constant values for the derivatives of stability, we reduce matrix  $A$  to an LTI (Linear Time-Invariant) matrix.

We can now visualize the system's stability by examining the signs of the eigenvalues of matrix  $A$  as the velocity  $v_x$  varies.

The graph in the complex plane in Figure 2.7: Root-Locus dependent on vehicle speed, shown below for the vehicle under analysis, is of particular interest. It illustrates the vehicle's oversteering nature. Under these conditions, the system's eigenvalues have no imaginary part, indicating that no oscillatory behavior is expected before reaching an unstable condition when  $\text{Re}(\lambda) > 0$ .

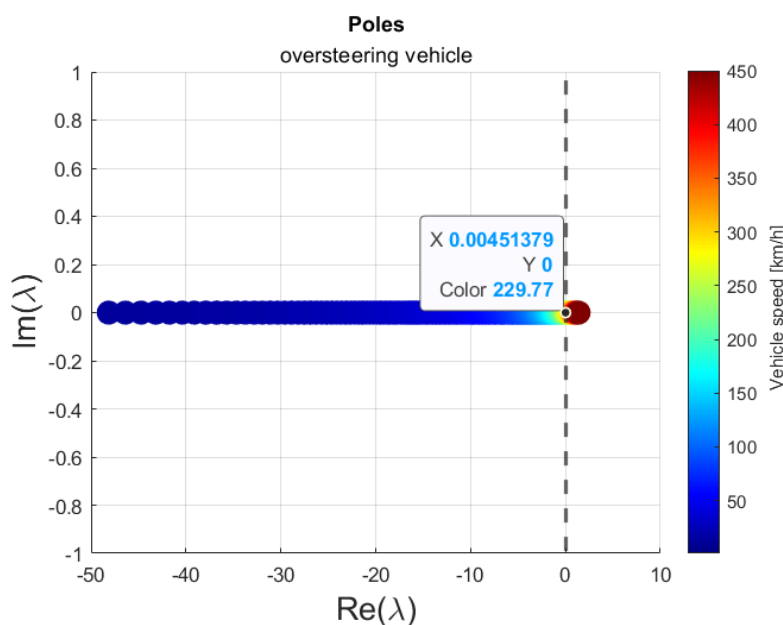


Figure 2.7: Root-Locus dependent on vehicle speed

#### 2.3.3.1. Understeering curve & Side Slip Angle curve

A vehicle is defined as understeering (oversteering), if more (less) steering angle to the wheels is required to increase the curvature  $\rho$  than in the case of kinematic steering. A neutral vehicle will require exactly the kinematic

steering angle to increase the curvature, which in case of small angle is directly proportional to vehicle wheelbase  $L$  and inversely proportional to  $R$ .

Like what was done in section 2.3.1, it is possible to evaluate the kinematic steering value from the simulation data as:

$$\delta_0 = \frac{L}{R} = L \cdot \frac{\dot{\psi}}{V}$$

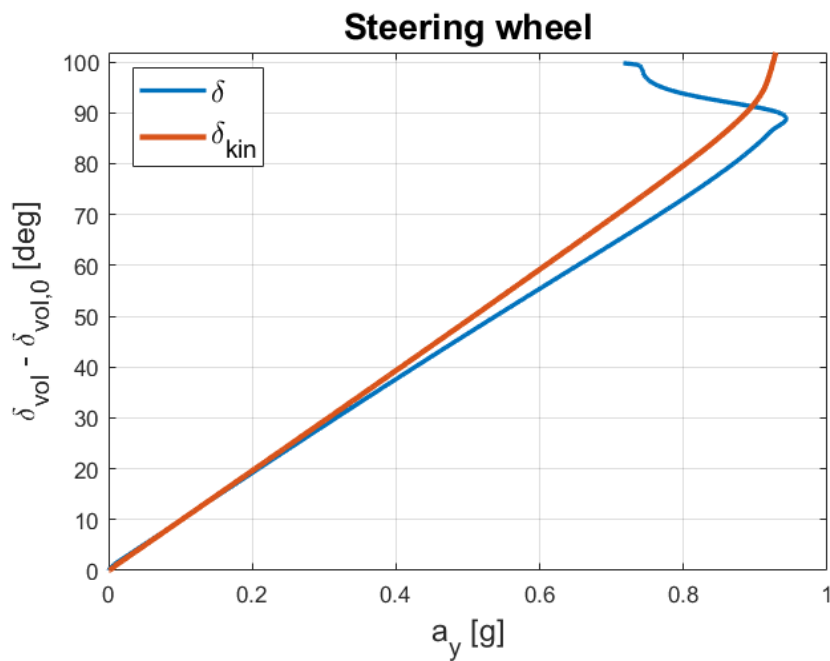


Figure 2.8: Steering angle: Compare with kinematic value.

The following expression is known as *understeering gradient*.

$$K_{us} = \frac{m}{l} \left( \frac{b}{C_{\alpha,f}} - \frac{a}{C_{\alpha,r}} \right) = -0.0367 \text{ deg}/(m/s^2)$$

Taking the steering ratio  $R_S$  into account, it is possible to express this value in terms of degrees at the steering wheel.

$$K_{us_{sw}} = \frac{m}{l} \left( \frac{b}{C_{\alpha,f}} - \frac{a}{C_{\alpha,r}} \right) \cdot R_S = -0.4769 \text{ deg}/(m/s^2)$$

From the expression of the *critical speed* in relation to the understeer gradient, we obtain:

$$V_{crit} = \sqrt{-\frac{L}{K_{us}}} = 229.4 \frac{km}{h}$$

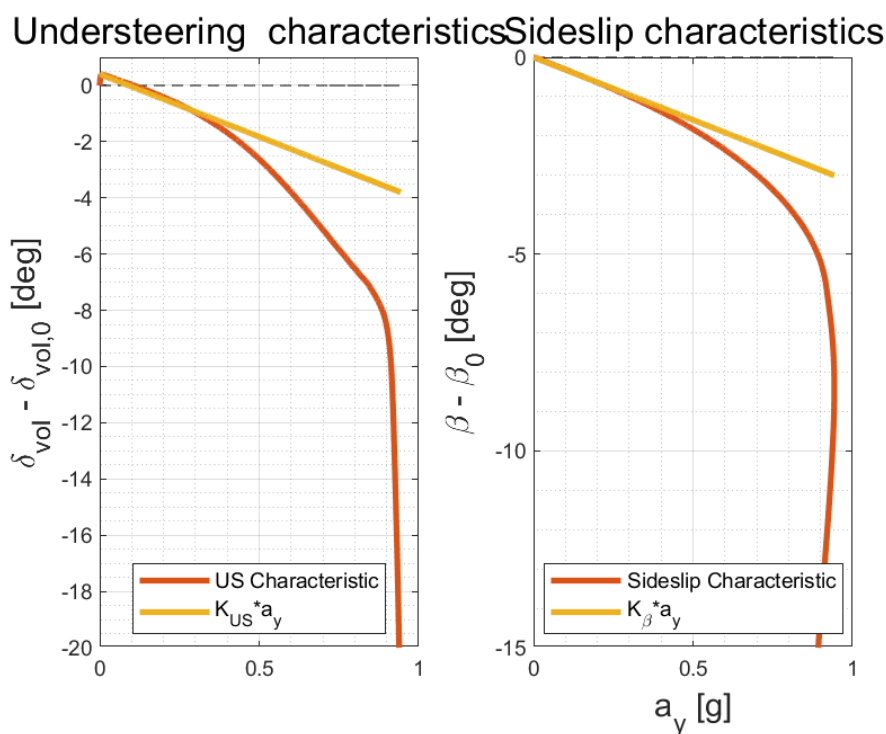
This value is consistent with what was derived in Figure 2.7: Root-Locus dependent on vehicle speed.

While the *sideslip gradient*:

$$K_{\beta} = -\frac{m_{rear}}{C_{\alpha,r}} = -0.3245 \text{ deg}/(m/s^2)$$

This characteristic of the lateral dynamics of a vehicle is shown in the plane  $[a_y, (\delta - \delta_{kin})]$ , the orange line shows the understeering characteristic of the vehicle within the linear field. This in fact overlaps to the characteristic obtained from the simulation data for small accelerations ( $<0.4g$ ).

Figure 2.9: Understeering and Sideslip Characteristics



### 2.3.4. Gain

The following responses define the more relevant steady-state output-input relationships of the vehicle.

For a constant forward speed  $v_x$  and for a constant input  $\delta$  the steady state output -input relationships are defined as follows:

$$\frac{\rho}{\delta} = \frac{1}{R\delta} = \frac{Y_\delta N_\beta - Y_\beta N_\delta}{v_x(N_r Y_\beta - Y_r N_\beta + m v_x N_\beta)} = \frac{1}{L + K_{US} V^2}$$

$$\frac{\beta}{\delta} = \frac{N_\delta(Y_r - m v_x) - N_r Y_\delta}{Y_r N_\beta - Y_r N_\beta + m v_x Y_\beta} = \frac{b + K_\beta V^2}{L + K_{US} V^2}$$

$$\frac{r}{\delta} = \frac{\rho}{\delta} v_x = \frac{Y_\delta N_\beta - Y_\beta N_\delta}{(N_r Y_\beta - Y_r N_\beta + m v_x N_\beta)} = \frac{V}{L + K_{US} V^2}$$

$$\frac{a_y}{\delta} = \frac{\rho}{\delta} v_x^2 = \frac{v_x(Y_\delta N_\beta - Y_\beta N_\delta)}{(N_r Y_\beta - Y_r N_\beta + m v_x N_\beta)} = \frac{V^2}{L + K_{US} V^2}$$

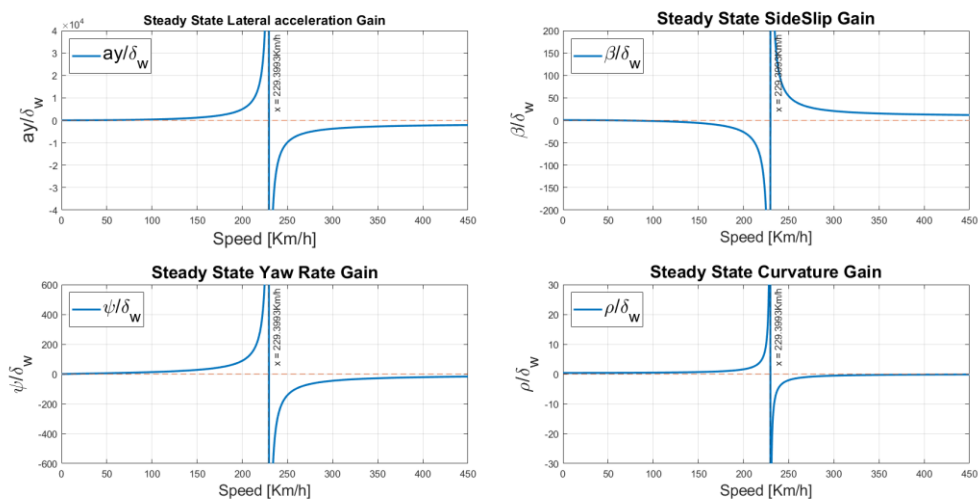
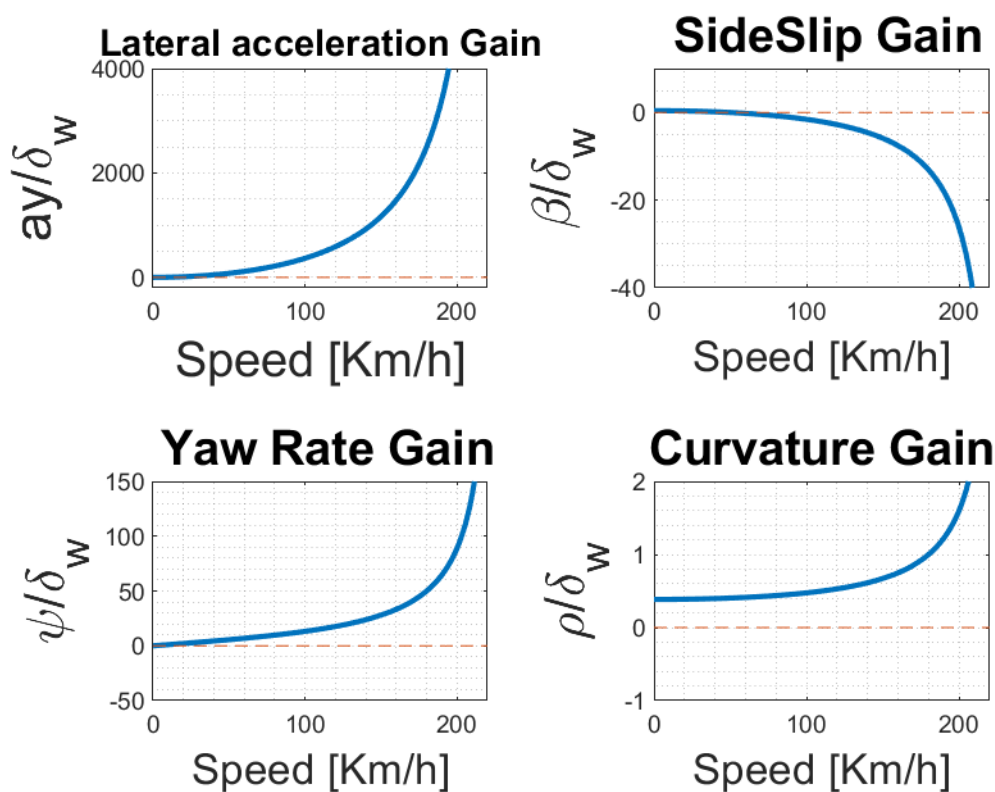


Figure 2.10: Gain

Looking at the graph related to the steady state curvature gain it is possible to state that the curvature for extremely low speed is coincident with respect to the condition of kinematic steering. Subsequently, the oversteering behaviour

becomes evident as the curvature grows up until, for a given vehicle speed (*critical speed*), it reaches infinite value. In this condition for a finite application of steering angle the curvature radius trajectory tends to zero and the centre of rotation is coincident with the vehicle centre of gravity: this condition is defined as *tailspin* and must be avoided. Above this value of speed, the curvature tends to zero for high value of speed. The critical speed value is consistent with what is defined in the graph Figure 2.7: Root-Locus dependent on vehicle speed.

The following provides the same information as the previous graph but with greater zoom into the stable operating range.



## 2.4. Cornering stiffness linearization around a fixed point.

The results obtained using the method analyzed in 1.1.2

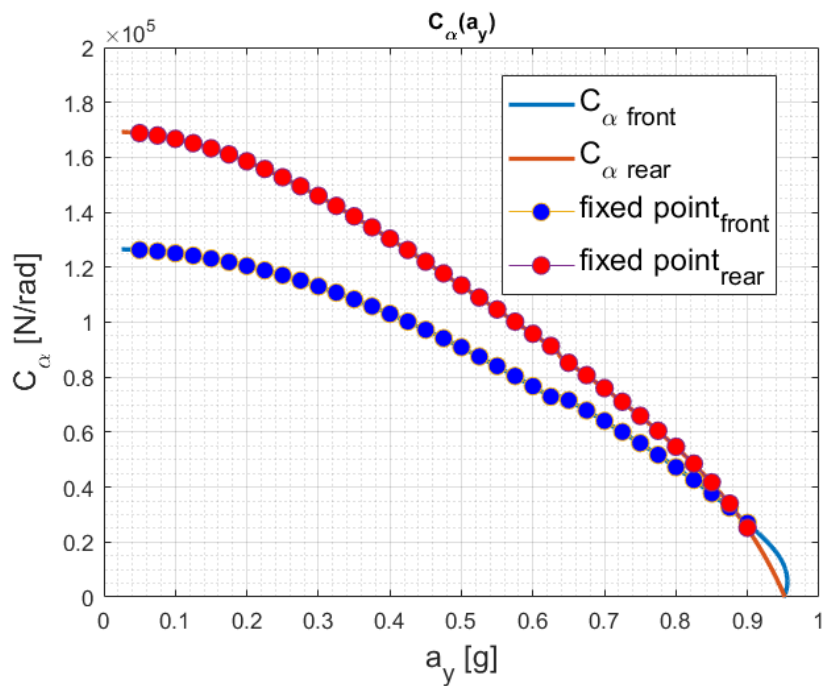


Figure 2.11: Cornering stiffness

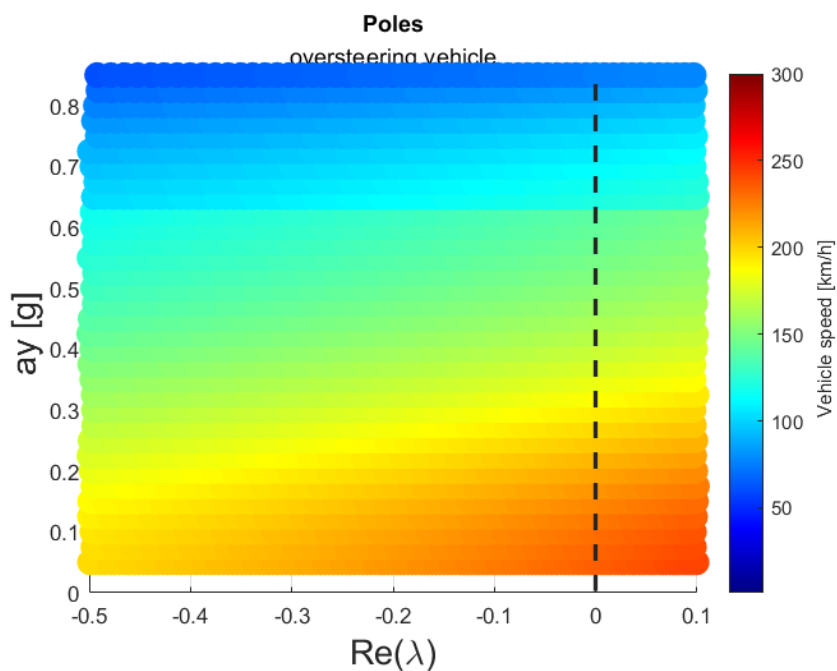


Figure 2.12: Real part eigenvalues of matrices  $\bar{A}$

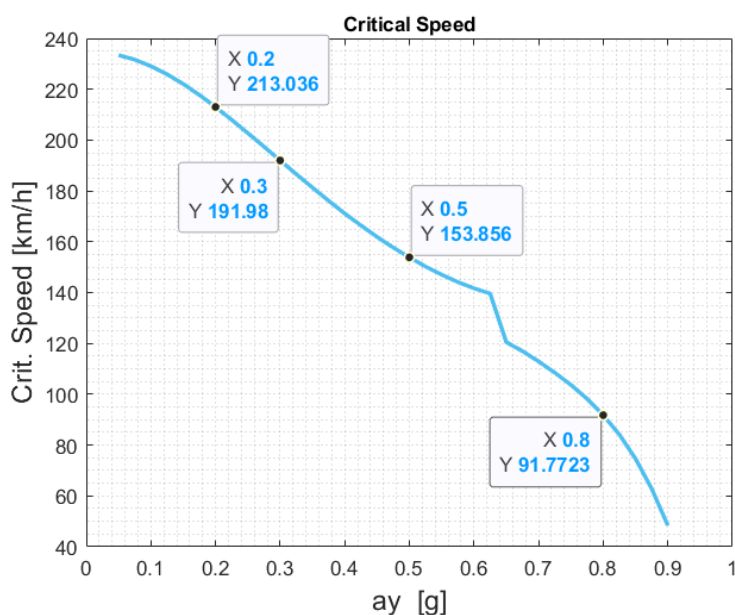


Figure 2.13: Critical Speed affected by lateral acceleration.

### Validation

To validate the model described above through simulation, several tests were conducted for different values of lateral acceleration. The manoeuvre considered involves a gradual approach to a given equilibrium condition, slow enough to neglect transient effects, followed by the maintenance of the desired equilibrium state. At a certain time instant ( $t_{start}$ ), a disturbance is applied to the system, specifically: an "impulse" on the throttle, starting from the initial condition corresponding to the throttle value required to maintain the vehicle at the desired constant speed, and increasing to a maximum limit, held for 1 second. This induces the rear axle (as the traction axle for the vehicle considered) to operate under conditions of higher longitudinal forces through the powertrain, which will lead, among other things, to a destabilization of the lateral forces relative to the equilibrium conditions. Below is a graph showing the throttle input for the simulations performed.

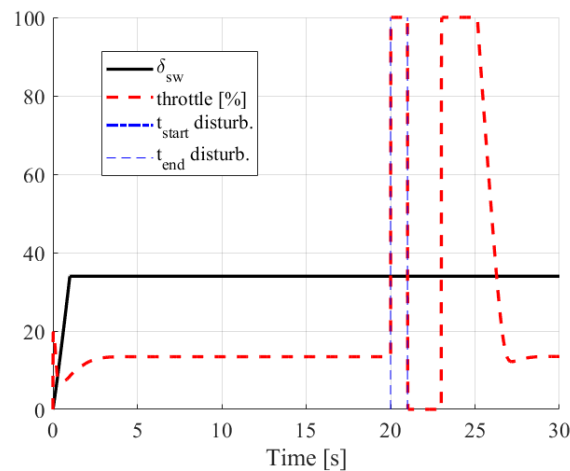


Figure 2.14: Input.

At the time instants when the disturbance is not applied (before  $t_{start}$  and after  $t_{end}$ ), the position of the throttle pedal is determined by the algorithm implemented in the model, which is responsible for maintaining a constant speed for that given equilibrium condition.

#### *Method*

To assess the consistency of the critical speed, values found as a function of lateral acceleration using the manoeuvres described above, two vehicle speed conditions will be simulated for each given value of lateral acceleration. Specifically, one condition will be below the critical speed, and the other will be at the critical speed for that value of lateral acceleration. What we expect to observe from these simulations is that for a speed below the identified critical speed, the application of the disturbance does not lead to divergence of the states and thus does not cause instability in the system. However, for a speed that coincides (within a sufficiently small range) with the critical speed, instability is expected to occur.

The critical speeds identified through simulation are consistent with those reported in Figure 2.13: Critical Speed affected by lateral .

The following will analyze some of the simulation parameters considered important in order to understand which of them are responsible for the various instability conditions. These graphs repeat similar trends for the different lateral acceleration conditions, and therefore it is deemed appropriate not to include them for each of the simulations conducted.

Simulation 1 :  $a_y=0.2g$ .

## -Tyre Forces

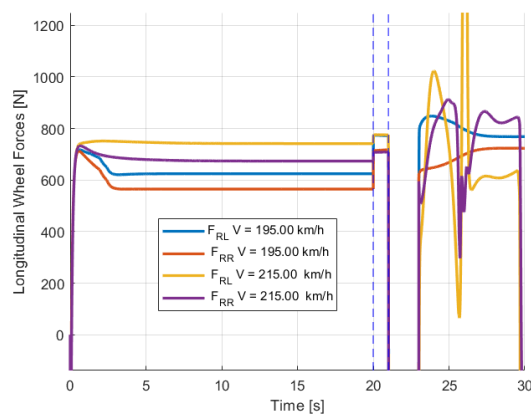


Figure 2.15: Longitudinal Rear Forces

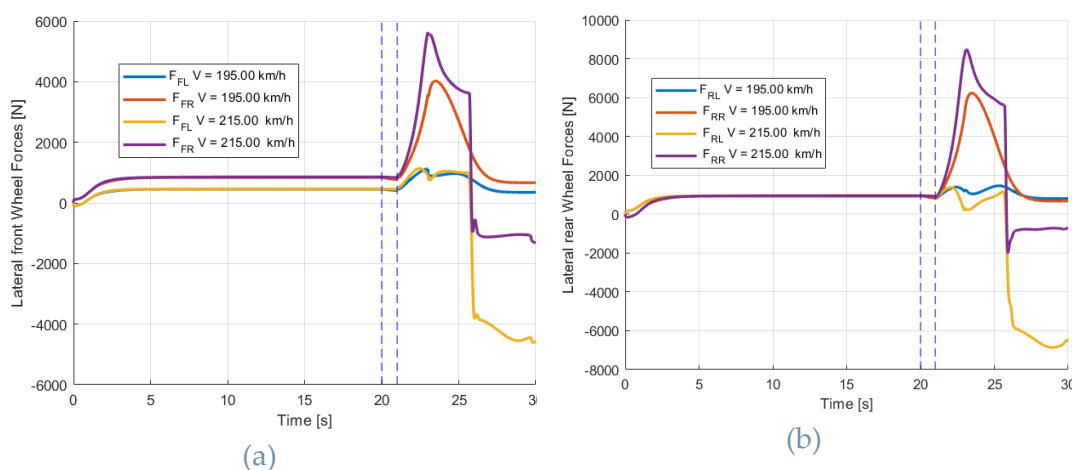


Figure 2.16: (a) Front Lateral Forces (b) Rear Lateral Forces

## - Tyre longitudinal slip and lateral slip

The following presents two of the quantities directly responsible for the vehicle's instability. In fact, the slip angles are the first to increase significantly in the case of an unstable simulation. Their increase also leads to a reduction in the axle's ability to generate not only lateral forces but also longitudinal forces, as confirmed by the subsequent rise in longitudinal slip. The vehicle reaches the so-called "spin-out" condition when the longitudinal slip reaches excessively high values, indicating that the axle is no longer able to exchange forces with the ground sufficient to maintain the vehicle in that specific

equilibrium state. For lower speeds than the identified critical speeds, the increase in slip angles is much more contained, allowing the vehicle to regain its equilibrium condition once the disturbance is no longer applied.

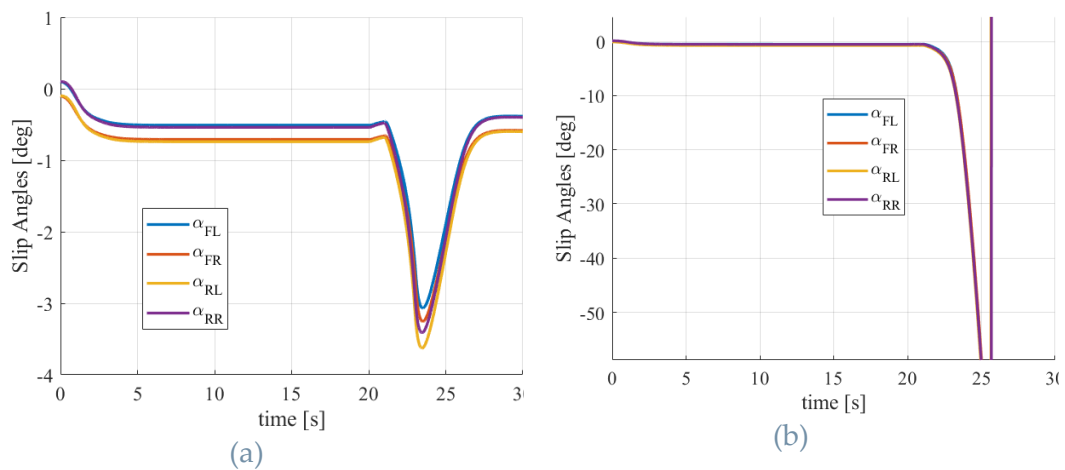


Figure 2.17 : Slip Angle (a) stable - (b) unstable

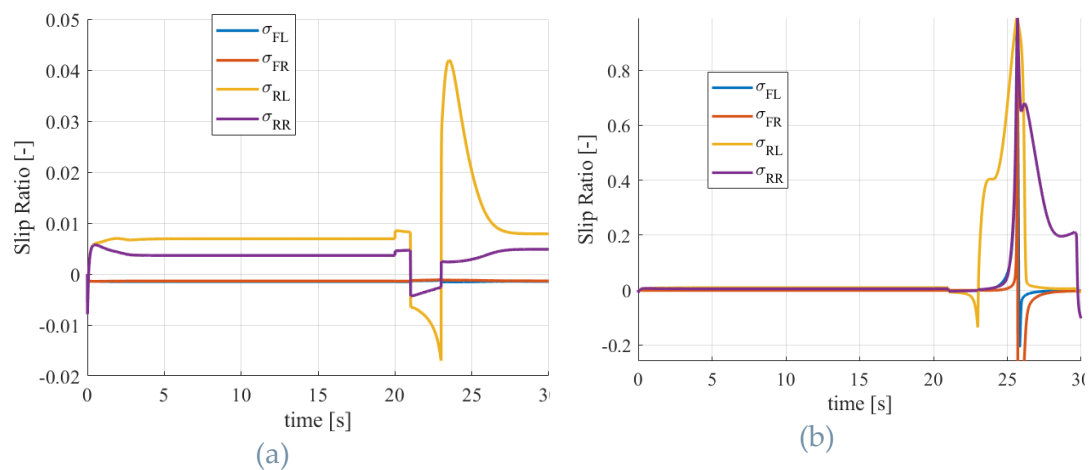


Figure 2.18 : Longitudinal Slip Ratio (a) stable - (b) unstable

### -Lateral Acceleration and side slip angle

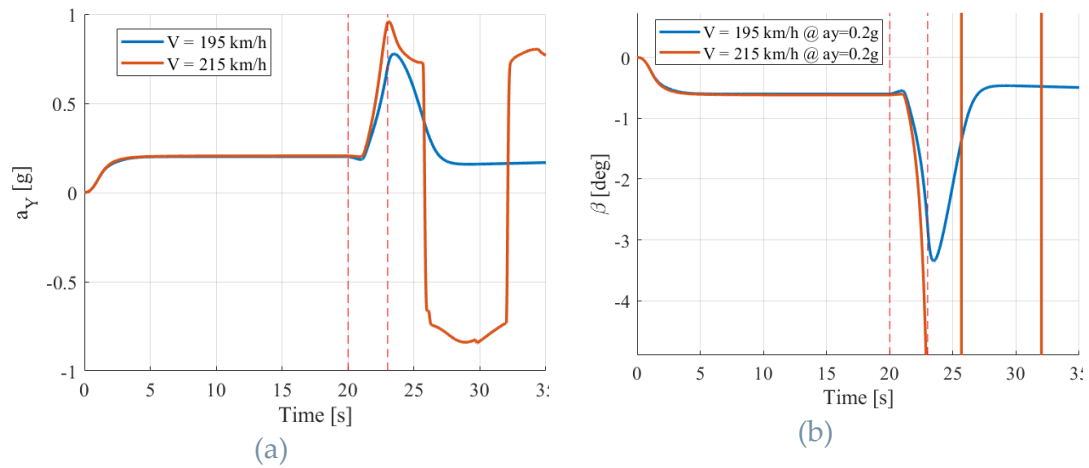


Figure 2.19: (a) lateral acceleration (b) side slip angle.

For the subsequent simulations with higher lateral acceleration values, only the graphs related to lateral acceleration are shown, as previously mentioned.

#### Simulation 2: $a_y = 0.3g$ .

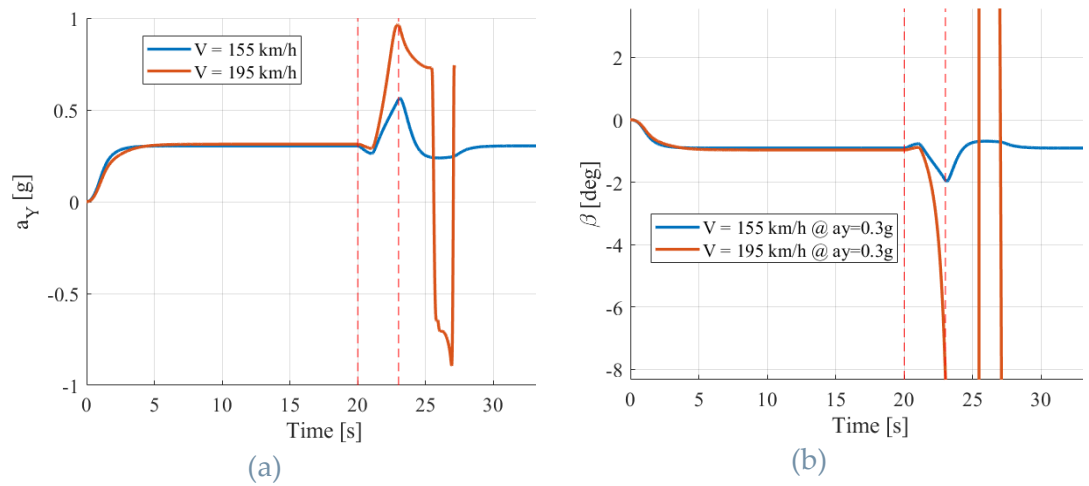


Figure 2.20:(a) lateral acceleration (b) side slip angle

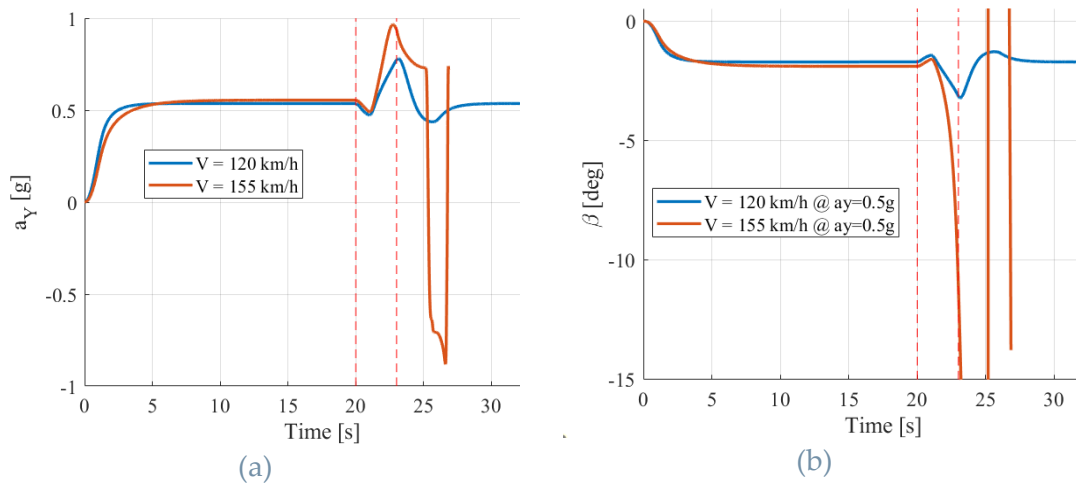
Simulation 3:  $a_y=0.5g$ .

Figure 2.21:(a) lateral acceleration (b) side slip angle

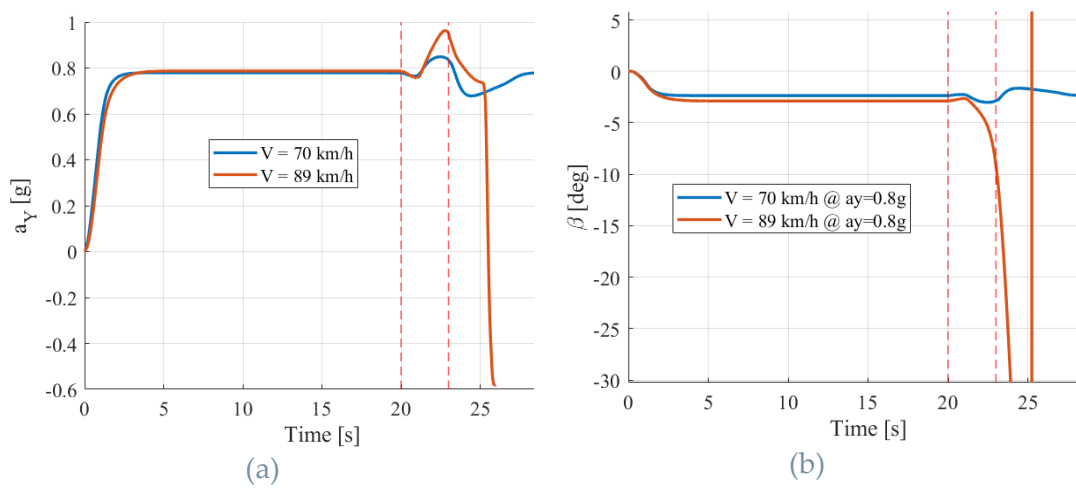
Simulation 4:  $a_y=0.8g$ .

Figure 2.22:(a) lateral acceleration (b) side slip angle

Later in the text these results will be further validated using the phase plane method discussed in 1.2.2.

## 2.5. Impact of road inclination on lateral dynamic.

In this section, an additional variable that can affect the vehicle's characteristic curves will be considered. This variable is the road inclination, which causes a longitudinal load transfer that, in extreme situations, can reduce or even increments the vehicle's stability range, particularly by altering its understeering coefficient and so its critical speed.

### 2.5.1. Implementation within the vehicle model.

The objective is to study the effect of longitudinal load transfer, caused by a longitudinal road inclination, on the vehicle's characteristic curves.

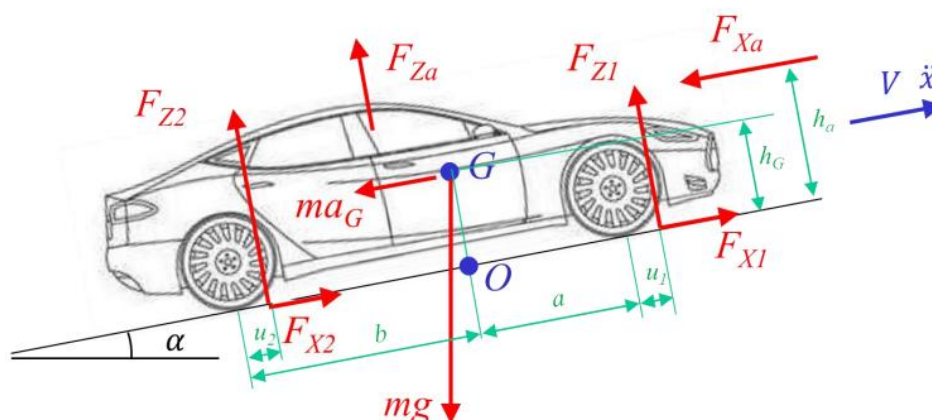


Figure 2.23: Free body diagram

Whit reference to the Figure 2.23: Free body diagram , the Equations of vertical forces are presented below, highlighting the contributions that have been added to the vehicle model to account for the road inclination  $\alpha$ .

$$F_{z_1} = mg \left( \frac{b}{L} \cos \alpha - \frac{h_g}{L} \sin \alpha \right) - \frac{m\ddot{x}h_G}{L} - \frac{F_{xa}h_a}{L}$$

$$F_{z_2} = mg \left( \frac{a}{L} \cos \alpha + \frac{h_g}{L} \sin \alpha \right) + \frac{m\ddot{x}h_G}{L} + \frac{F_{xa}h_a}{L}$$

Defining the road inclination as change in height along the length, we can write:

$$i = \tan \alpha$$

This term can be expressed as a percentage, where 100% corresponds to an angle  $\alpha = 45^\circ$ . The parameter  $i$  will represent the input value of the vehicle model: its implementation is provided below.

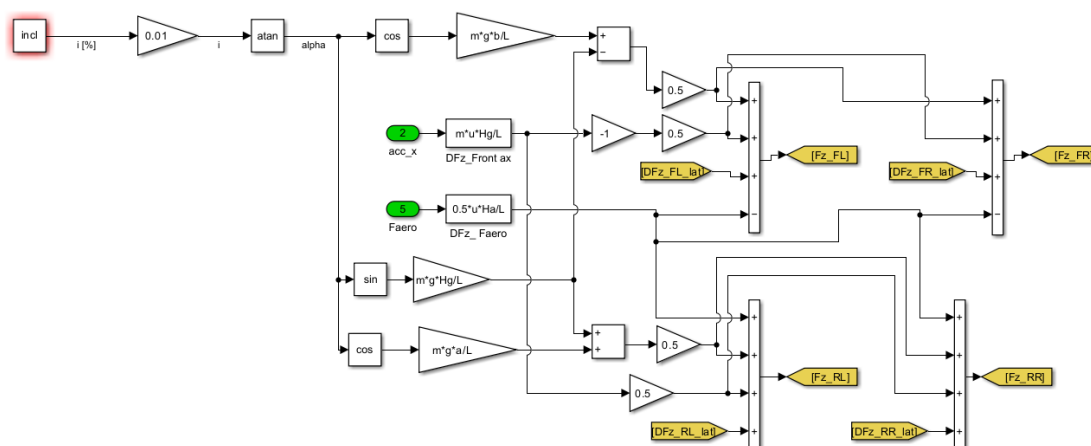


Figure 2.24: Normal forces computation, Block diagram

## 2.5.2. Effects on Critical Speed

In order to study the effects of road inclination, the same procedure as in the previous sections was repeated to identify new values for the cornering stiffness, understeer coefficients, and consequently critical speed. The table below shows the derived values.

Table 2.3: Cornering stiffness affected by road inclination

$i$	$C_{\alpha_f} \left[ \cdot 10^5 \frac{N}{rad} \right]$	$C_{\alpha_r} \left[ \cdot 10^5 \frac{N}{rad} \right]$	$K_{us} \left[ \frac{deg}{\frac{m}{s^2}} \right] \cdot R_s$
0%	1.26641	1.69519	-0.4539
5%	1.23859	1.72154	-0.3048
-5%	1.30840	1.66690	-0.6463

Referring to the work done in 2.3.4, it is possible to visualize the behaviour of the critical speed as a function of road inclination on the curvature gain graph.

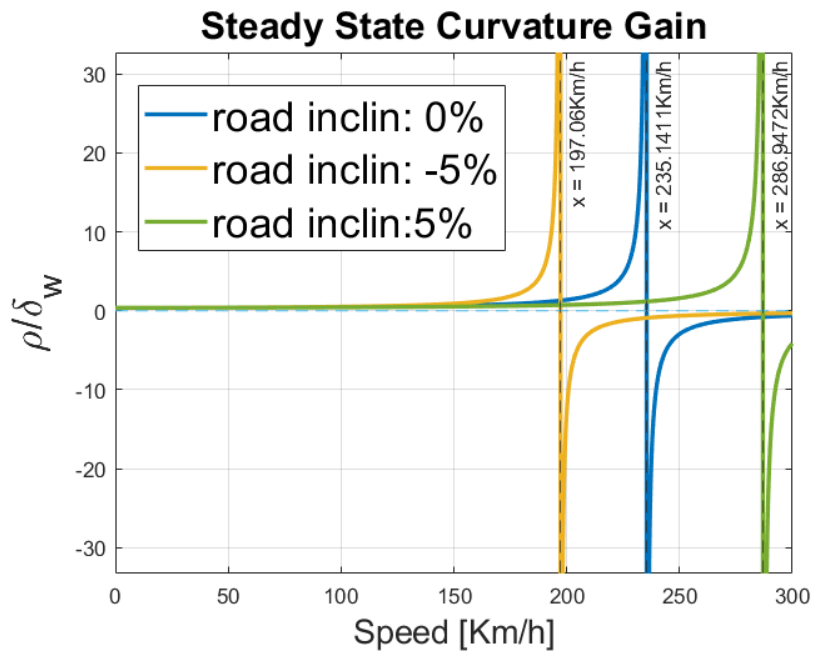


Figure 2.25: Critical Speed affected by road inclination

From this graph, it is evident that the critical condition occurs when the vehicle is in a downhill phase, which increases its oversteering tendency. For this reason, we have decided to explore this aspect in more detail by simulating negative slopes steeper than those typically encountered on highways (maximum 5%). This will be the topic of discussion in the next section.

### 2.5.3. Effect of negative slopes

As previously mentioned, the objective of this section is to examine the effect of extreme negative slopes. The characterization operations carried out previously were repeated over a wide range of inclinations, from 0% to -40%.

Let us now examine the effects on the cornering stiffness of the axles and their percentage variation with reference to the flat road scenario.

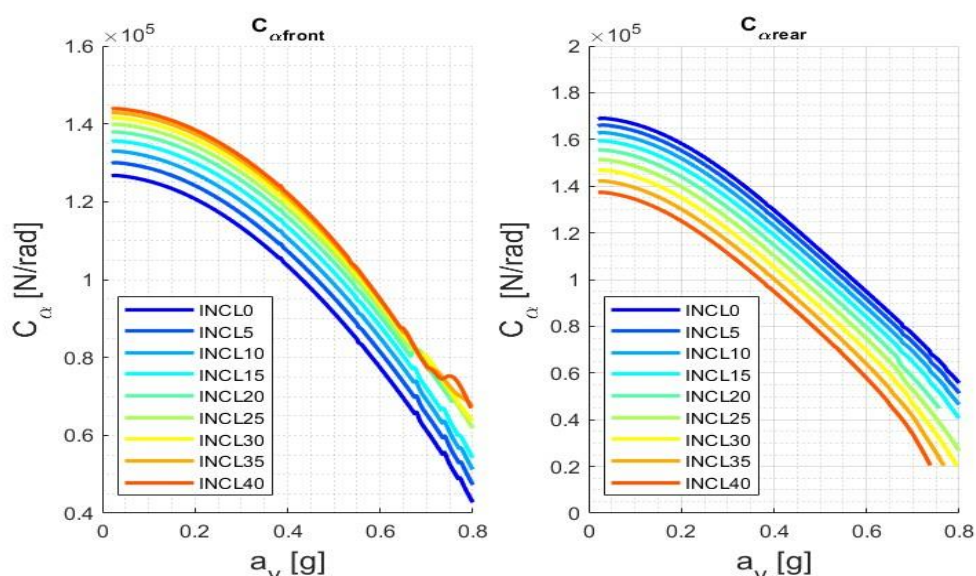


Figure 2.26: Cornering stiffness affected by negative road inclination

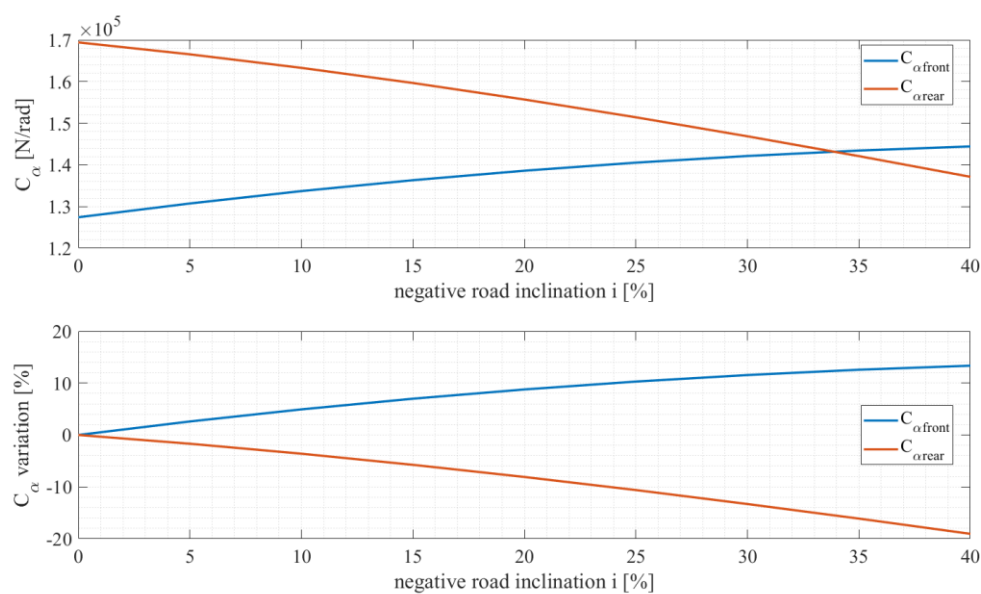


Figure 2.27: Cornering stiffness: Effect in terms of percentage variation

Similarly to what has been discussed so far, the values of the understeer gradient and its percentage variation are obtained as the road inclination changes.

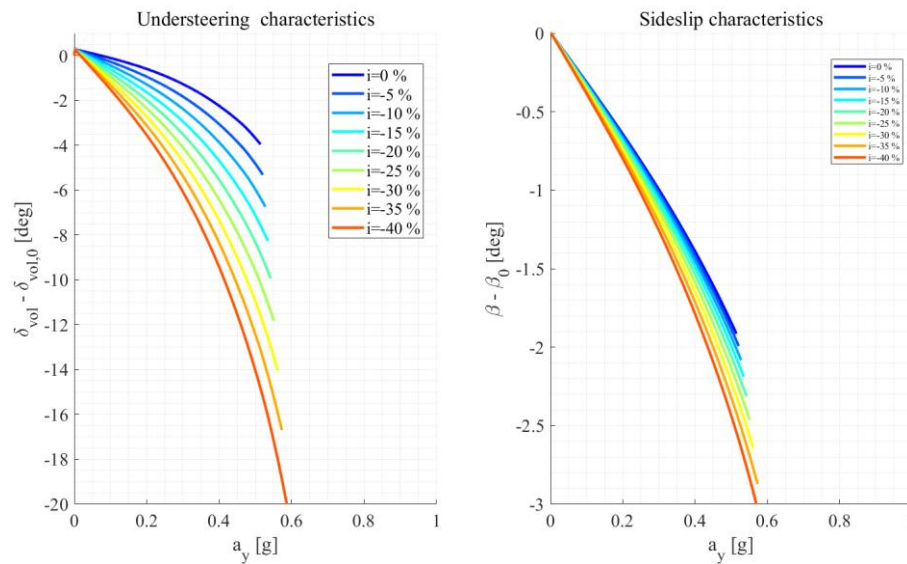


Figure 2.28: Characteristic curves affected by road inclination

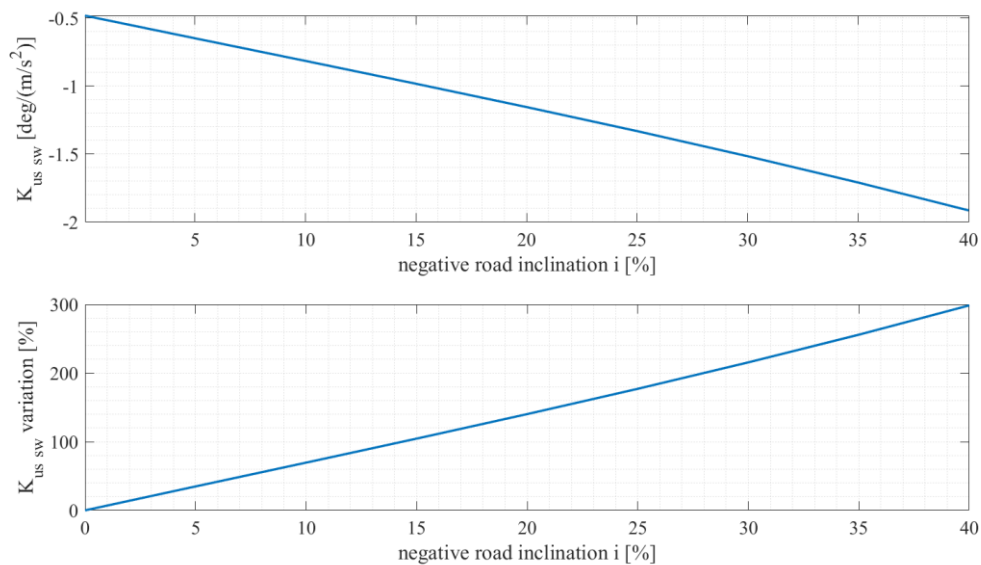


Figure 2.29: Understeering gradient: effect in terms of percentage variation

Finally, it is possible to show the effects of road inclination on the critical speed values calculated, as shown in 2.3.3.1.

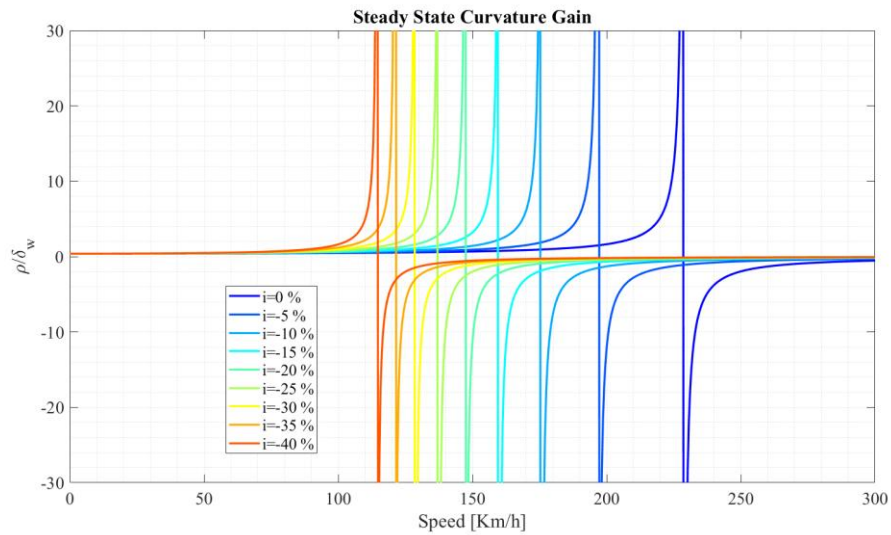


Figure 2.30: Critical speed affected by road inclination

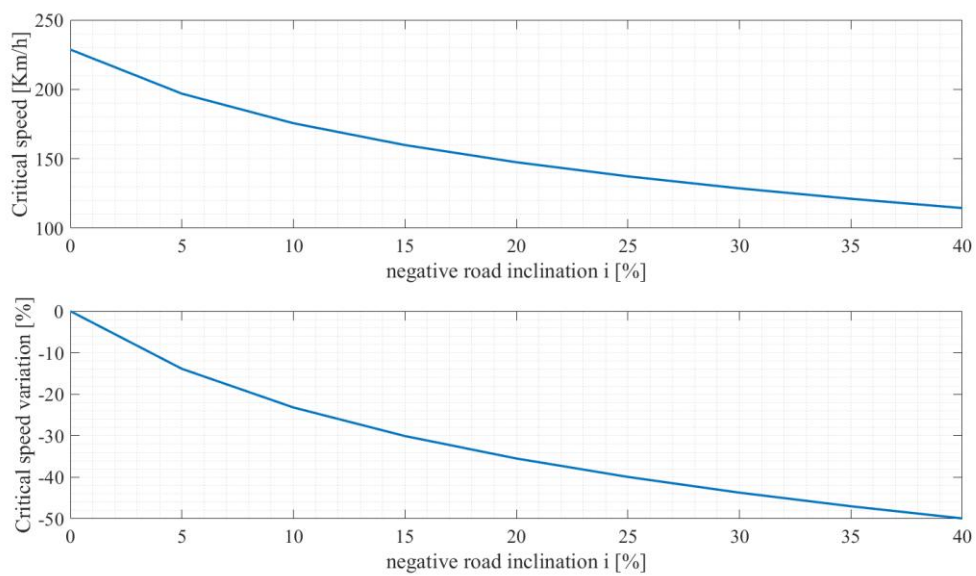


Figure 2.31: Critical speed: effect in terms of percentage variation

### 2.5.4. Effect on an Understeering vehicle

Based on what is shown in 2.5.3, it can be stated that the road inclination can alter the dynamic behaviour of the vehicle: in particular, this does not occur only with oversteering vehicles, but it is also possible to make a vehicle that is designed to be understeering, and thus asymptotically stable, unstable.

The objective of this paragraph is to demonstrate this phenomenon of instability in an understeering vehicle. Starting from the data in Table 2.1: Vehicle Data, by modifying the most relevant parameters, such as the load distribution and the percentage distribution of the anti-roll bars on the front axle, we can characterize an understeering vehicle when the road inclination is zero. In particular, starting from the oversteering vehicle analyzed in this text, the following modifications have been made:

- Weight distribution parameters, specifically with a 60% distribution on the front axle.
- Anti-roll bar distribution parameters between the front and rear, with 50% allocated to the front bars

Once its characteristic is defined, the objective is to show how a negative road inclination can lead to an oversteering behaviour instead.

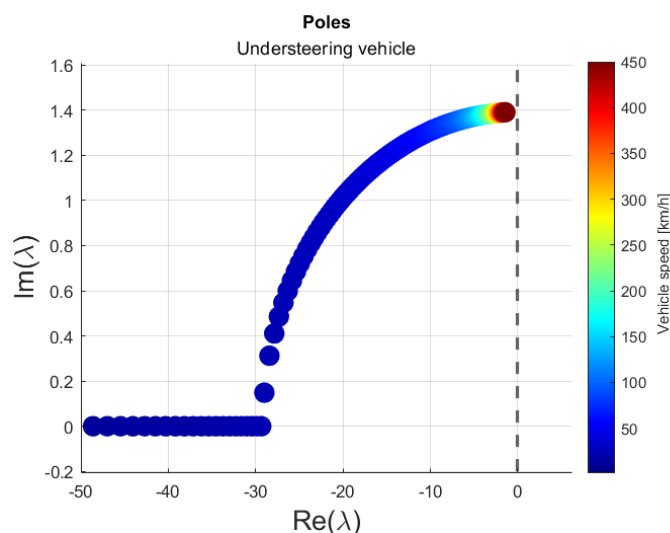


Figure 2.32: understeering vehicle root-locus

Instead, applying an inclination of  $i=-5\%$

Table 2.4:understeering to oversteering

$i$			
	$C_{\alpha_f} [\cdot 10^5 \frac{N}{rad}]$	$C_{\alpha_r} [\cdot 10^5 \frac{N}{rad}]$	$K_{us} \left[ \frac{deg}{\frac{m}{s^2}} \right] \cdot R_s$
0%	1.7684	1.2145	0.1184
-5%	1.7926	1.1779	-0.0581

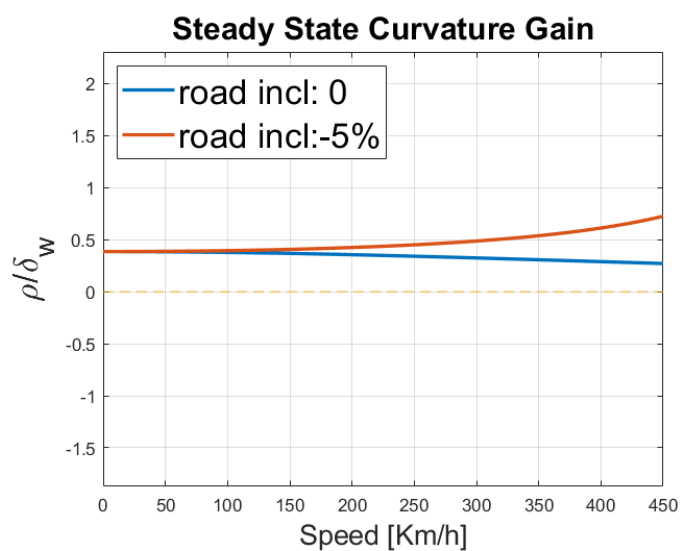


Figure 2.33:Understeering to oversteering

## 2.6. Impact of longitudinal acceleration on lateral dynamic.

In this section, an additional variable that can affect the vehicle's characteristic curves will be considered. This variable is the longitudinal acceleration, which causes a longitudinal load transfer that, in extreme situations, can reduce or even increments the vehicle's stability range, particularly by altering its understeering coefficient and so its critical speed.

### 2.6.1. Implementation within the vehicle model.

As with the study of road inclination, the effects of load transfer due to longitudinal acceleration will be analyzed by imposing a longitudinal acceleration value as input to the model. This input causes a load transfer to the tires, while the actual longitudinal acceleration of the vehicle remains the value required to maintain constant speed. It is therefore clear that this approach does not account for the effects of a given longitudinal acceleration on changes in speed or on the increase in the longitudinal forces transmitted from the tire to the road. Consequently, the study is limited to analyzing the contribution of longitudinal load transfer in relation to the vehicle's lateral dynamics.

### 2.6.2. Effect on cornering stiffness

Let us now examine the effects on the cornering stiffness of the axles and their percentage variation with reference to the zero longitudinal acceleration scenario.

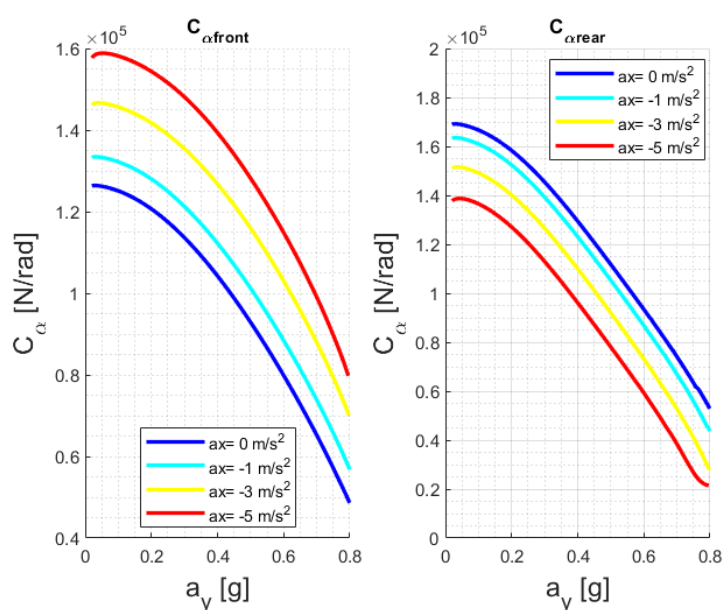


Figure 2.34: Cornering stiffness affected by ax

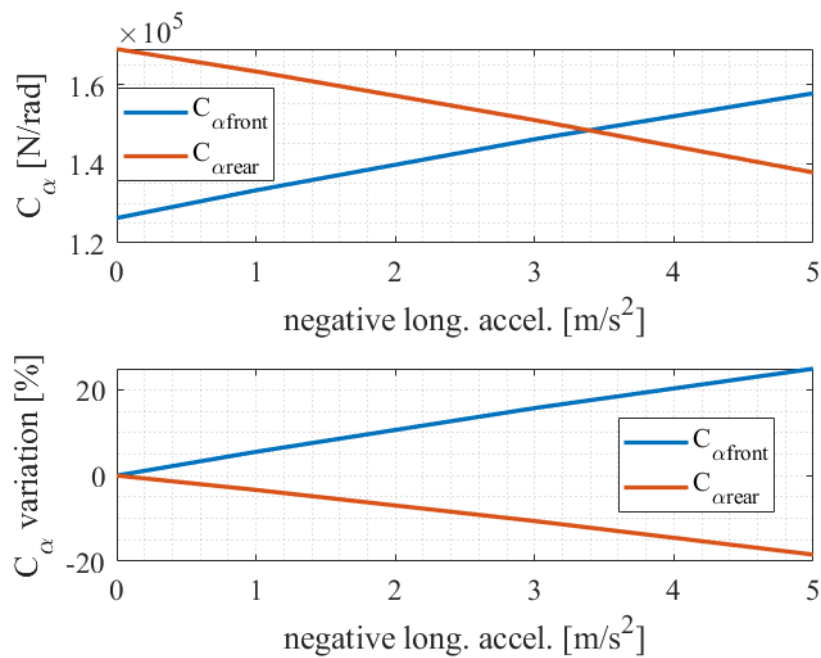


Figure 2.35: Cornering stiffness percentage variation

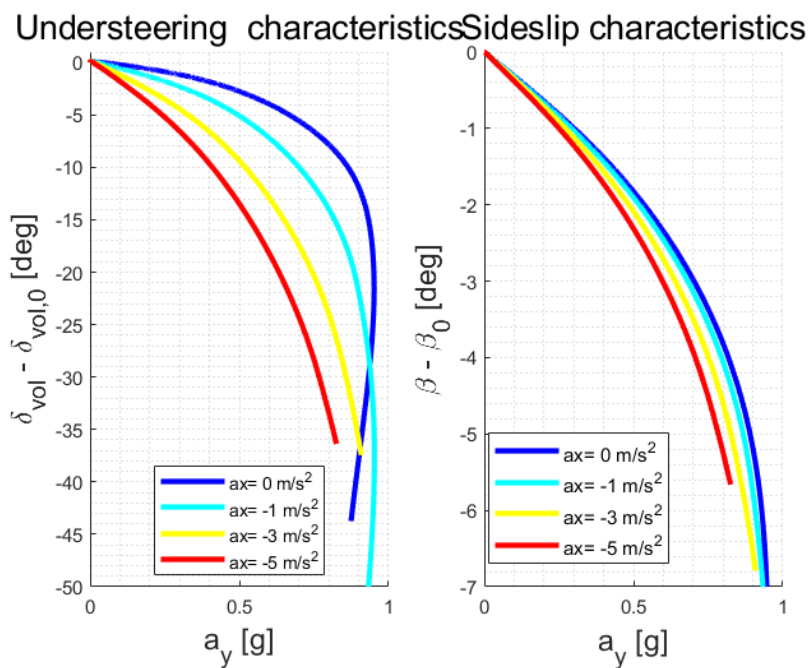


Figure 2.36: Characteristic curves affected by long. accel.

Finally, it is possible to show the effects of road inclination on the critical speed values calculated, as shown in 2.3.3.1.

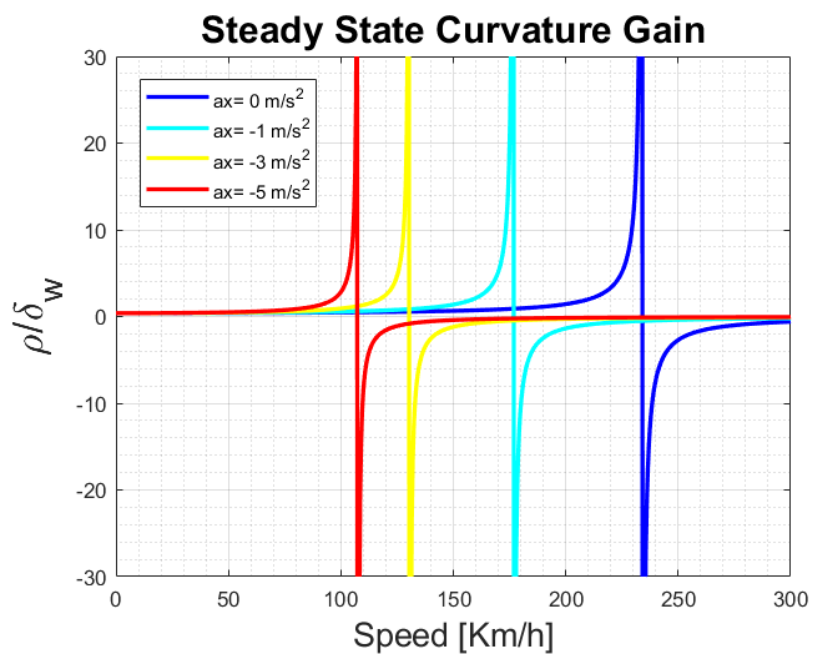


Figure 2.37: Critical speed affected by long. accel.

### 2.6.3. Combined effect of negative acceleration and negative road inclination

As can be seen from the sections. 2.5 and 2.6, both the effect of a negative road slope and the effect of vehicle deceleration contribute to a progressive increase in the vehicle's oversteering behavior. The goal of this section is to highlight how the combined effect of these two phenomena can lead to critical driving situations. The combined impact of these two factors is likely to occur; for example, consider a downhill mountain road. As soon as a hairpin curve approaches, the instinctive response is to reduce the vehicle's speed by applying the brakes, resulting in deceleration and consequently a load transfer to the front axle. In such a situation, where the slope and deceleration are not negligible, instability can occur even in a vehicle that is prone to understeering.

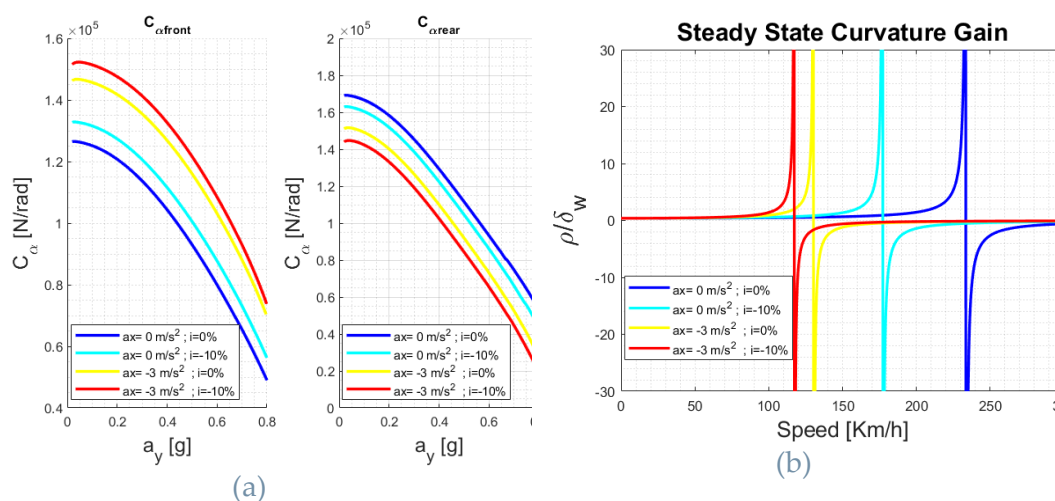


Figure 2.38 : Combine effect of deceleration and negative road inclination.

## 2.7. Impact of friction coefficient on lateral dynamic.

A similar analysis to the one conducted in 2.5 is presented in this section, with the aim of studying the effects of variations in the tire-road friction coefficient. We will specifically examine how this parameter influences the lateral behaviour of the vehicle.

Let us now examine the effects on the cornering stiffness of the axles and their percentage variation with reference to the unitary friction coefficient.

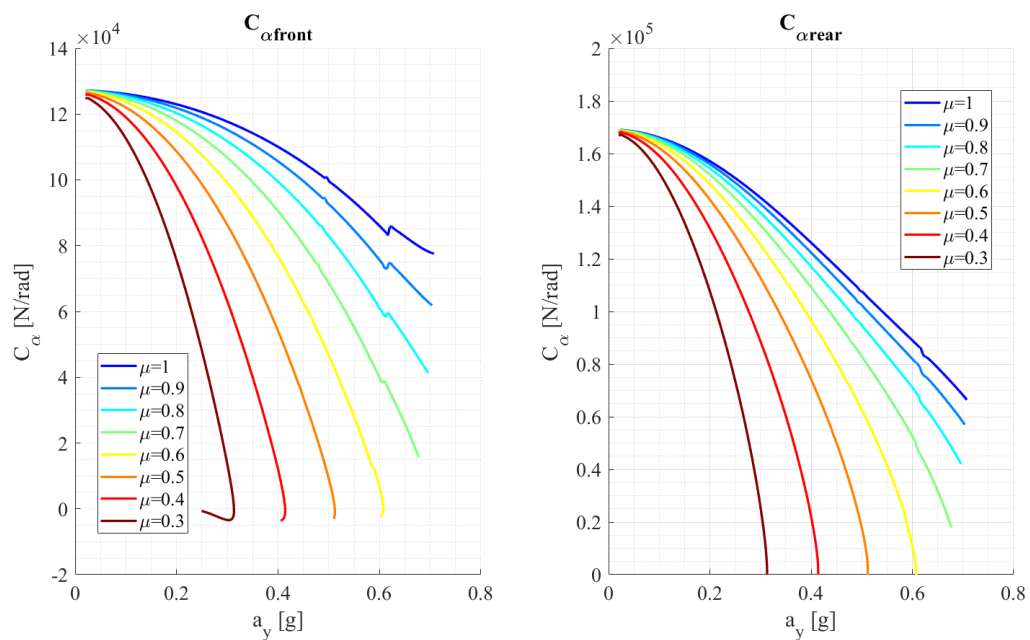


Figure 2.39: Cornering stiffness affected by friction coefficient

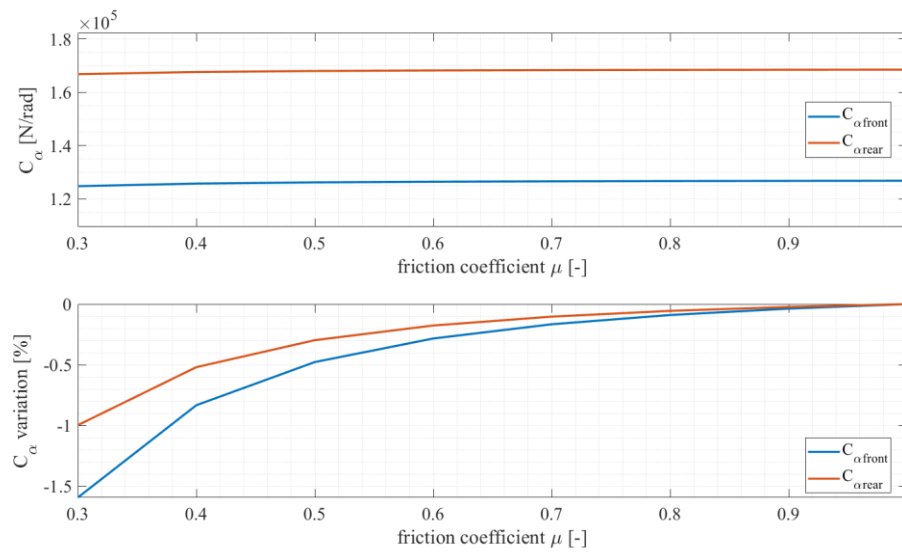


Figure 2.40: Cornering stiffness: Effect in terms of percentage variation

Similarly to what has been discussed so far, the values of the understeer gradient and its percentage variation (around the origin) are obtained as the friction coefficient changes. In this case, it is interesting to note how, as the lateral acceleration increases, the vehicle's behaviour tends to become more understeering.

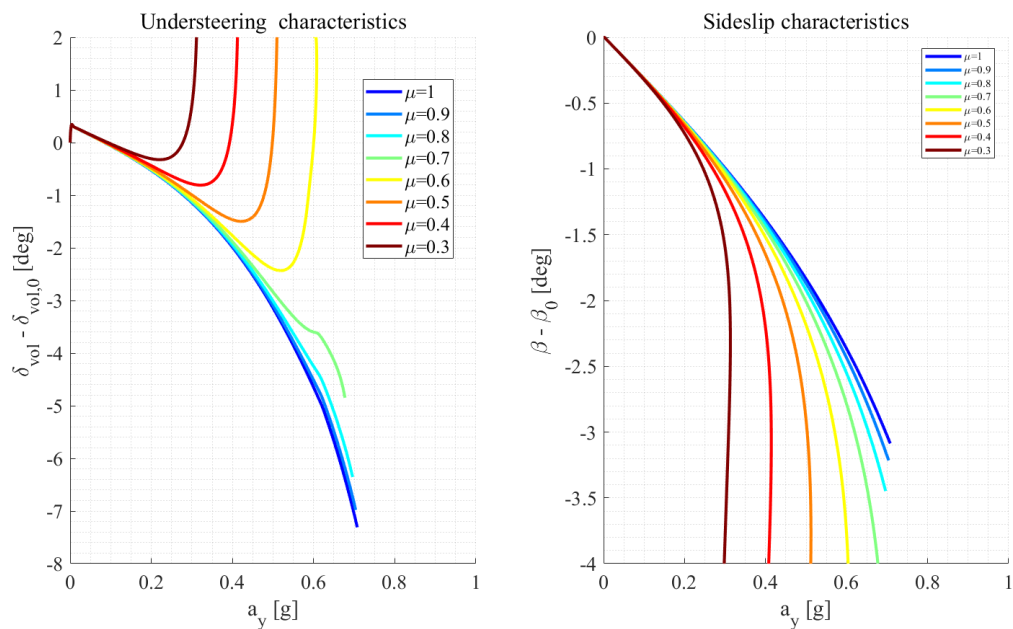


Figure 2.41: Characteristic curves affected by friction coefficient

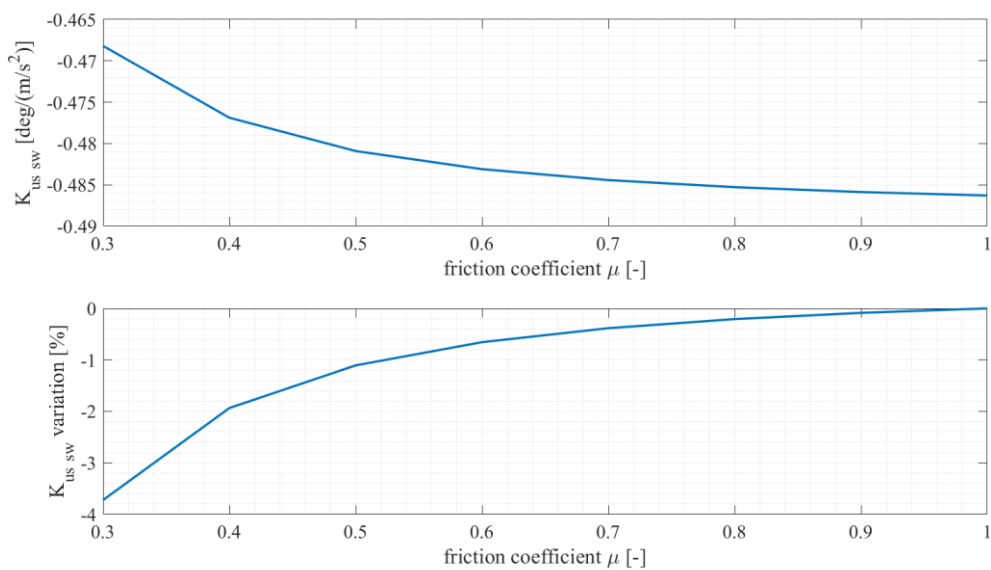


Figure 2.42: Understeering gradient: effect in terms of percentage variation

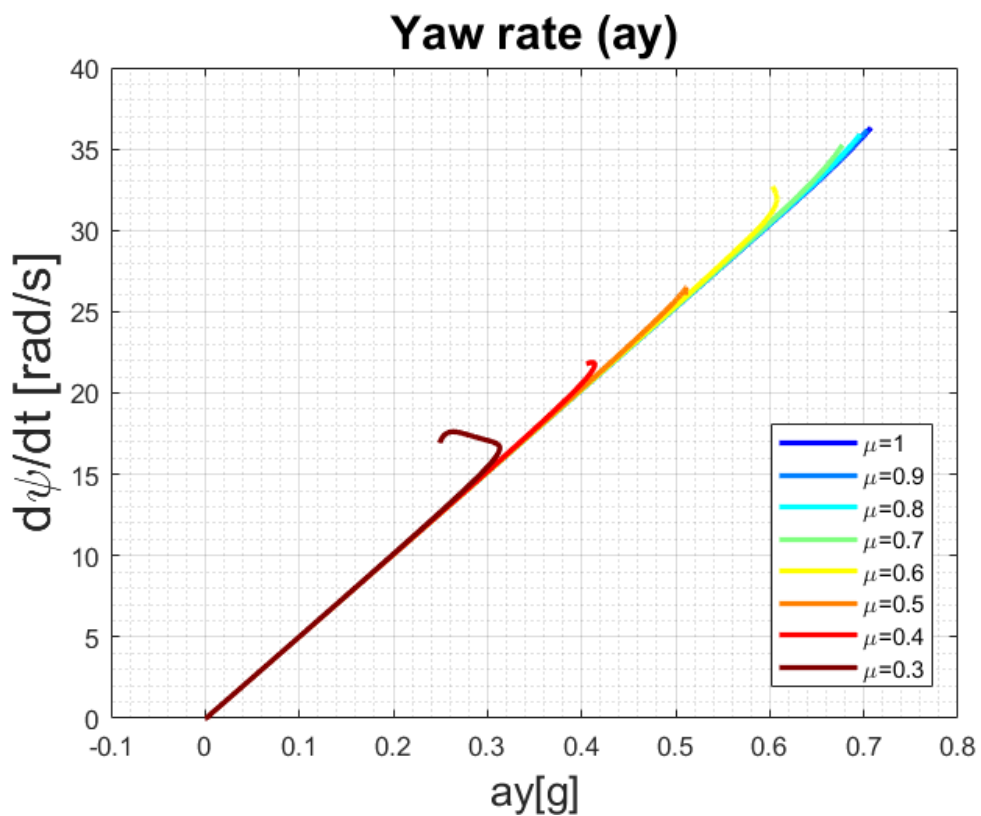


Figure 2.43: Yaw rate characteristic affected by friction coefficient

The effect on the critical speed, obtained as in 2.5.3 is not significant since the cornering stiffness values for small lateral accelerations are not noticeably influenced by the adhesion coefficients.

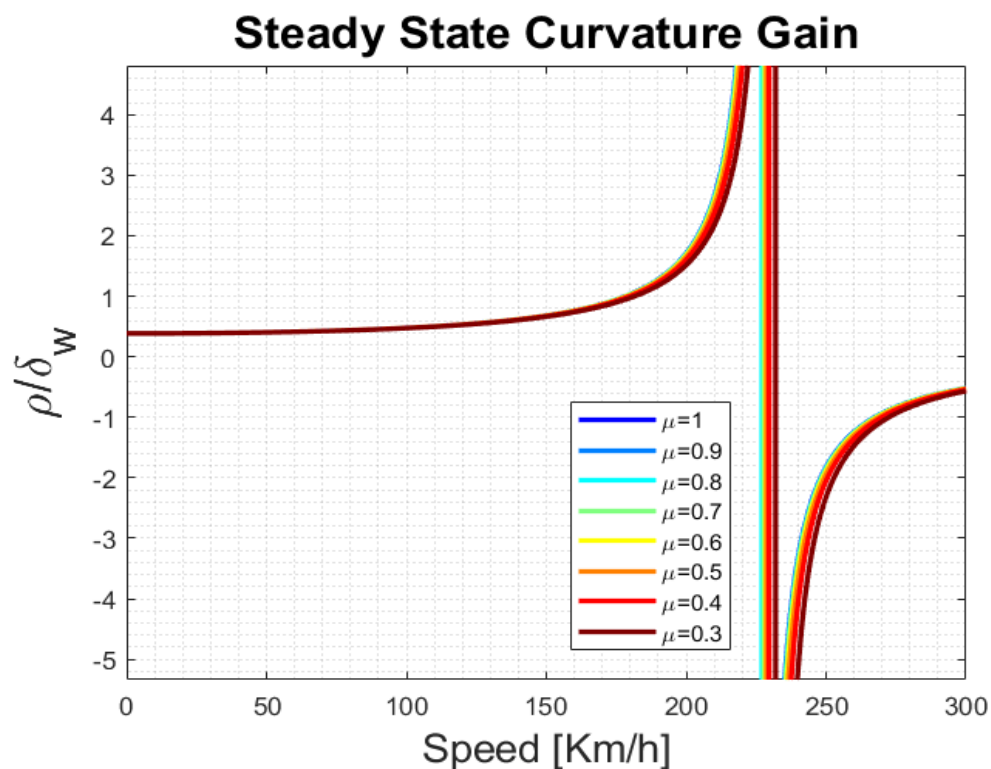


Figure 2.44: Critical speed affected by friction coefficient

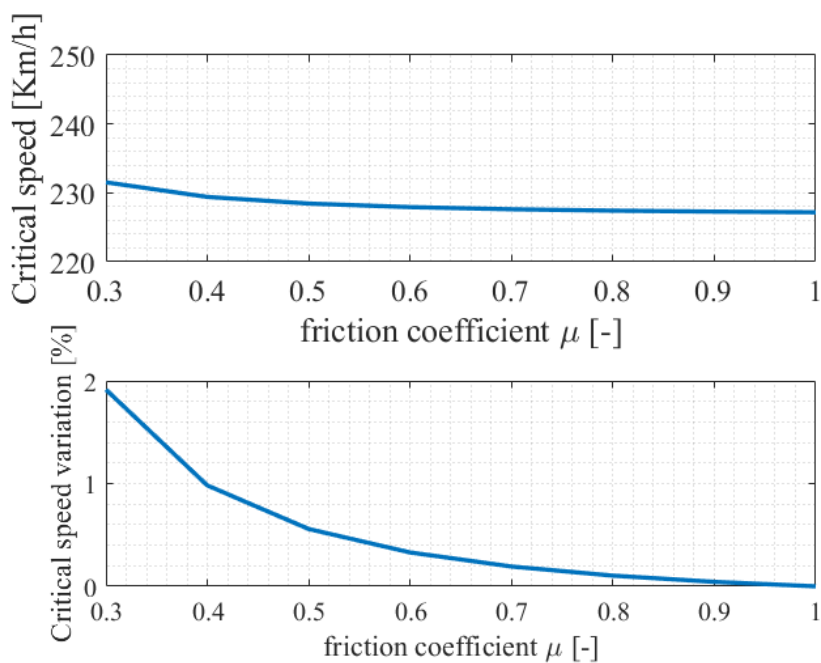


Figure 2.45: Critical speed: effect in terms of percentage variation

## 2.8. Characteristic of the axles through the tire model

With reference to the model discussed in **Errore. L'origine riferimento non è stata trovata.** we present below the results obtained, which will then be compared to those obtained by the equations of the single-track model from the simulations of ramp steer of the complete vehicle model discussed in 1.1.3. In addition, other tire parameters will be analyzed as parameters that could alter the characteristics of the vehicle.

### 2.8.1. Results

The following shows the results obtained using the model just described.

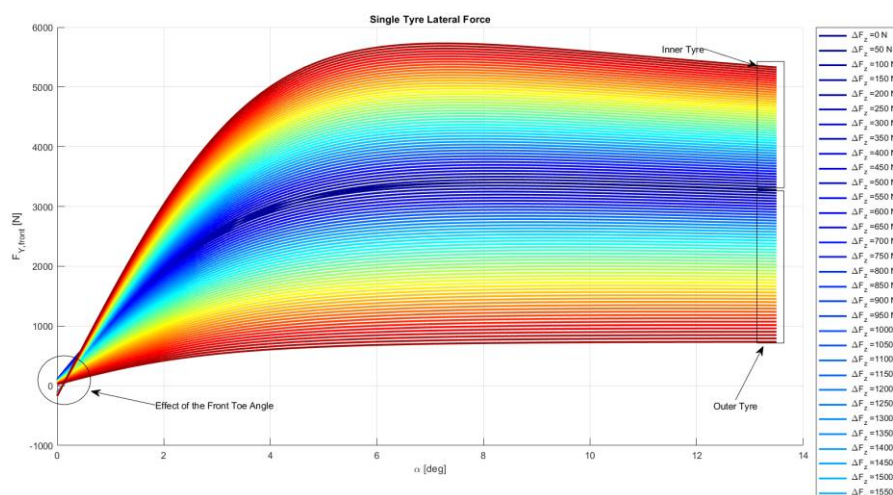


Figure 2.46 : Single tyre Lateral Front Forces affected by load transfer

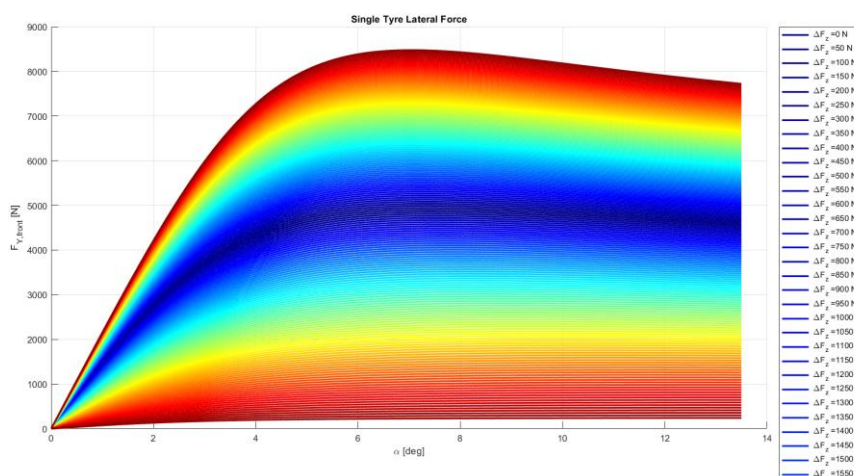


Figure 2.47 : Single tyre Lateral Rear Forces affected by load transfer

For the method to be valid, there must be a correspondence between the curve obtained using the coefficients  $\eta_f$  and  $\eta_r$ , which describe the lateral force variation with respect to the load transfer  $\Delta F_z$ , and the actual characteristic obtained through the simulation of the nonlinear model. In this regard, the following figure shows the two overlapping curves.

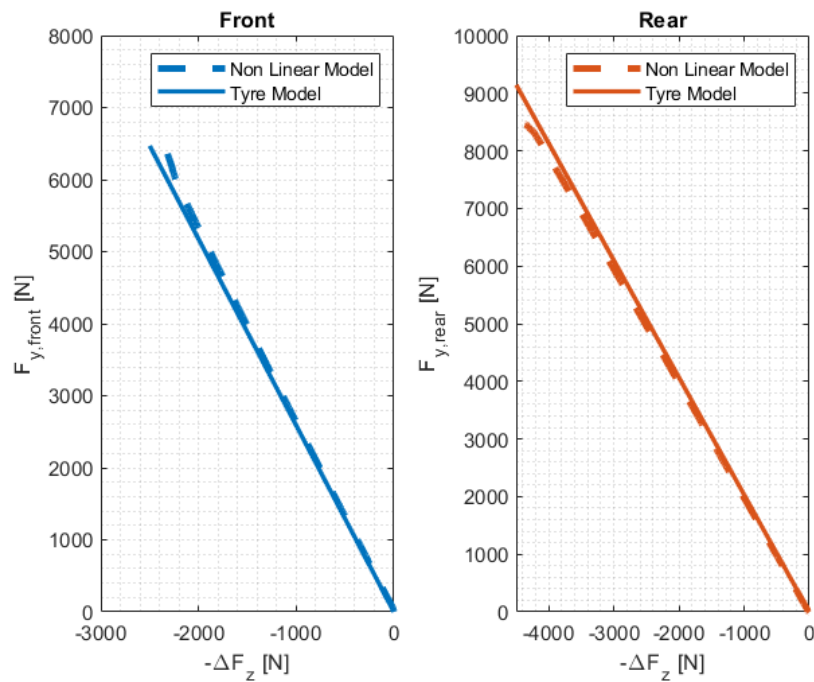


Figure 2.48 :  $F_y(\Delta F_z)$  compare between nonlinear and tyre model

Once this characteristic has been verified, it is now possible, following the steps described in the previous section, to evaluate the axle characterization point by point.

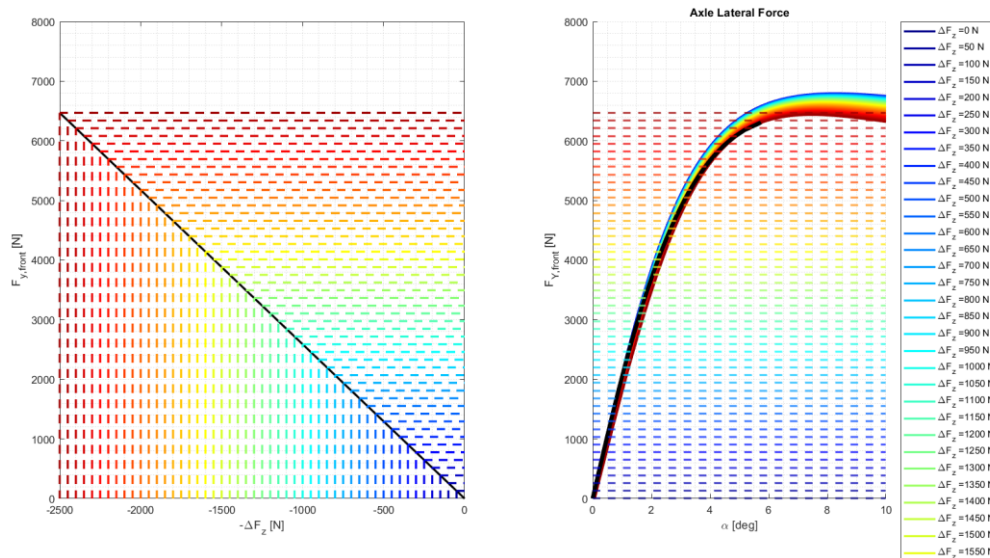


Figure 2.49 : Computation of the Front Axle characteristic

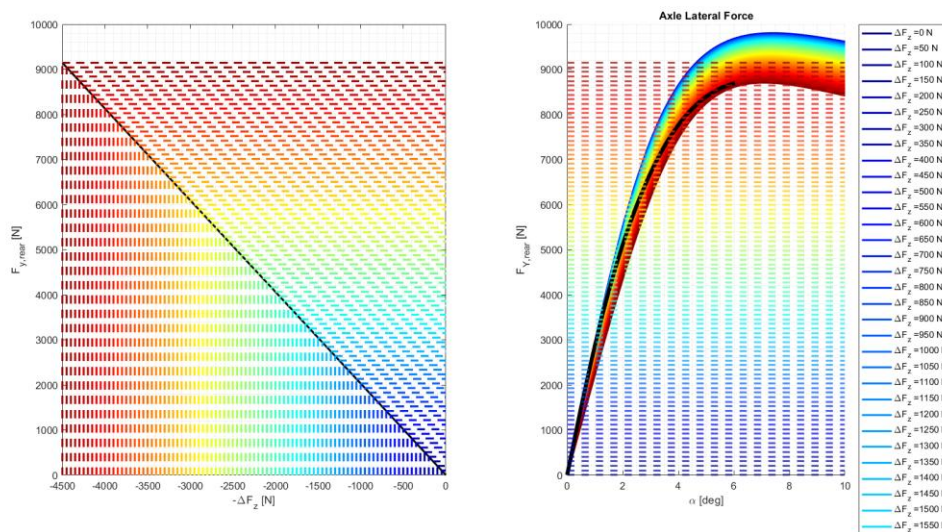


Figure 2.50 : Computation of the Rear Axle characteristic

Beyond the maximum lateral acceleration limit, no further increase in load transfer occurs, and the intersection considered so far loses its significance. Under these conditions, which are no longer of a stationary nature, the characteristic curves were obtained by taking as a reference the lateral force characteristic at the maximum load transfer limit. Below, the two obtained curves are presented in detail.

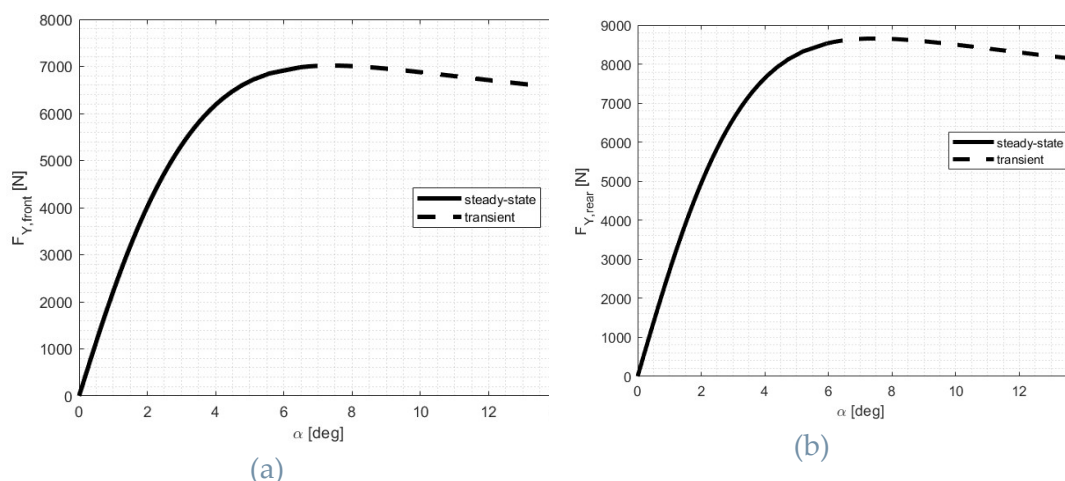


Figure 2.51 : Front (a) and Rear (b) Tyre characteristic

The results obtained in terms of axle characteristics () using the method described in this section are now compared with the results obtained through the ramp steer maneuver, as presented in section 2.3 Figure 2.6, with respect to the nonlinear model.

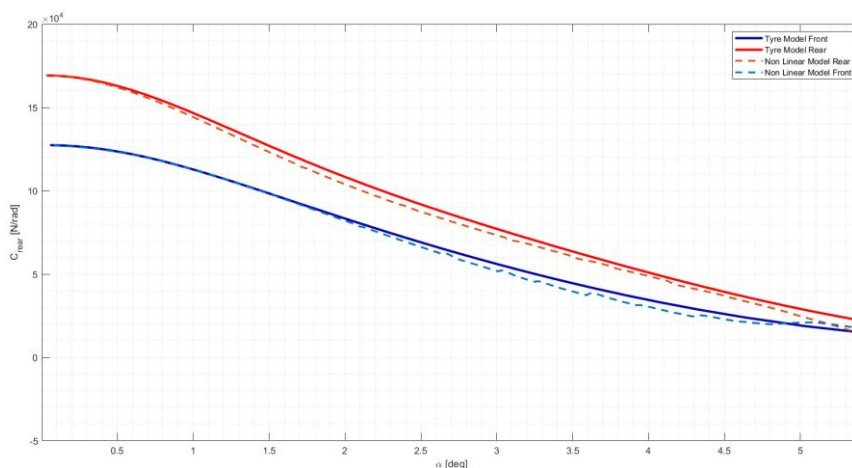


Figure 2.52 : Cornering Stiffness compare between non-linear and tyre model

It is interesting to note that through this comparison, it can be affirmed that the point-by-point construction method for the axle characteristic is capable of accurately describing how the axles behave as the slip angles change. This result is very important because it allows the axle characteristics to be

described without the need for nonlinear field simulations, thus reducing the computational time of the process. Therefore, knowing the geometry of the roll centers, roll gradient, vehicle roll stiffness (broken down in terms of springs and anti-roll bars), weight distribution, and the Pacejka model parameters dependent on tire properties is sufficient to estimate the axle characteristics with good approximation. These characteristics are directly responsible for the dynamic behavior of the vehicle.

This method also, as mentioned earlier, allows for a detailed analysis of the influence that certain parameters (such as longitudinal slip, camber angles, and toe angles) have directly on the tire model. By analyzing the variation in cornering stiffness caused by these parameters, it will be possible to estimate their influence on the stability region of a vehicle exhibiting oversteer, like the one under analysis, but also on the potential to trigger oversteering phenomena and, thus, instability, even in vehicles that are typically stable, such as understeering vehicles.

### 2.8.2. Longitudinal Slip

By repeating the procedure described in 0 for different values of longitudinal slip, it is possible to estimate the effect that this parameter has on the axle characteristics and, consequently, on the lateral dynamic capability of the vehicle under examination.

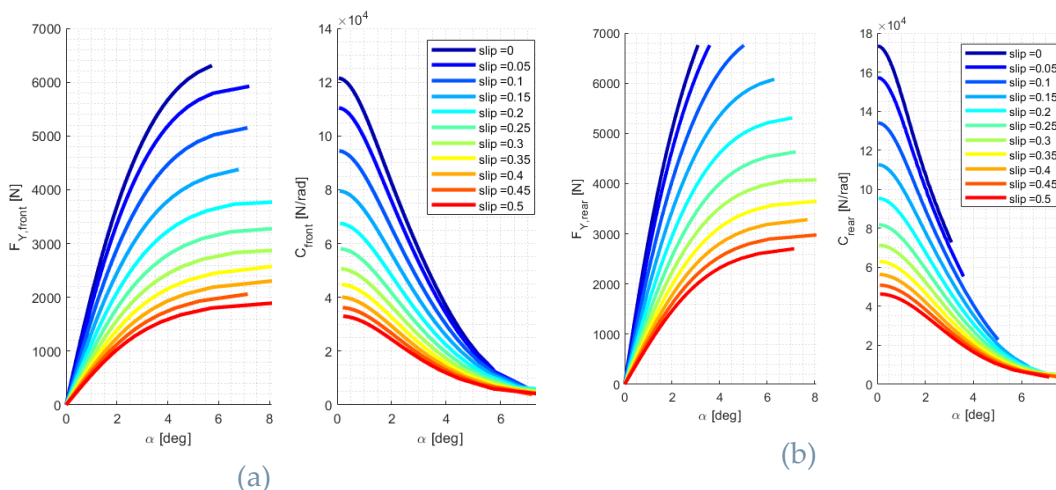


Figure 2.53 : (a) Front (b) Rear Cornering Stiffness affected by longitudinal slip

### 2.8.3. Toe Angle

In a manner similar to what was done for longitudinal slip, the results of the influence of the toe angle on the characteristics (front and rear) of the axles are presented.

To clarify the sign convention used for the toe angle, reference is made to the following image, [11].

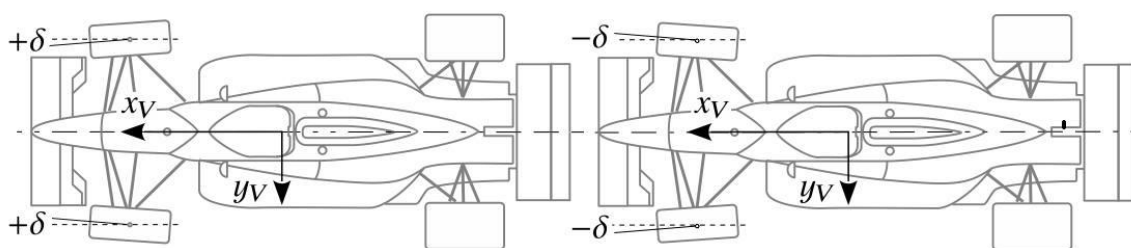


Figure 2.54 : Sign convention for toe angle. Left: Toe-in, right: Toe-out

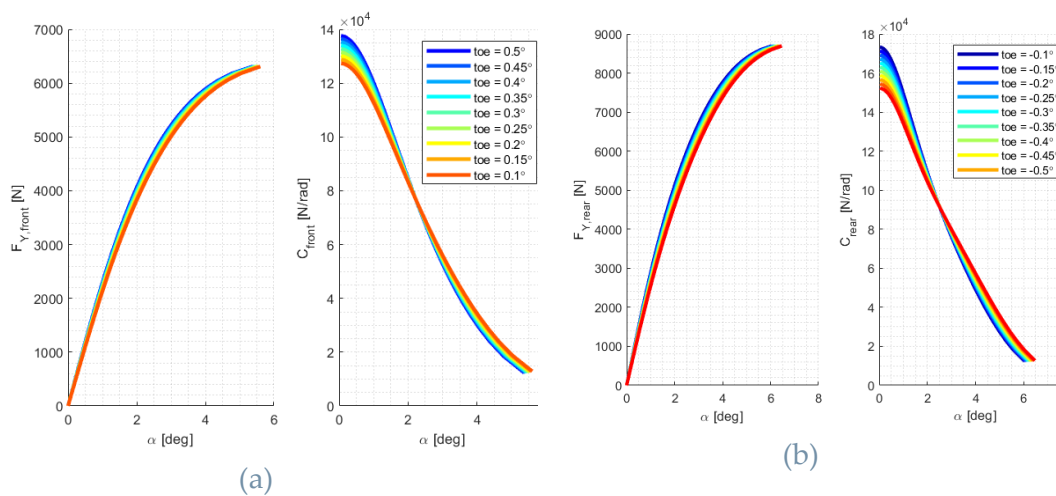


Figure 2.55 : (a) Front (b) Rear Cornering Stiffness affected by toe angle

### 2.8.4. Camber Angle

The following shows the influence of the camber angle on cornering stiffness. To clarify the sign convention used for the camber angle, reference is made to the following image, [11].

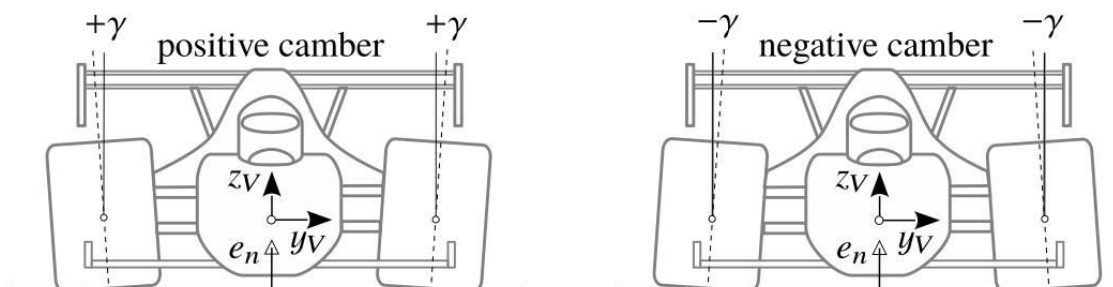


Figure 2.56 : Sign convention for camber angle

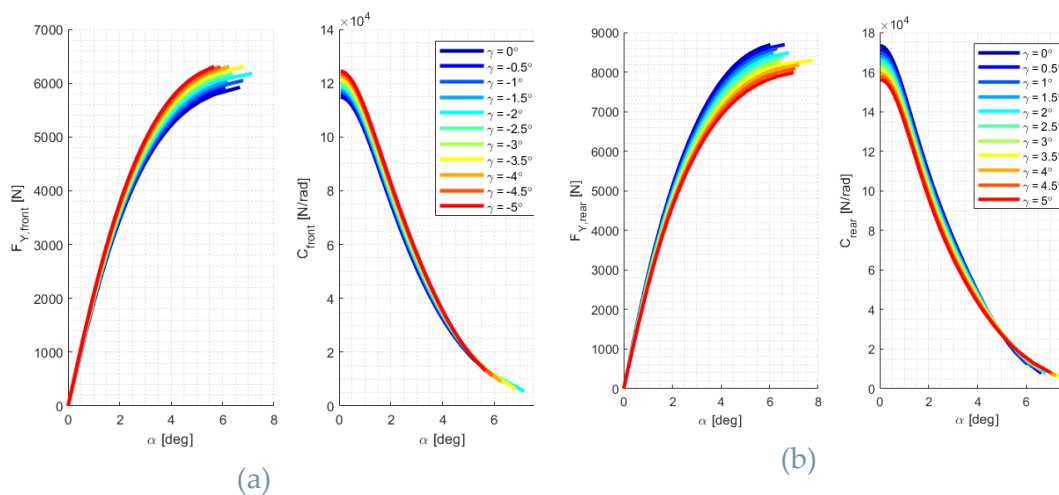


Figure 2.57 : (a) Front (b) Rear Cornering Stiffness affected by camber angle

## 2.9. Yaw Moment Control

### 2.9.1. Objective

The objective of this section is to revisit the work presented in a 1993 paper by Y. Shibahata [12] which introduces the development of a method called the ' $\beta$ -method.' This method aims to determine the potentially available yaw moment as a function of the vehicle's operating conditions. There are several techniques that can be employed to control the vehicle's yaw moment, which vary depending on the type of vehicle considered. For example, torque vectoring techniques are widely used, particularly in vehicles equipped with one or more electric powertrains [13], or active control systems such as the Electronic Stability Program (ESP).

However, in this section, we will focus on control actions for the yaw moment using only the steering angle, either by the driver or by a control system capable of directly influencing the steering.

First, a simplified vehicle model, the bicycle model, will be presented to obtain the desired maps. After discussing this, further contributions will be introduced using a double-track model, equipped with four tires, which takes into account the contribution of the track width, traction forces, and self-aligning torques to estimate the potentially available yaw moment.

Additionally, with the aim of generalizing these maps, which in the reference paper are described on the  $(M_z, \beta)$  plane, a solution will be presented to express the potentially available yaw moment as a function of lateral acceleration, parameter that provides a more descriptive representation of the vehicle's operating conditions than the sole steering angle.

### 2.9.2. Method

With reference to [12] to obtain the maps on the  $[(M)_z, \beta]$  plane, it is necessary to be able, for a given steering angle, to evaluate the yaw moment based on the forces exerted by the tires as the vehicle's operating conditions change, particularly as the sideslip angle  $\beta$  changes. In order to assess the magnitude of the lateral forces that can be exerted by the tire, we decided to use the axle characteristics previously derived through the method described in section 2.8. However, to use these characteristics, it is necessary to know the values of the tire slip angles under the given conditions of speed, sideslip angle, and yaw rate. For this purpose, the following methodology was employed: Starting from the various conditions of  $u$ ,  $v$ , and  $\psi$  of the vehicle,

the values of  $u_i$  and  $v_i$  for the  $i$ -th wheel are evaluated in order to determine the slip angle of each wheel.

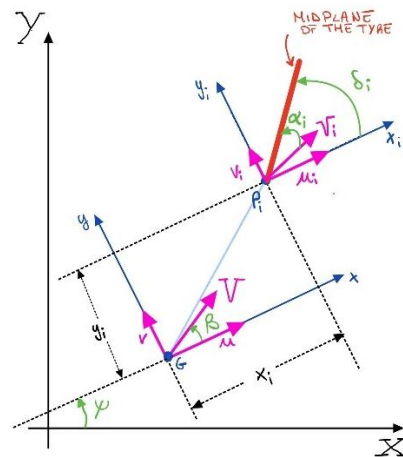


Figure 2.58 : Global Reference frame (X,Y), Vehicle reference frame (x,y) and Tyre reference frame ( $x_i, y_i$ )

$$\overline{V_G} = \overline{V_i} + \dot{\psi} \wedge (\overline{P_i - G})$$

Term  $\dot{\psi} \wedge (\overline{P_i - G})$  can be expressed as

$$\begin{vmatrix} \mathbf{i} & \mathbf{j} & \mathbf{k} \\ 0 & 0 & \dot{\psi} \\ x_i & y_i & 0 \end{vmatrix} = -\dot{\psi} y_i \cdot \mathbf{i} + \dot{\psi} x_i \cdot \mathbf{j} + 0$$

$$\overline{V_i} = \begin{pmatrix} u_i \\ v_i \end{pmatrix} = \begin{pmatrix} u \\ v \end{pmatrix} + \begin{pmatrix} -\dot{\psi} y_i \\ \dot{\psi} x_i \end{pmatrix}$$

and finally the  $i$ -th wheel's side slip angle can be expressed as

$$\alpha_i = \arctan\left(\frac{v + \dot{\psi} x_i}{u - \dot{\psi} y_i}\right) - \delta_i$$

Further considerations should be made on the term  $\delta_i$  that in a vehicle with toe angles other than zero does not exactly represent the steering angle value to the wheels, as

$$\delta_i = \delta_w \pm \delta_0$$



previously analyzed, was taken as reference (2.3), driven at the speed of  $70 \frac{km}{h}$ , As shown in the graph below.

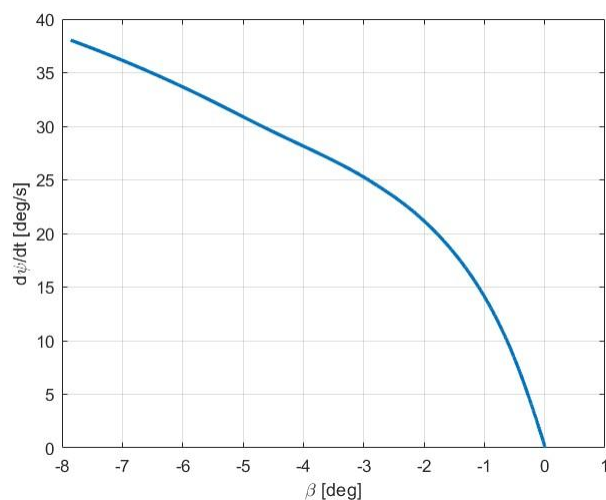


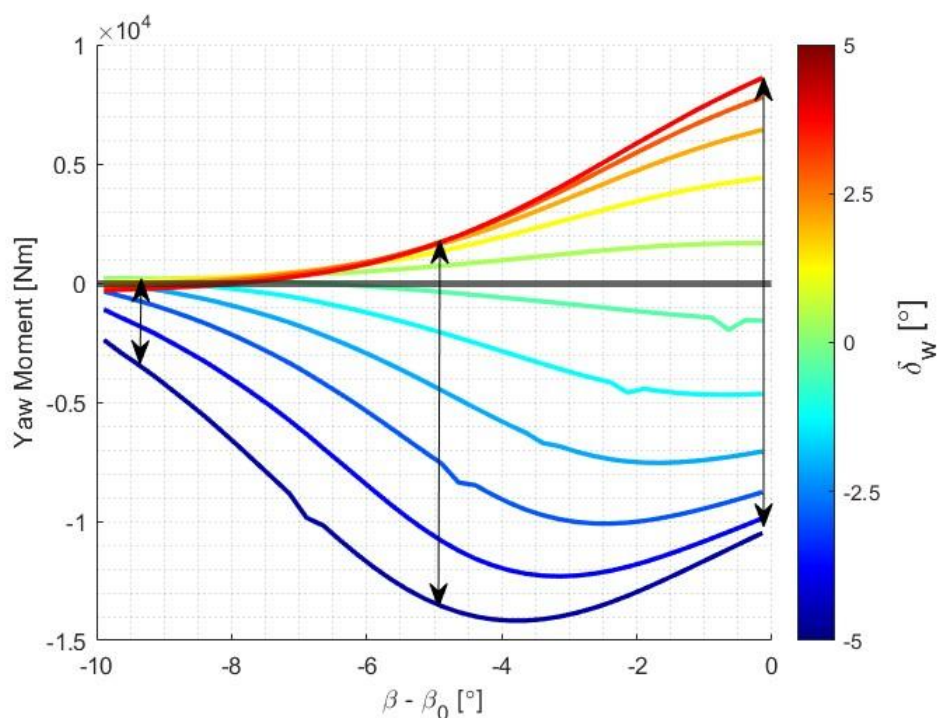
Figure 2.60:  $(\beta, \dot{\psi})$

Thus, setting successive values of the flying angle to the wheels and imposing on the vehicle these conditions of states  $(\beta, \dot{\psi})$ , the lateral forces expressed at the front and rear axles respectively are derived.

In this first analysis the yaw moment potentially expressible from each of these state conditions is derived from the following equation of equilibrium at rotation:

$$M_z = F_{y,front} \cdot a - F_{y,rear} \cdot b$$

The following is a graph showing the results obtained for steering angle values at wheels between  $[-5^\circ, 5^\circ]$ , alternately steering angles between  $[-65^\circ, 65^\circ]$ .

Figure 2.61:  $M_z - (\beta - \beta_0)$ 

The area between the maximum and minimum curve  $M_z$  defines the zone within which it is still possible to correct the vehicle's trajectory by using the steering angle. The double arrows in the graph are intended to show how this area is progressively reduced as it increases in the form of the term  $(\beta - \beta_0)$ . The asymmetry of this graph can be justified by the fact that part of the adhesion useful to generate positive moments is already used precisely to bring the vehicle in those dates' conditions  $(\beta, \dot{\psi})$ , while for opposite flying angles that generate negative moments you still have full availability of the adhesion.

It is also important to point out that for negative steering angles, there is no "bundling" of the curves when varying from  $\beta$ , what instead happens for positive flying angles from the direction of those necessary to bring the vehicle in those given states. The above appearance suggests that the maximum steering excursion is a very important aspect when trying to stabilize the vehicle motion through the action of the steering alone: For example, the cars that compete in the drift championships are specially fitted with suspensions that have, among other things, the objective of maximizing the range of the steering wheels, just for the reasons just described. In the same way, however, an increase in steering possibilities does not directly result in an increase in the moment of yaw in the case of a positive flying angle, as is evident from the graph above, beyond a certain value of  $(\beta - \beta_0)$  the increase in flying

angle even has the effect of reducing the maximum value of  $M_z$  due to the fact that large values of drift angles are being applied to the front axle and thus result in its saturation.

Term  $(\beta - \beta_0)$  has a direct correspondence with the lateral acceleration, it is therefore possible to express the embarrassing moment also in relation to the lateral acceleration. The graph below shows this.

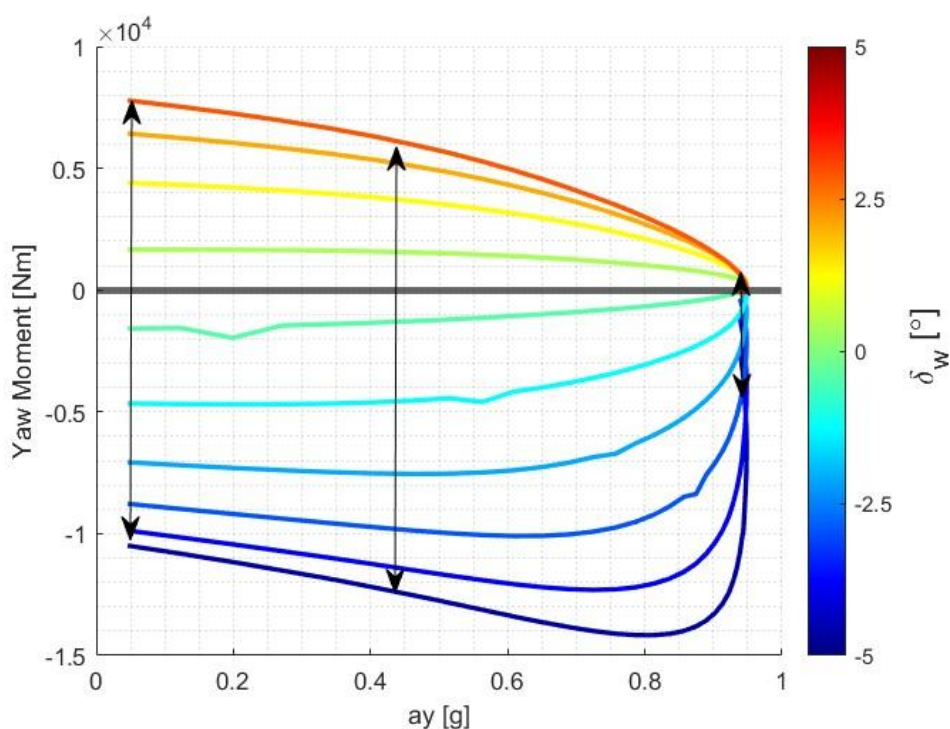


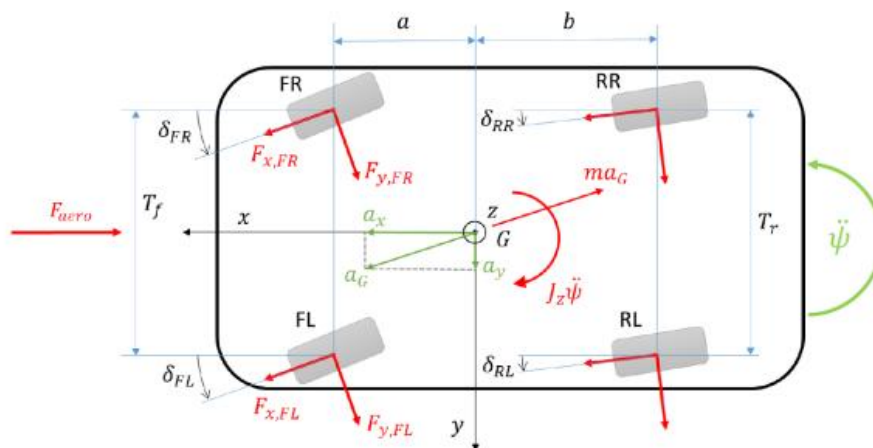
Figure 2.62:  $M_z - a_y$

Again, as was to be expected, there is a reduction in the area between the maximum and minimum  $M_z$  curves with increasing lateral acceleration. In particular, one can notice the aggressive reduction that results from being near the lateral acceleration limit: what we defined as an area degenerates at a point in correspondence with the maximum value of lateral acceleration, which is a symptom of the fact that in this condition no action applied to the flying angle is more able to stabilize the vehicle.

As we have already said in the introduction of this paragraph, our intention is to show the results of the same analysis, conducted this time taking into account a more complete vehicle model: dual track model. In particular, the

use of a four-wheel model can eliminate the previously introduced parallel-wheel steering hypothesis which is much more representative of real road vehicle steering systems. The contributions of longitudinal forces and self-aligning moments of tires are also considered in this analysis.

Below is a graph useful to understand the model used and its equation of balance at rotation.



$$M_z = \sum_{i=1}^4 F_{x_i} \cos \delta_{w_i} y_i + \sum_{i=1}^4 F_{x_i} \sin \delta_{w_i} x_i + \sum_{i=1}^4 F_{y_i} \cos \delta_{w_i} x_i + \sum_{i=1}^4 F_{y_i} \sin \delta_{w_i} y_i + \sum_{i=1}^4 M_{Z_i}$$

The results obtained are quite comparable to those obtained with the single-track model and with the characteristic curves of the axles which consider the load transfer. The smallest differences can be attributed to the contribution of longitudinal forces and self-alignment moments. In particular, the presence of these contributions results in a slight reduction of the area between the two curves. The vehicle being considered, as described in previous chapters, has an open differential and due to load transfer the curved inner wheel undergoes a significant decrease of vertical load in favor of the outer wheel, this phenomenon means that the longitudinal forces on the outer wheel are modularly greater than those generated by the inner wheel. Due to this difference, a moment is generated around the x-axis that has positive direction: therefore, for positive flying angles we see, compared to the single-track model, an increase in the available moment precisely due to the contribution just described. Conversely, for negative side slip angles, the contribution described above results in a reduction of the available moment.

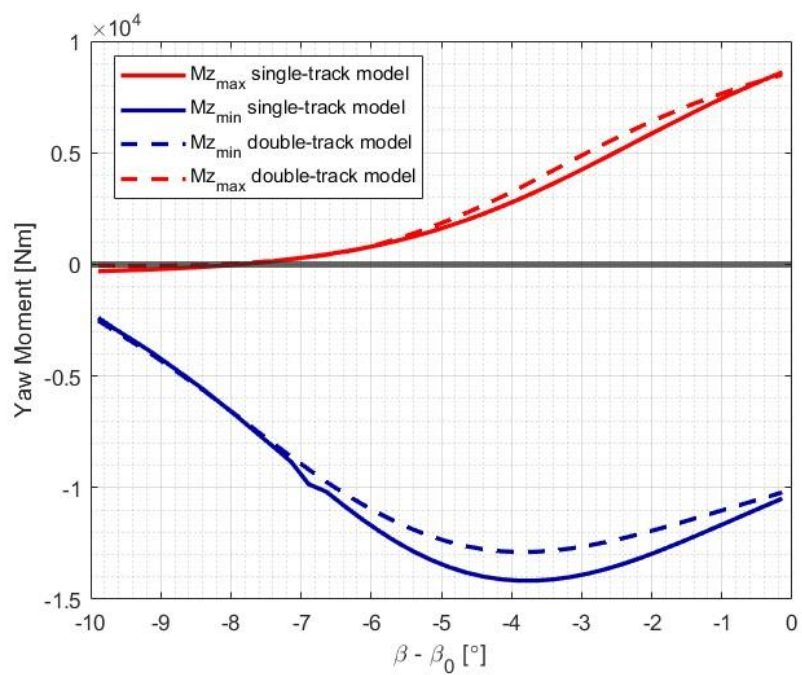


Figure 2.63: Results Comparison between single-track and dual-track

### 3 Phase Plane

With reference to the work presented in 1.1.2, the methodology described in 1.2.2 allows for the validation of the critical speed graph as a function of lateral acceleration, which is shown below.

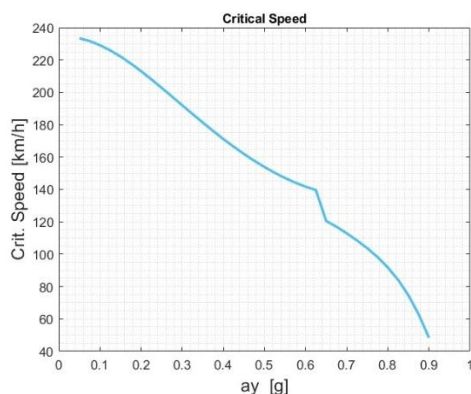


Figure 3.1: Critical speed affected by lateral acceleration

Each point on this curve is expected to represent an unstable equilibrium point, meaning that a small perturbation from the equilibrium condition would lead to the divergence of the system states. For example, at  $V = 89 \frac{km}{h}$  and  $\delta_{sw} = 16^\circ$ , the system is in a condition of  $a_y = 0.8g$ . For this lateral acceleration value, the chosen speed corresponds exactly to the identified critical speed under this specific acceleration condition. The resulting phase plane is shown in Figure 3.2: in particular, the equilibrium condition reached corresponds to the steady-state condition of the states identified in 2.4. Additionally, a comparison is made with a scenario where the steering angle is slightly increased to  $\delta_{sw} = 18^\circ$ , which, at the same speed, results in a higher lateral acceleration. Under these conditions, it is no longer possible to identify any equilibrium points within the phase diagram. The red point in the left figure in Figure 3.2 represents the unstable equilibrium point. In contrast, the right figure confirms the absence of any equilibrium points, for the negative value of side slip angle, with all initial conditions leading to diverging trajectories in the phase plane.

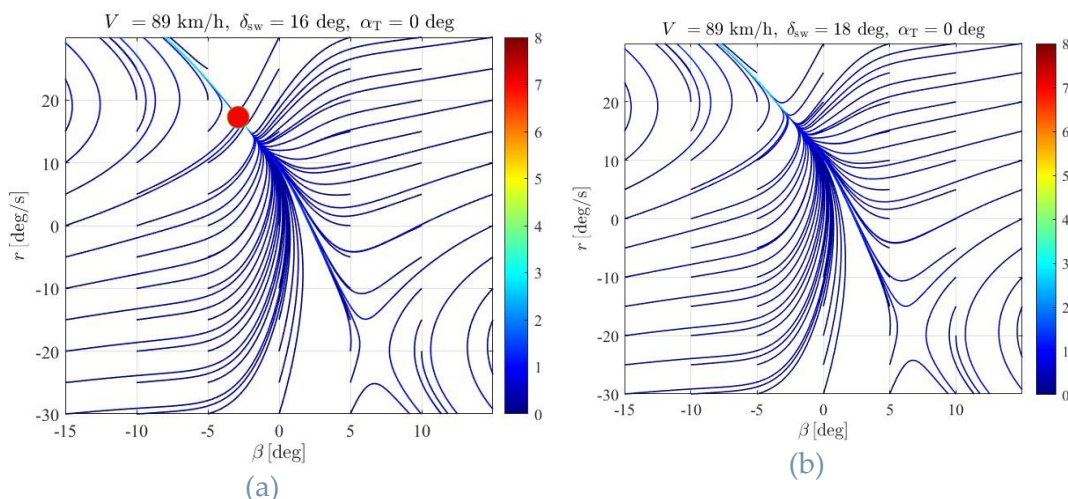


Figure 3.2 : Phase Portrait at  $V=89$  km/h for two value of steering angle

The same considerations can be made by selecting another point on the curve in Figure 3.1: Critical speed affected by lateral acceleration. For example, choosing a speed of  $V = 155 \frac{km}{h}$  and a steering angle of  $\delta_{sw} = 2.7^\circ$ , we find ourselves in a condition of  $a_y = 0.5g$ . For this lateral acceleration value, the selected speed corresponds exactly to the identified critical speed under that specific acceleration condition. Therefore, as in the previous case, we expect the presence of a single unstable equilibrium point for this condition.

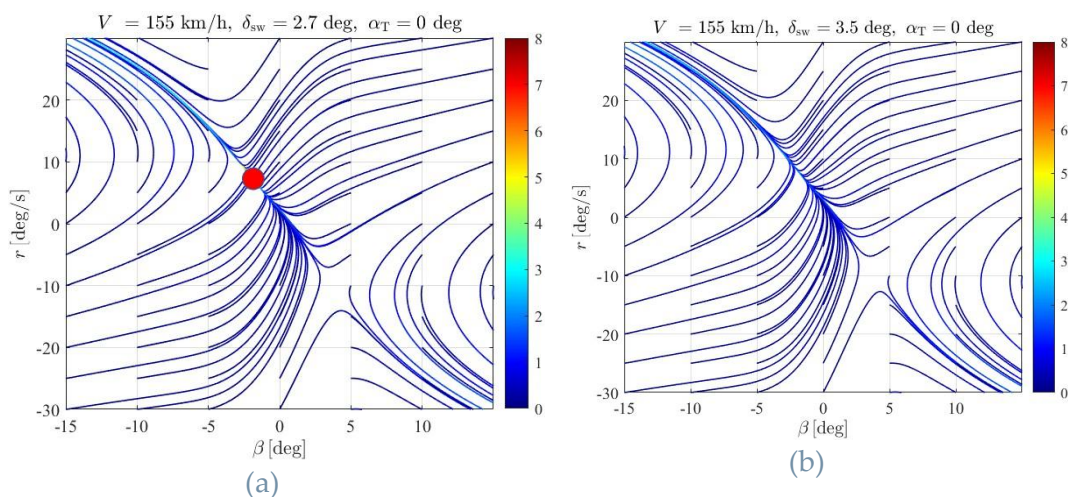


Figure 3.3 : Phase Portrait at  $V = 155 \frac{km}{h}$  for two value of steering angle

### 3.1.1. Bifurcation

The aim of the following discussion is to demonstrate how some of the parameters analysed in Chapter 2 affect the stability region of the phase plane previously described. The generation of these stability maps, varying with the vehicle's operating conditions, will then be introduced in the following chapter within a vehicle model equipped with a predictive controller. The controller's objective must be to account, among other things, for the vehicle's stability limits as the operating conditions change.

#### 3.1.1.1. Effect of steering angle

With reference to what has been described so far, it is possible to analyse the behaviour of the system's equilibrium points at a given speed as the steering angle varies. Specifically, under the described conditions, we expect to find the two unstable equilibrium points of the system: one is at a steering angle of approximately  $\delta_{sw} = 16^\circ$ .

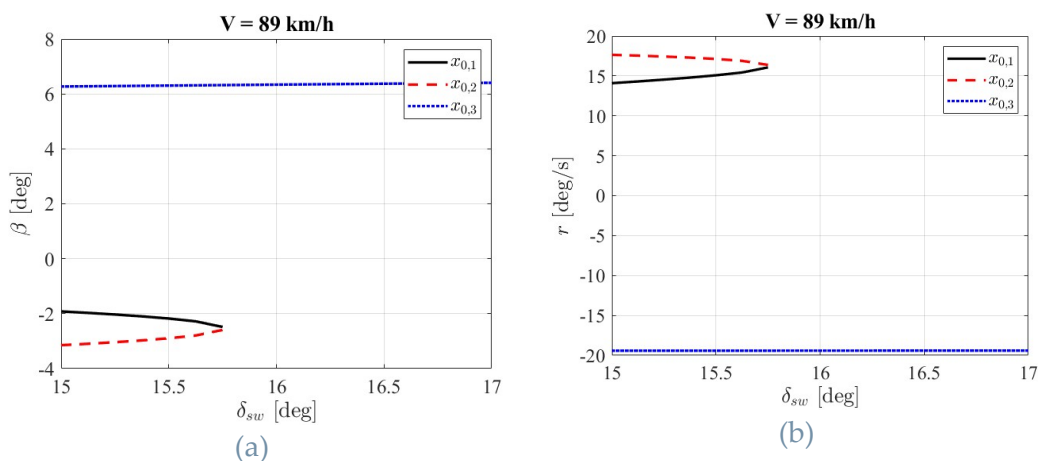


Figure 3.4 :bifurcation analysis stable fixed point (black solid line) unstable fixed point (red and blue dashed line)

The above can be displayed in a three-dimensional graph, by combining the results of the bifurcation tool with the phase plane.

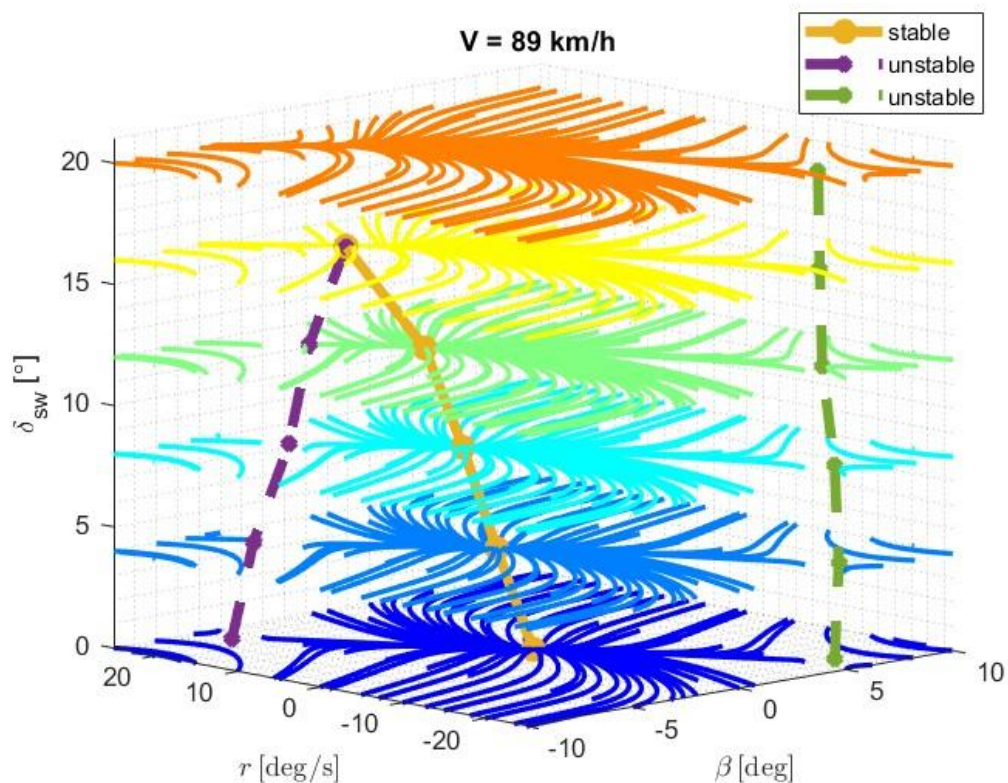


Figure 3.5 : Steering Angle bifurcation analysis

The trend of the equilibrium points on the plane of the phases when the steering wheel angle varies can be more clearly visualized in Figure 3.6 : Equilibrium points affected by steering angle. It is intended to point out that within the treatment the points of stable equilibrium will be indicated with circles, while the points of unstable equilibrium by means of rhombuses and stars.

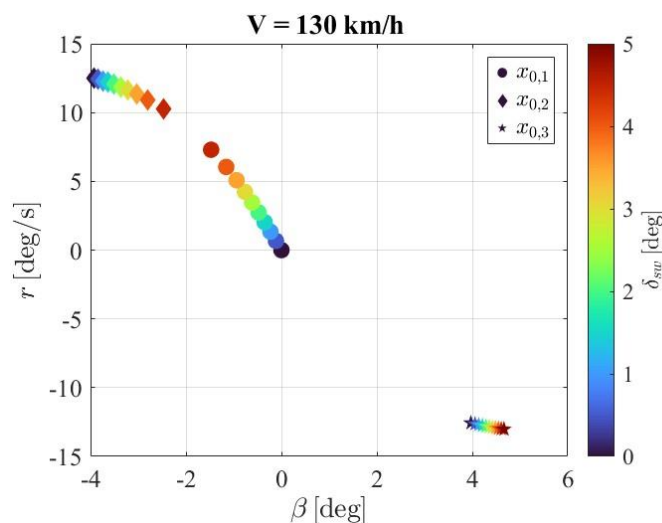


Figure 3.6 : Equilibrium points affected by steering angle

### 3.1.1.2. Effect of longitudinal road inclination

In order to show the effect of the longitudinal inclination of the road on the balance points, the trend of these on the plane of the phases

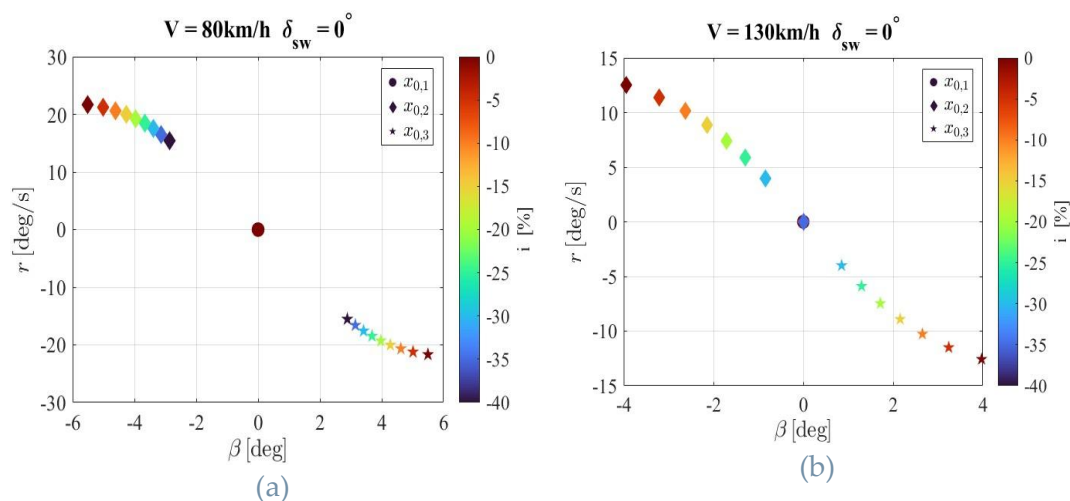


Figure 3.7 : Equilibrium Point affected by road inclination

It is clear that the trend of these points also depends on other parameters such as vehicle longitudinal speed and steering angle: looking at figure 3.7 we see how the increase (in absolute value) of the value  $i$  indicating the percentage of longitudinal road inclination for figure (a) does not lead to a coincidence between stable equilibrium point (circle) and unstable equilibrium points (diamond, star), that is to say for that given value of longitudinal speed it is still possible to define an area of stability even if reduced due to the inclination of the road. In contrast, for the case (b) where the vehicle speed is higher there is an overlap for a value of  $i = 35\%$ , that is, in correspondence to this value it is no longer possible to define a stability area since the point identified is a single unstable equilibrium point and even small disturbances around this point can lead to the divergence of states and therefore to phenomena of instability. The objective of the controller will therefore be in the following chapters to be able to detect the reduction of the stability zone and then make invalid trajectories that may lead to instability phenomena, before they can occur. The above-mentioned points out the importance of defining such maps as multidimensional maps which take account of the mutual presence of certain operating conditions.

### 3.1.1.3. Effect of longitudinal acceleration

It is important to clarify that this analysis was conducted by implementing the longitudinal acceleration contribution, as done in Chapter 2, solely as a contribution to longitudinal load transfer. However, in a future analysis, it would be advisable to also consider the causes generating longitudinal acceleration, such as traction and braking forces on the vehicle. This would allow accounting for the effect these forces have on the tires' ability to generate lateral forces.

Nonetheless, this analysis highlights the significant impact that longitudinal load transfers have on the stability region.

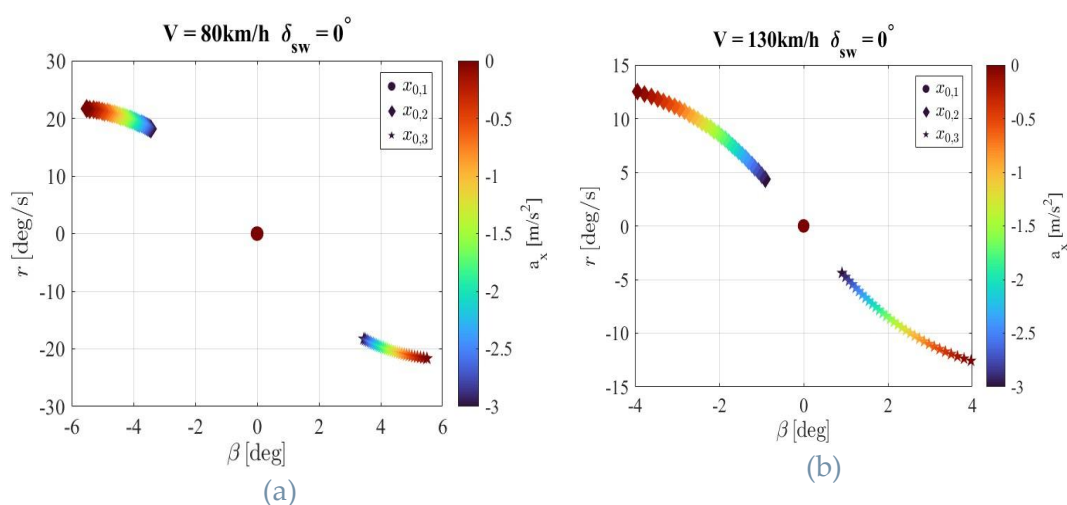


Figure 3.8 : Equilibrium points affected by longitudinal acceleration

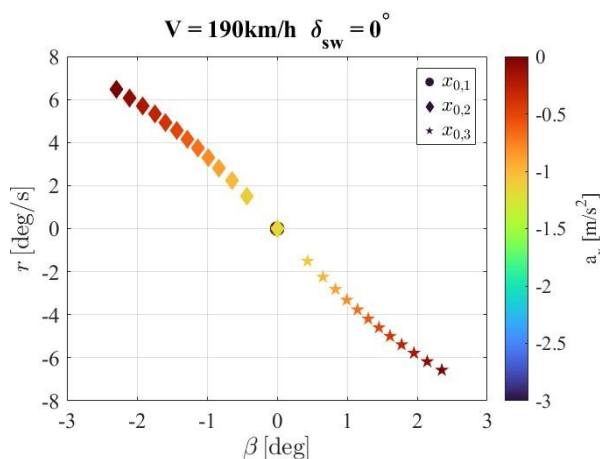


Figure 3.9 : Equilibrium points affected by longitudinal acceleration

3.1.1.4. Effect of adherence coefficient

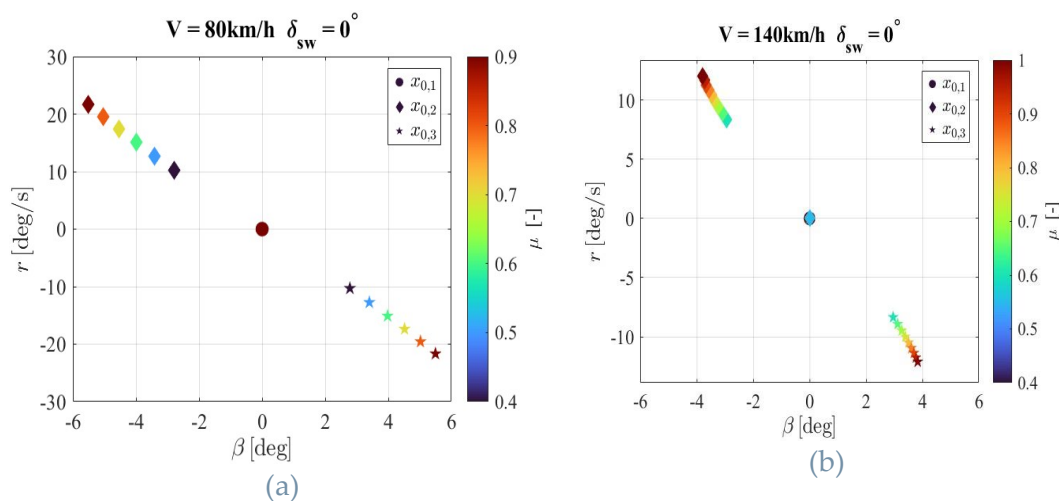


Figure 3.10: Equilibrium Point affected by adherence coefficient

Unlike the cases analyzed so far, studying the effect of the coefficient of adhesion we note from FIG (b) that there is no progressive reduction in the stability zone: in particular by changing from a value of ... at a value of ... the distance between stable and unstable equilibrium points is drastically reduced to zero, leading to the coincidence of stable and unstable equilibrium points, thus defining a single unstable equilibrium point. We can see what is described above also in the figure below which shows the bifurcation analysis conducted to vary the coefficient of adhesion for the two variables of system state.

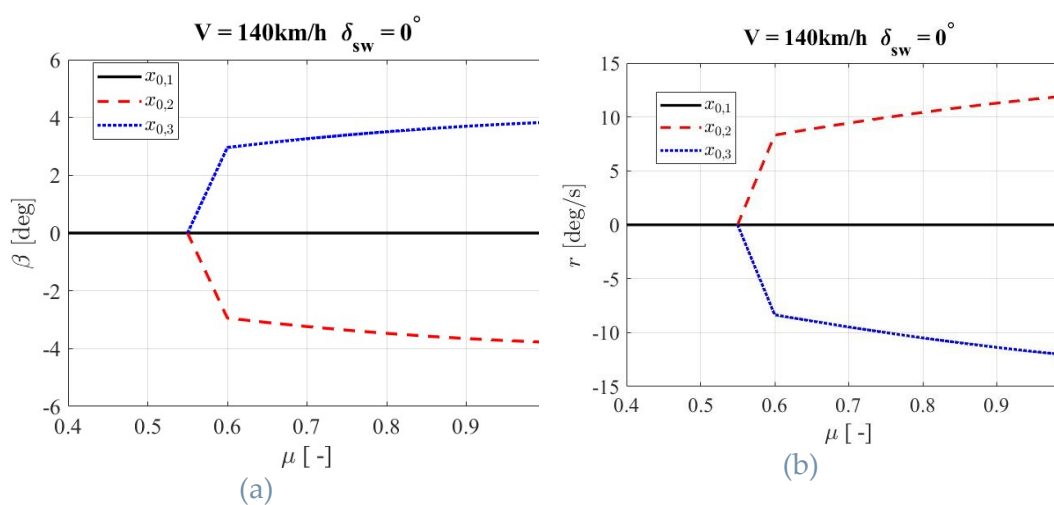


Figure 3.11 : Adhesion coefficient Bifurcation Analysis

However, what has been described above does not hold true when analyzed through the phase plane generation tool. This leads to the conclusion that, currently, the bifurcation analysis tool still has some limitations in correctly identifying the system's equilibrium points. For future development, it would be advisable to analyze the neighborhood of the unstable equilibrium points with a finer discretization, possibly starting from the trajectory generation tool in the phase plane.

### 3.2. Open-Loop Stability region definition

After obtaining a sufficient number of phase maps and diagrams, a method is required to define the stability zone in which the vehicle can operate under varying operating conditions. In reference to the work carried out on the autonomous driving model preceding this thesis ( ) the stability zone was defined as follows.

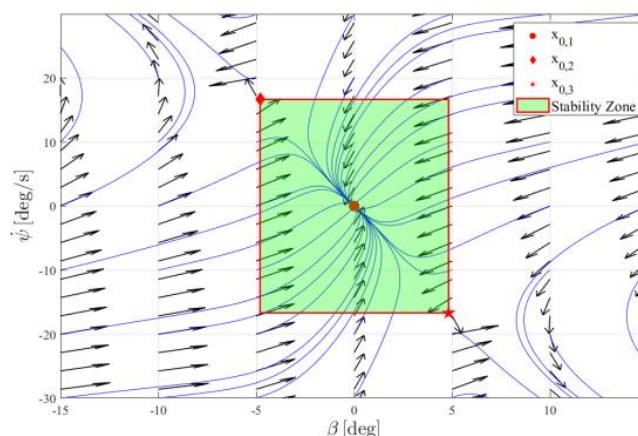


Figure 3.12 : Example of Stability area previously considered

With reference to Figure 3.11, the area of a rectangle whose vertices were the two points of unstable equilibrium of the vehicle was defined as the stability zone of the vehicle. This method, while working, considered the trajectories of states (when initial conditions vary) that are in fact stable. In addition, within the controller model the verification of feasibility of the trajectory in terms of stability was implemented by simply verifying that states were greater than a maximum value and less than a minimum value (values defined by the sides of the green rectangle in the figure)

With the objective of extending the stability zone considered valid in this work, a new method for defining the defined stable area was developed, presented below.

Starting from the bifurcation analysis conducted on the various parameters, the defined points of unstable equilibrium are taken as reference for the definition of the stability zone. The distance between these two points is taken as a reference to define the short diagonal of a rhomboidal figure. Choosing the short diagonal and setting the parameters for defining the rhomboidal figure, such as, length of the larger diagonal by a gain added to the short diagonal previously defined, and angle between the two diagonals identified,

it is possible to define a diamond shape in which the states are defined as stable. The above is easier to understand by looking at the figure below.

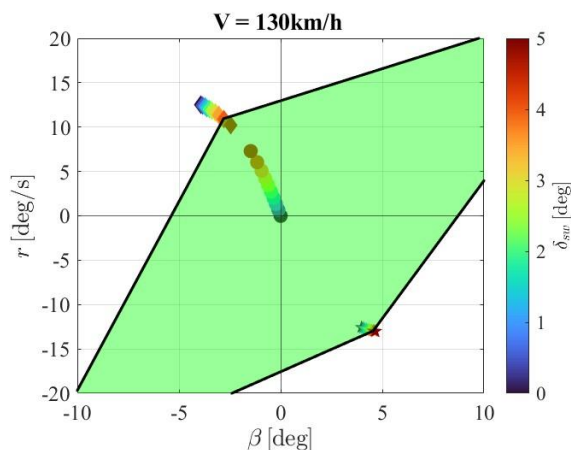


Figure 3.13 : Example of stability area definition

Take as reference, by way of example, the bifurcation analysis conducted on the flying angle at speed  $V = 130 \frac{km}{h}$ . Selecting, for example, the unstable balance points for a flying angle  $\delta_{sw} = 4^\circ$  the region marked in green in FIG is defined as stable.

To ensure that this region comprises only and exclusively stable points, it is possible to display the identified area directly in the phase plan which also shows the vector field. In FIG, the red dotted square represents what was defined in the previous work as a stable zone, In green the region of stability estimated by the new method is highlighted and in red the remaining part of the phase diagram which is called unstable.

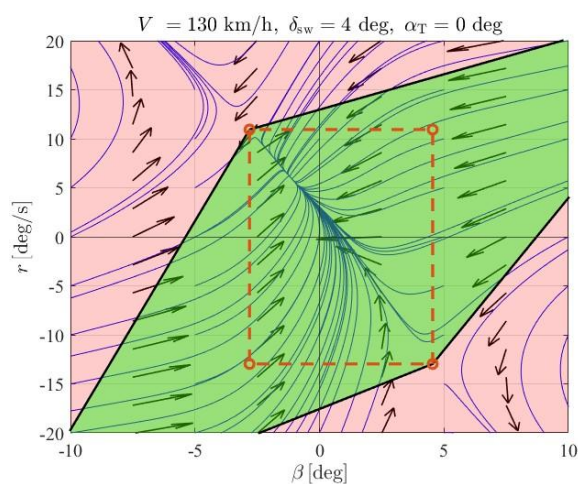


Figure 3.14 : Example of stability area over vector field

In this way we see how now we have as reference a zone of stability much larger than the only area of the square dotted in red. This allows us to work under conditions which are in fact stable, and which were previously discarded.

### 3.3. Closed-Loop Stability region definition

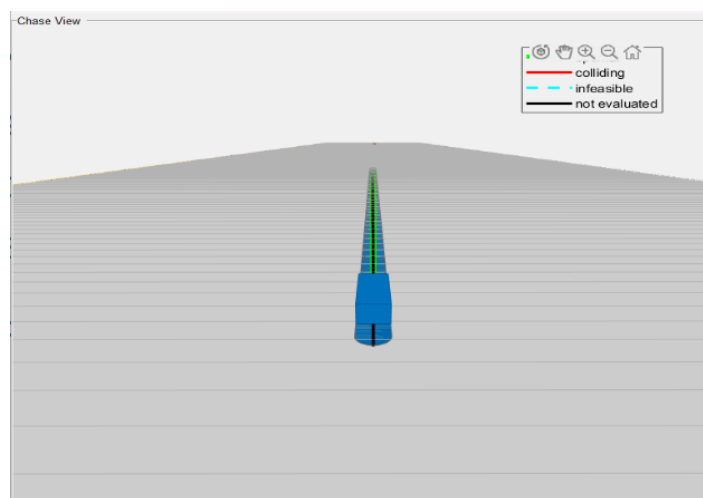
#### 3.3.1. Method

The objective is to define a stability region for the vehicle system equipped with a model-based predictive controller. Building on previous work [9], the stability of the system, including both the vehicle and the driver (or controller), is analyzed through the application of an impulse-type disturbance. This type of disturbance provides the system with an initial state velocity, allowing different initial state conditions to be imposed by varying the disturbance magnitude.

By letting the simulation evolve, it is then possible to evaluate which initial state conditions lead to stability or instability. This distinction will certainly depend on the vehicle conditions but, more importantly, on the controller design and specific parameters such as the actuation delay of the commands, and under- or over-steering nature of the vehicle.

#### 3.3.2. Simulation Scenario

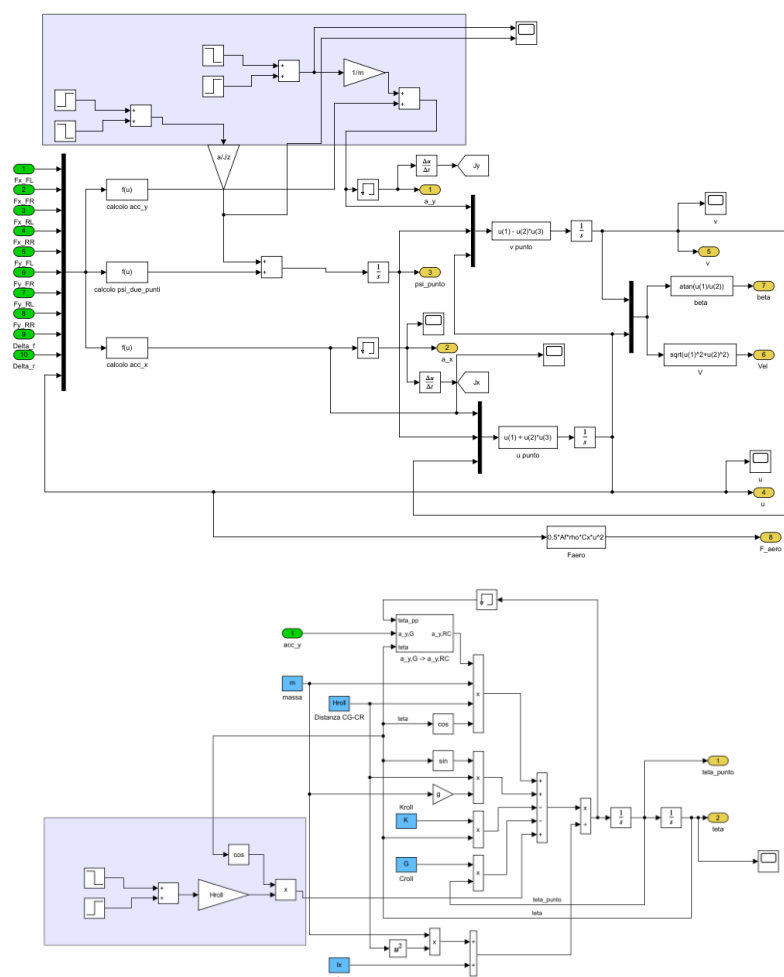
The implemented simulation scenario consists of a straight trajectory (thus, a straight reference trajectory for the controller) traveled at a constant speed of  $V = 120 \frac{km}{h}$ . The lane boundaries have been set wide enough to allow the vehicle's trajectory to evolve without considering real roadway constraints. This is because the objective of this study is not to analyze conditions leading to the vehicle running off the road, but rather to ensure sufficient space for performing the maneuver.



### 3.3.3. Disturbance Implementation

A lateral force disturbance and a yaw moment disturbance were applied to the vehicle at a given instant  $t=1s$  with a duration of  $\Delta t=0.2s$  during the maneuver. This disturbance was implemented by introducing an external lateral force contribution into the equation that calculates the vehicle's lateral acceleration. The force magnitude progressively increased to start from gradually larger initial state conditions, allowing for an analysis of its effects on the vehicle-controller system. A similar approach was used to introduce the yaw moment disturbance.

Below, the details of the implemented Simulink block are presented, where the blue area represents the added external force contribution.

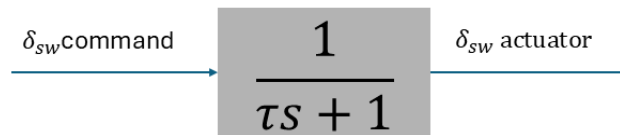




$$\ddot{\theta} = \frac{1}{(I_{x_g} + mh_{rc}^2)} [ma_y h_{rc} \cos\theta + mgh_{rc} \sin\theta - K_{roll}\theta - C_{roll}\dot{\theta} + F_{y_{dist}} h_{rc} \cos\theta]$$

### 3.4. Steering Dynamics

In order to also study the effect of the controller-actuator system parameters on the stability region, a first order transfer function was introduced to represent a delay in the actuation of the steering wheel angle. This angle is computed by the controller based on errors relative to the reference trajectory.



Two delay values,  $\tau$ , were chosen to be displayed, specifically referred to as:

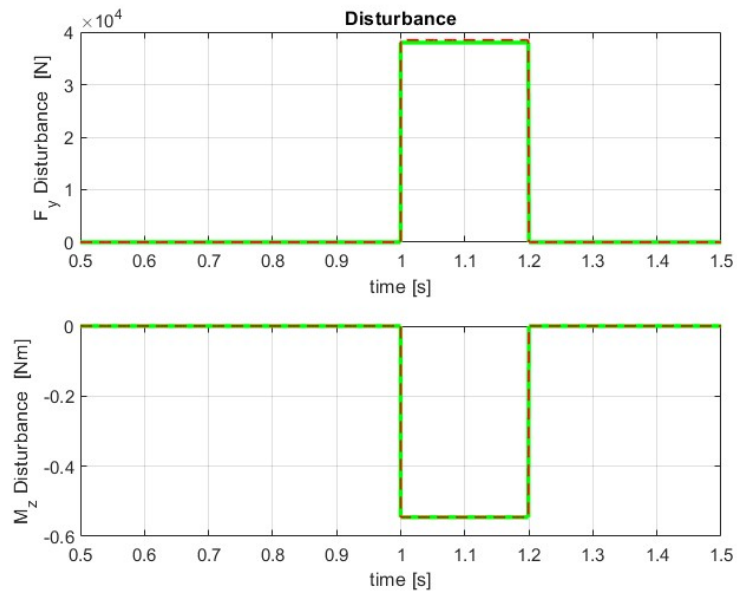
Table 5 . Steering actuation delay

	$\tau$	unit
<i>Fast Steering</i>	0.2	[s]
<i>Slow Steering</i>	0.4	[s]

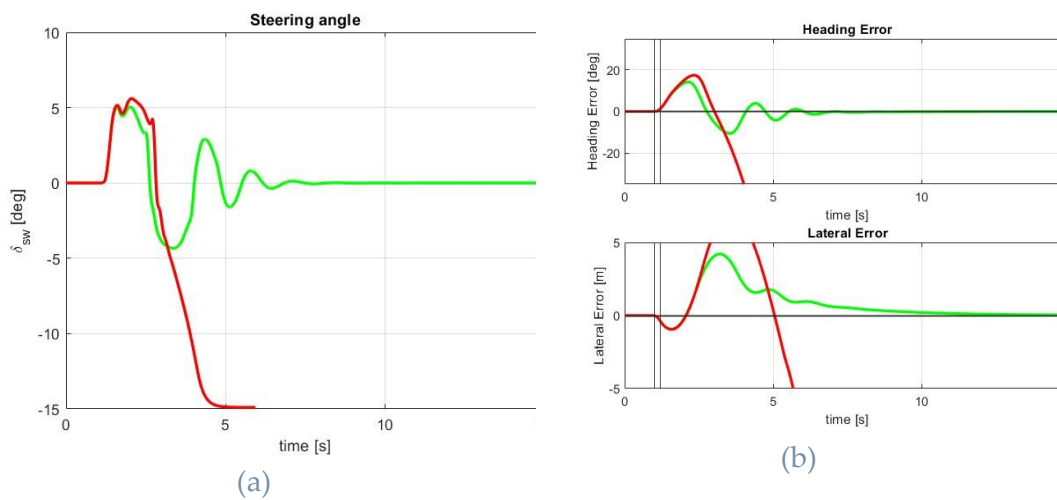
## 3.5. Results: OverSteering Vehicle

### 3.5.1. "Fast steering" Results

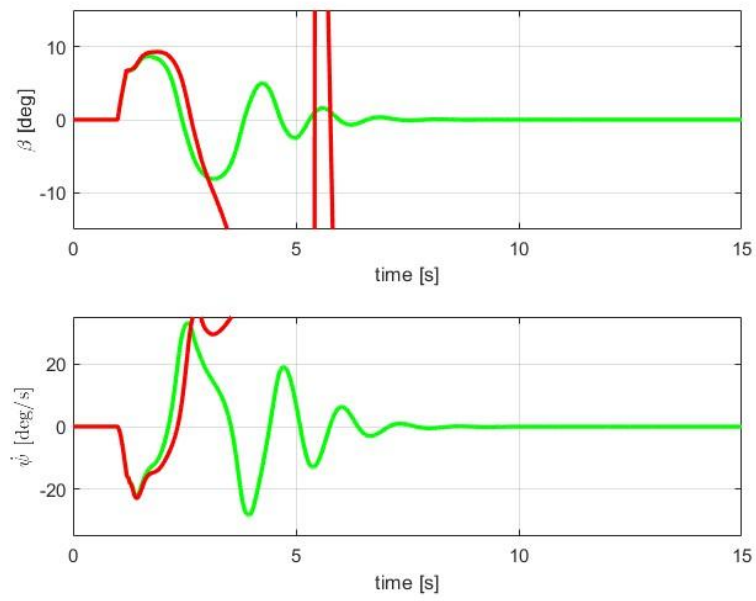
Input: Disturbance



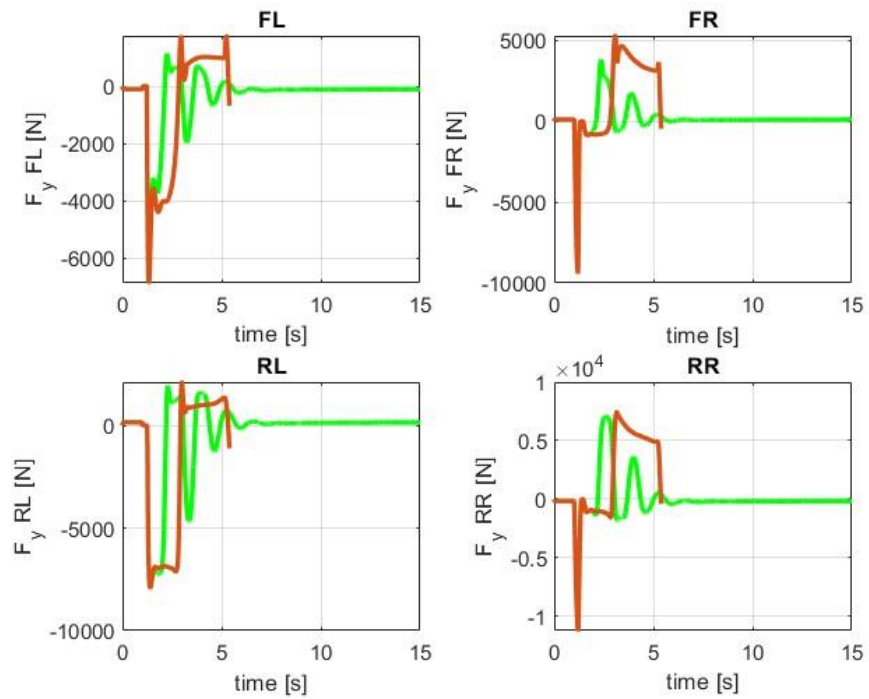
Steering Angle and Errors



## State



## Lateral Force



## Phase Plane

By performing a series of simulations, like those whose results are shown in the previous graphs, it is possible to represent the closed-loop stability region of the vehicle in the phase plane.

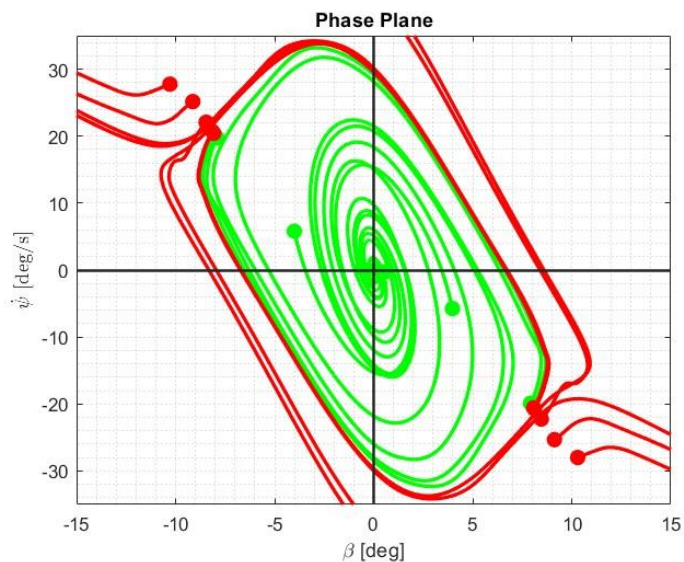
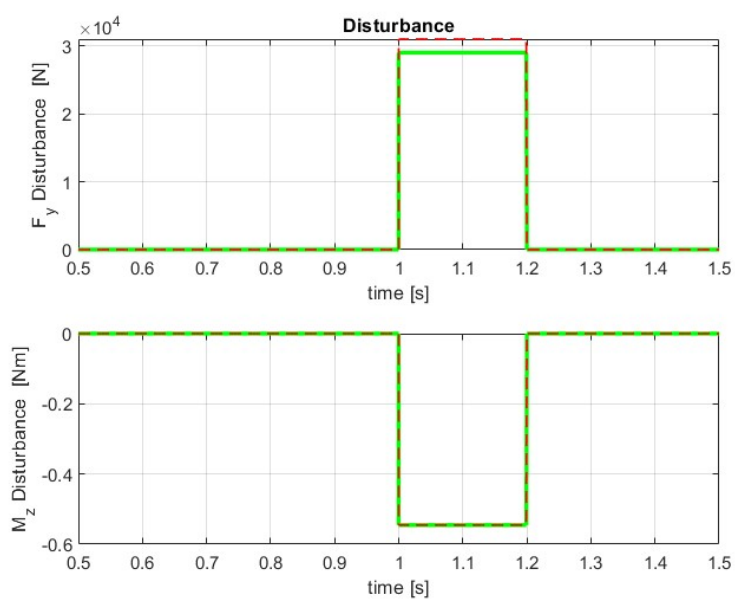


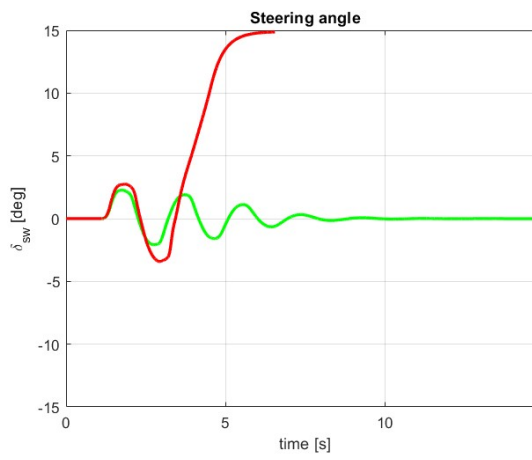
Figure 3.15: Closed loop phase plane

## 3.5.2. "Slow Steering" Results

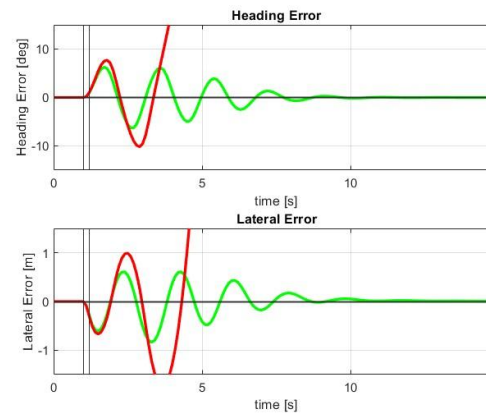
Input: Disturbance



## Steering Angle and Errors

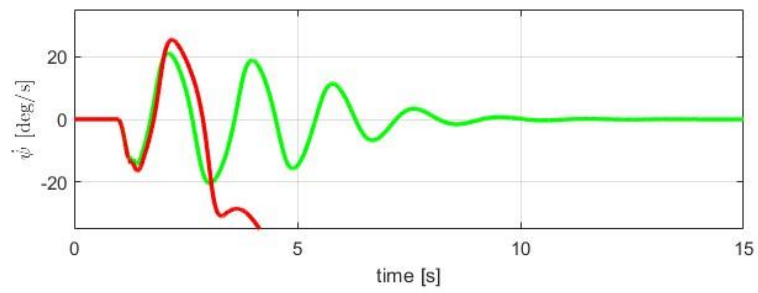
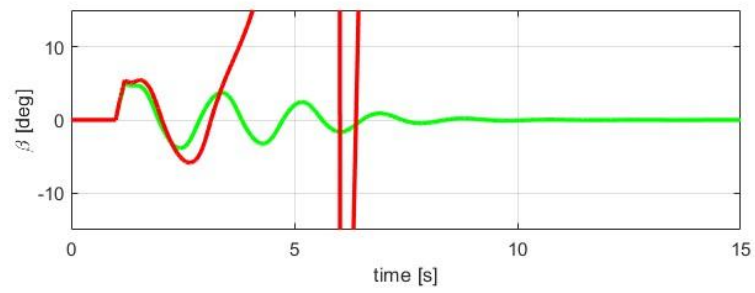


(a)

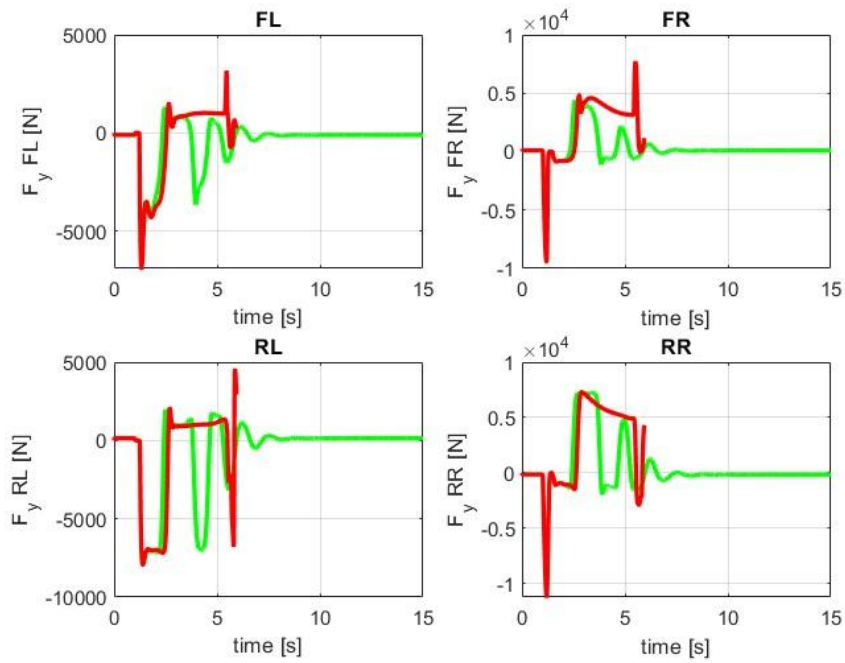


(b)

## State



## Lateral Force



## Phase Plane

By performing a series of simulations, like those whose results are shown in the previous graphs, it is possible to represent the closed-loop stability region of the vehicle in the phase plane.

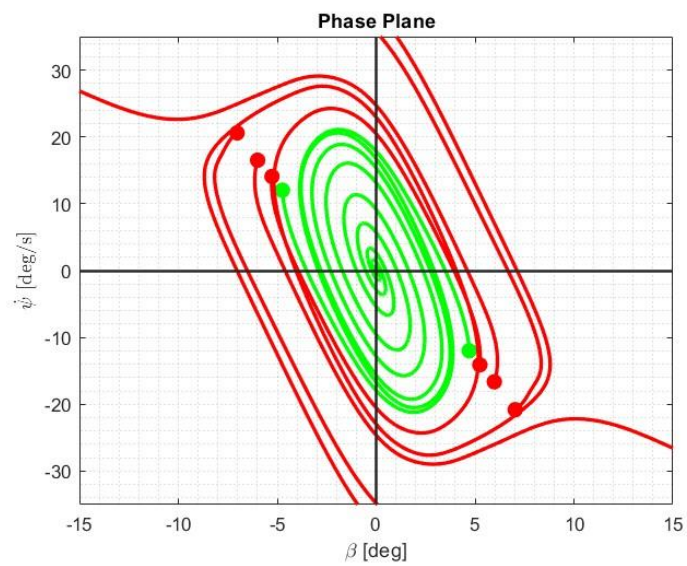


Figure 3.16 : Closed loop phase plane

### 3.5.3. Effect of Steering Actuation Delay

A particularly relevant analysis is the comparison between the stability region obtained in the so-called "fast steering" case and the "slow steering" case. The graph presented below shows that, despite the controller receiving the same information in both cases, the stability region is significantly influenced by the delay  $\tau$ .

This highlights the importance of considering this parameter in control system design, especially regarding the closed-loop stability of the system.

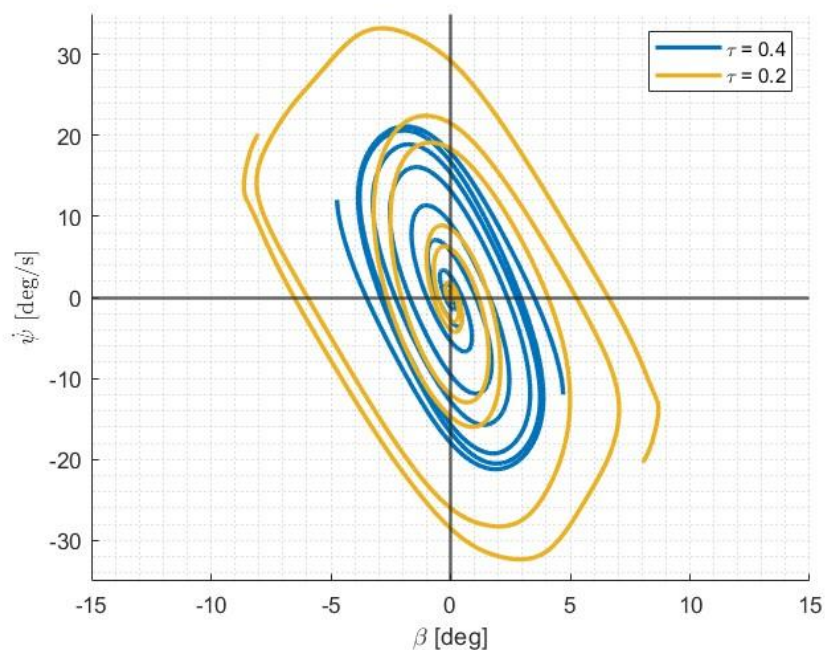


Figure 3.17 : Effect of steering actuation delay

Observing the time behaviour of the state variables in the figure Figure 3.18, we notice the differences in the time required to reach the steady-state condition in the two cases of steering angle actuation delay. As shown in the graph Figure 3.17, the initial points of the states after the disturbance application are different. This is due to what was previously demonstrated, namely that in the case of faster actuation, to be on the edges of the limit cycle, we can shift to higher values of initial conditions. However, as expected, in the case of  $\tau=0.2$ , the settling time is lower compared to the case of  $\tau=0.4$ ,

indicating that when the steering dynamics are slower, more time is required to reach a steady-state condition.

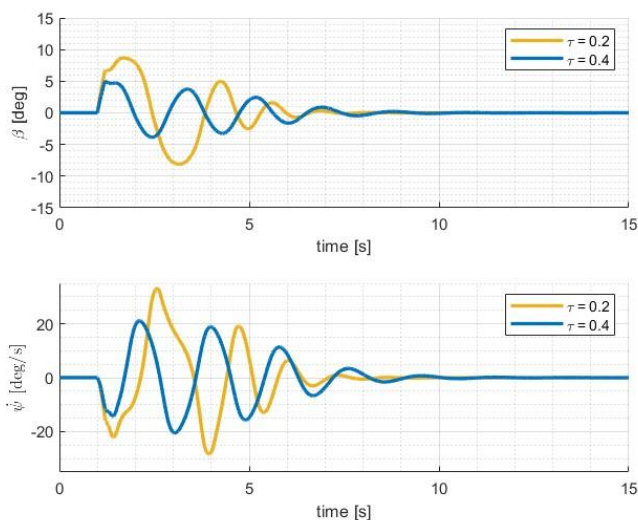


Figure 3.18 : State behaviour compare between different steering actuation delay

The table reports the obtained settling time values.

	$\tau$ [s]	State	Settling time [s]
<b>Fast Steering</b>	0.2	$\beta$	5.42
		$\dot{\psi}$	6.38
<b>Slow Steering</b>	0.4	$\beta$	7.35 [+35%]
		$\dot{\psi}$	8.61 [+35%]

Having discussed the comparison in terms of stability, it is also interesting and necessary to focus on the errors relative to the reference trajectory. Excessively large errors, particularly those related to lateral deviation, indicate the need for wide spaces to ensure successful stabilization. This highlights a critical aspect: the ability of the controller to stabilize the vehicle may become secondary in disturbance conditions that lead to excessive trajectory errors—not only in terms of controller performance but also in terms of safety.

Thus, while the controller can stabilize the vehicle, achieving this behavior requires a wide lane margin, which is often unavailable in real-world scenarios. This consideration can be observed in the following graph.

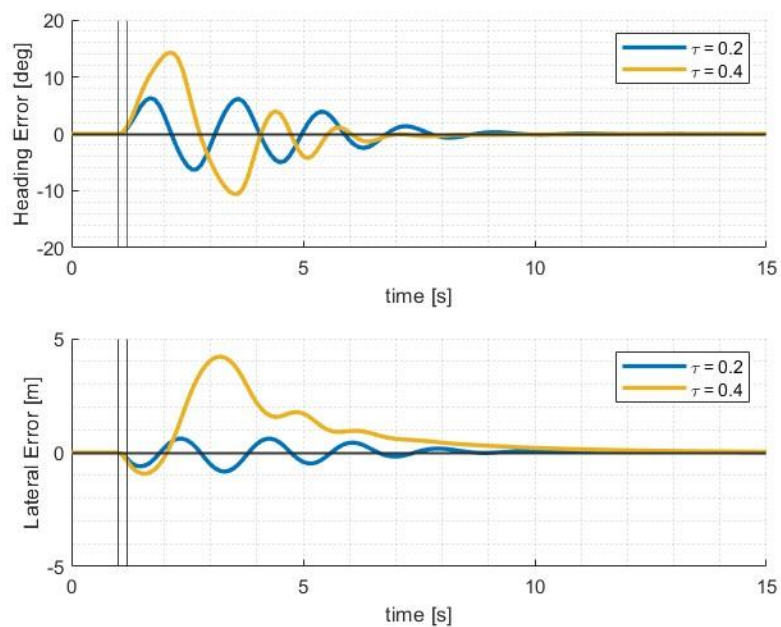


Figure 3.19: Error compare between different steering angle actuation delay

### 3.5.4. Comparison of vehicle stability zone in closed loop and open loop

In the graph below, it is possible to observe the change in the morphology of the stability zone for an oversteering vehicle when transitioning from open-loop conditions to controlled vehicle conditions (i.e., closed-loop). The red area represents the instability zone in the open-loop case, while the light green area indicates the stability zone. Superimposed on these two zones is the dark green area, which represents the stability zone of the vehicle in closed loop when  $\tau = 0.2s$ .

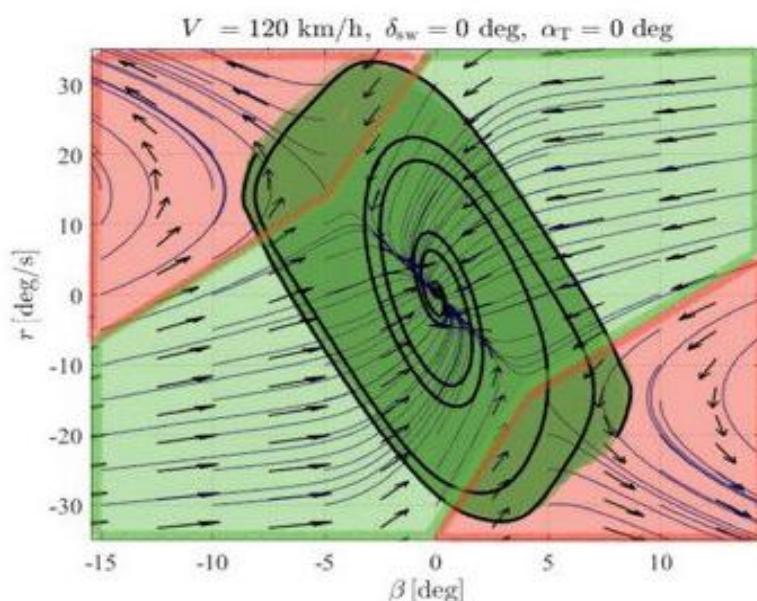


Figure 3.20 : Open-loop vs Closed-loop stability zone

	Closed loop Stability Area
	Open loop Stability Area

From this comparison, it is evident that the change in the stability zone is significant. In particular, the controller is able to stabilize parts of the regions that were previously unstable for the uncontrolled vehicle. This is of great importance in the context of autonomous driving systems. Therefore, it is essential to emphasize that, for vehicle stability control, attention should not only be given to the vehicle's intrinsic stability characteristics but rather to those of the entire vehicle-controller (or driver) system. The maps obtained in this phase can thus be used to assess the stability limits of the controlled vehicle.

## 3.6. Results: UnderSteering Vehicle

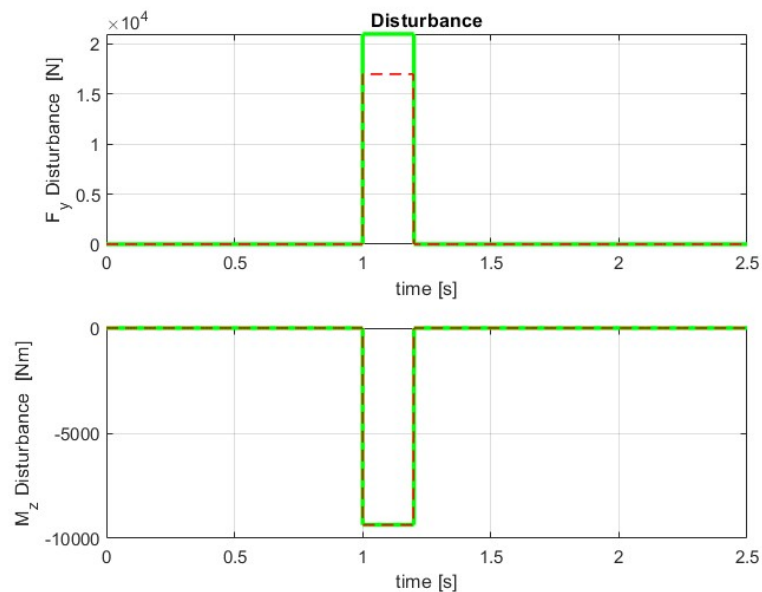
A further analysis was conducted by testing an understeering vehicle to verify the presence of these instability zones in the vehicle-controller system, even in a vehicle that is inherently open-loop stable. For the characterization of the understeering vehicle, as done in 2.5.4, starting from the oversteering vehicle analyzed in this text, the following modifications were made:

- The weight distribution parameters, specifically with a 60% distribution on the front axle.
- The distribution parameters of the anti-roll bars between the front and rear, with 50% allocated to the front bars.

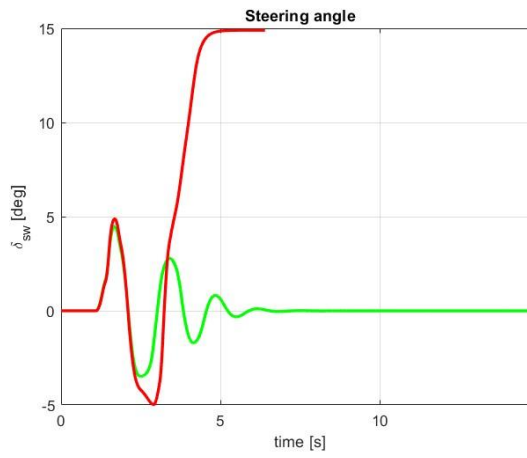
Consistent with these modifications, the new cornering stiffness maps for the understeering vehicle were provided to the controller, following the same approach as in the oversteering case.

### 3.6.1. “Fast steering” Results

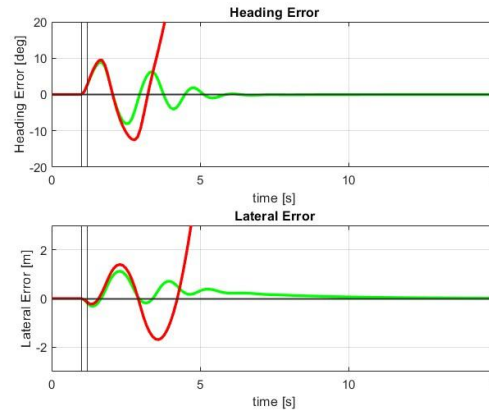
Input: Disturbance



### Steering Angle and Errors

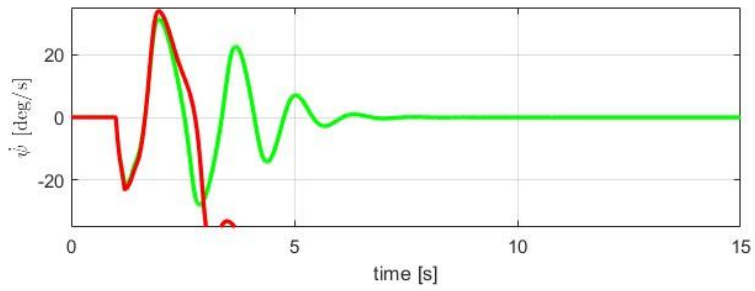
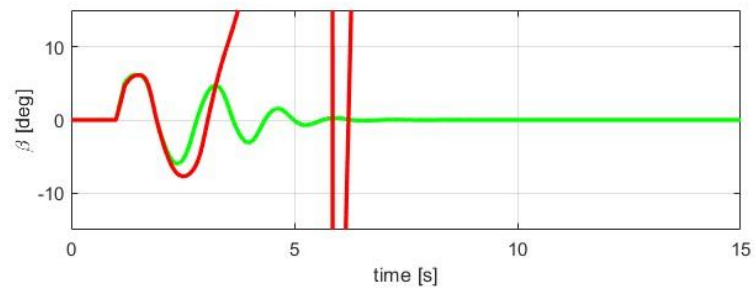


(a)

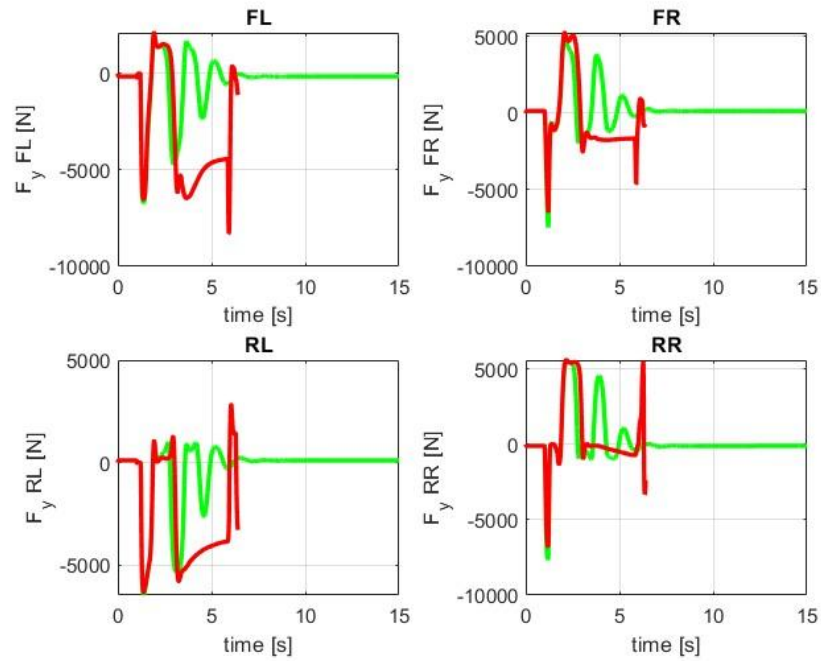


(b)

### State

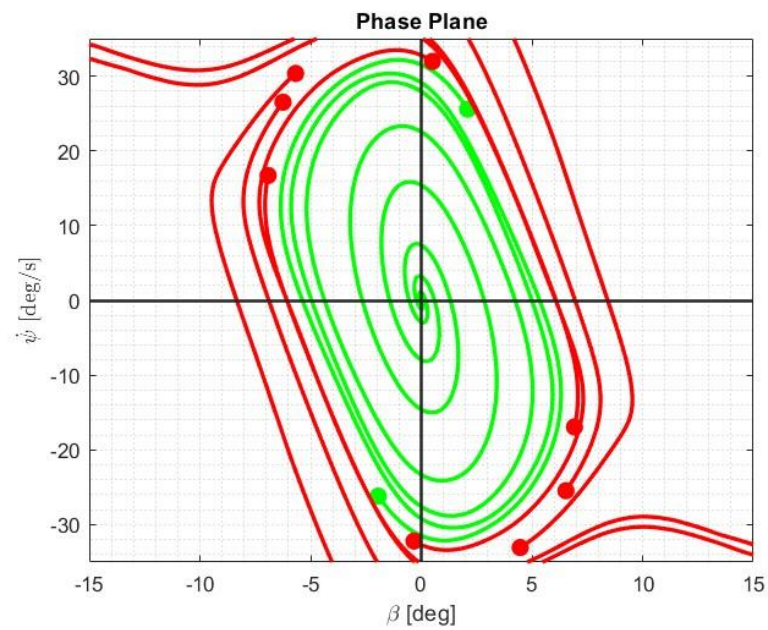


## Lateral Force



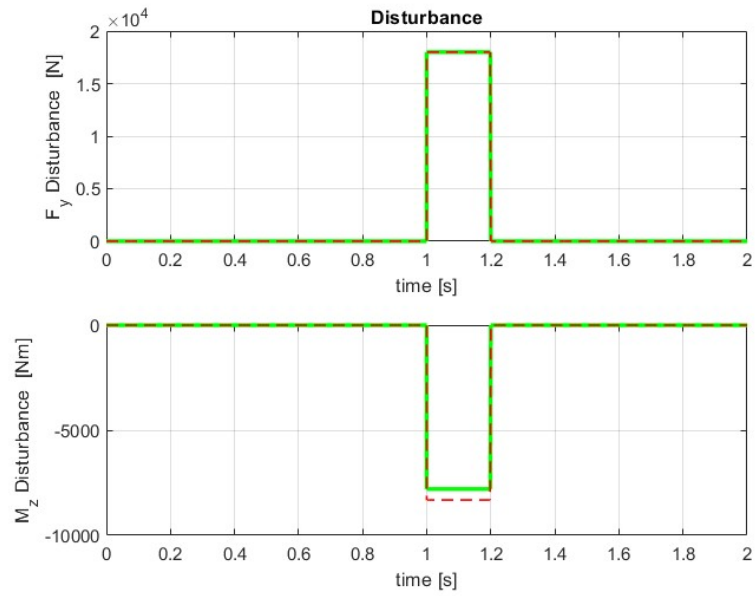
## Phase Plane

By performing a series of simulations, like those whose results are shown in the previous graphs, it is possible to represent the closed-loop stability region of the vehicle in the phase plane.

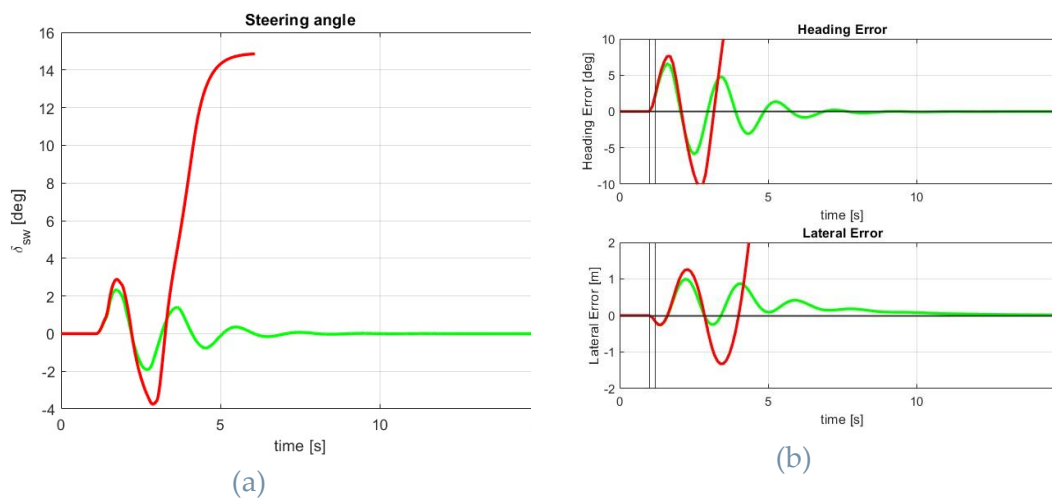


### 3.6.2. "Slow Steering" Results

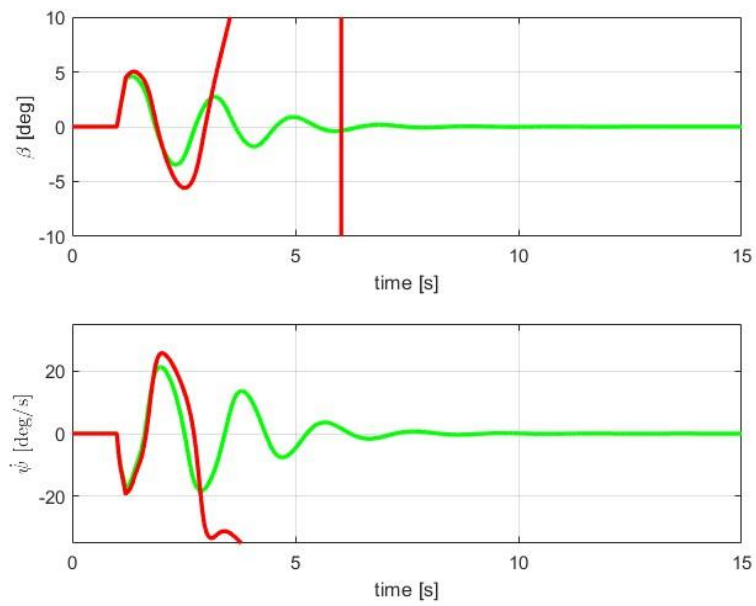
Input: Disturbance



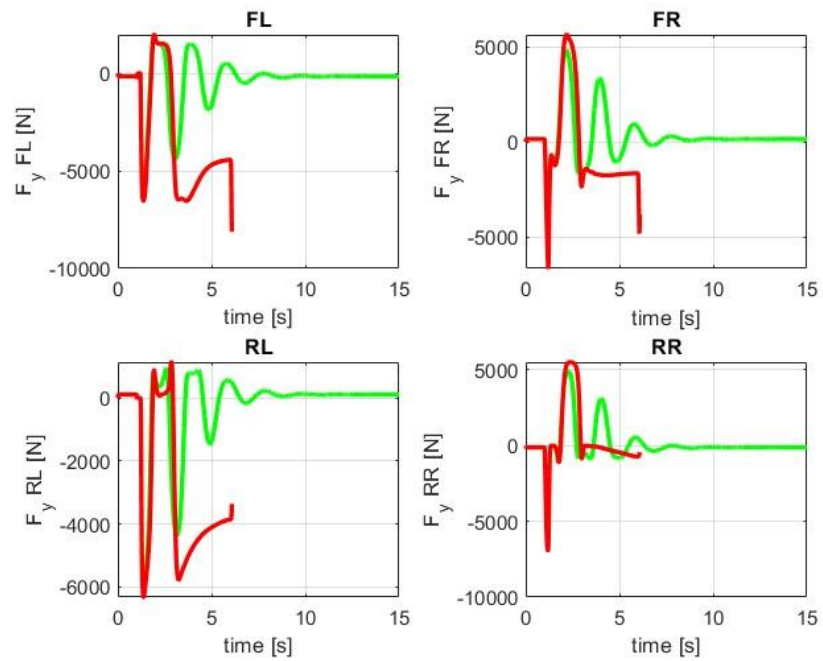
Steering Angle and Errors



## State

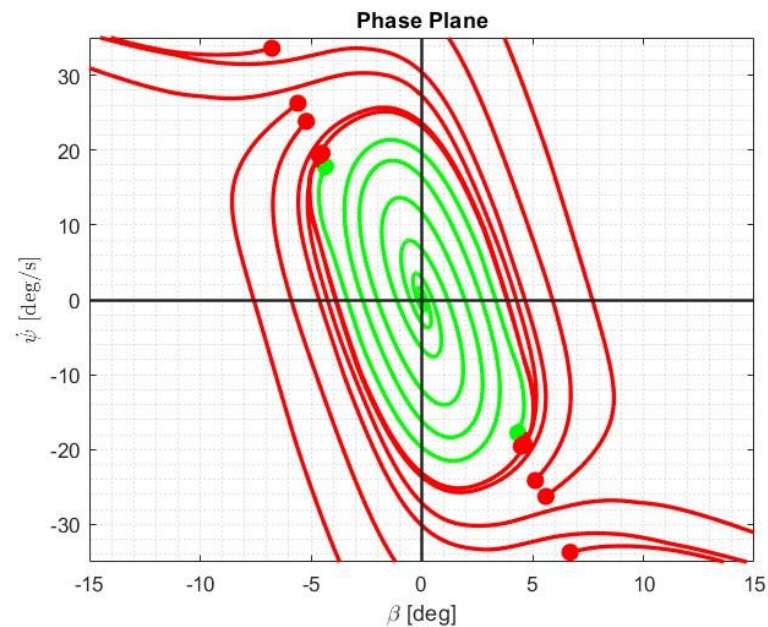


## Lateral Force



## Phase Plane

By performing a series of simulations, like those whose results are shown in the previous graphs, it is possible to represent the closed-loop stability region of the vehicle in the phase plane.



### 3.6.3. Effect of Steering Actuation Delay

As done for the oversteering case in 3.5.3 Effect of Steering Actuation Delay, a comparison of the stability region between the two steering actuation dynamics has been presented. Like the oversteering case, an increase in steering actuation delay results in a reduction of the stability region, as well as a longer time to reach the steady-state condition.

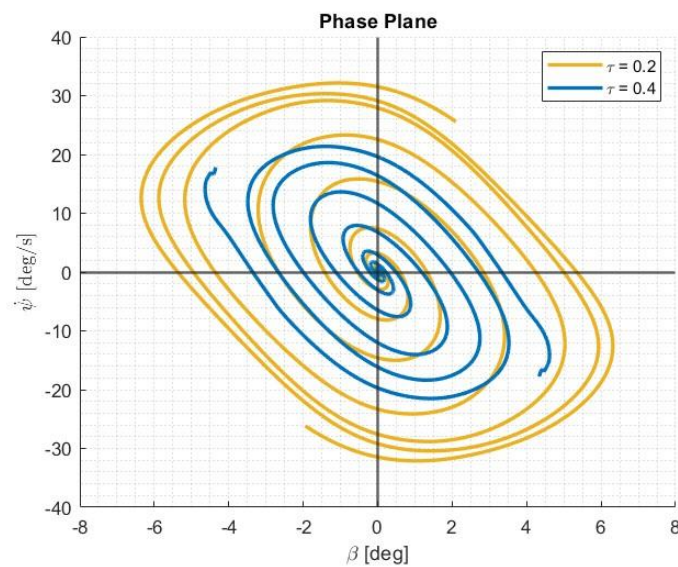


Figure 3.21 : Effect of steering actuation delay

### 3.6.4. Comparison of vehicle stability zone in closed loop and open loop

As done for the oversteering case in 3.5.4, the following graph shows the comparison between the stability region for an understeering vehicle in open-loop versus the controlled (closed-loop) case. Like the oversteering scenario, the case with  $\tau=0.2$  has been selected for visualization.

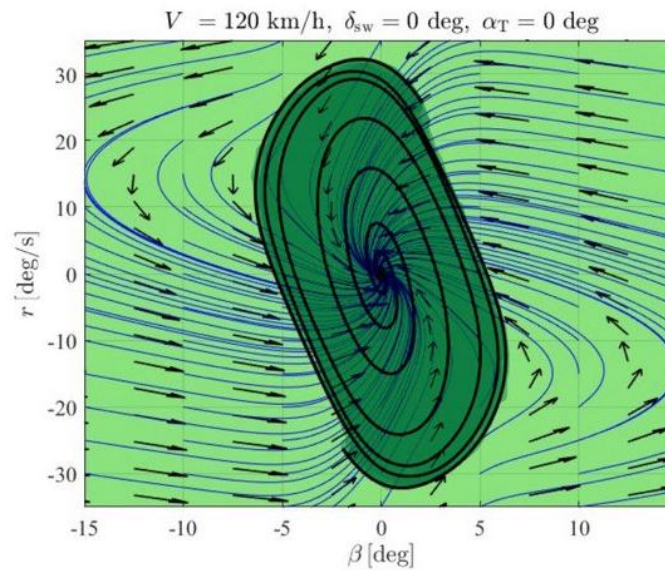


Figure 3.22 : Open-loop vs Closed loop stability compare

	Closed loop Stability Area
	Open loop Stability Area

### 3.7. Oversteering vs Understeering

An important comparison at this stage is between the two stability regions identified for the understeering and oversteering vehicle configurations. The following graph presents the phase plane comparison.

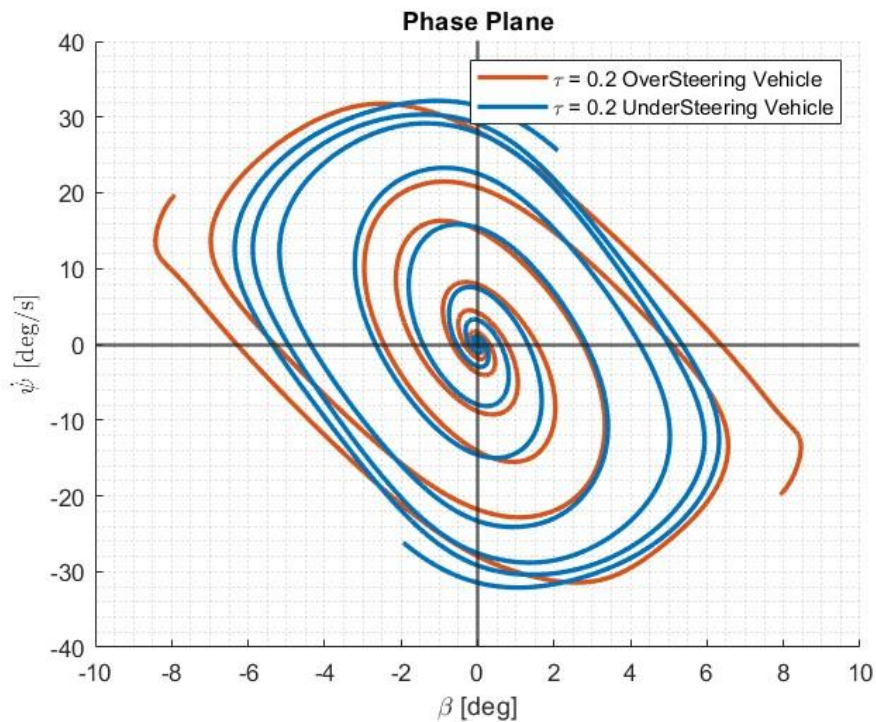


Figure 3.23 : Oversteering vs Understeering stability zone

As observed in the graph, the size of the stability regions in both cases is quite comparable. This leads to an important consideration: the controller plays a crucial role in defining the stability region, regardless of the vehicle's inherent nature. However, this is true only if the controller has real-time knowledge of the vehicle's operating conditions. Specifically, in both cases, the controller has updated information on the cornering stiffness, allowing it to better manage the plant.

In conclusion, by studying the stability of the closed-loop system, we can affirm that if the controller is well-informed about the vehicle's operating conditions and is properly designed, the understeering or oversteering nature of the vehicle does not necessarily represent a constraint. That said, it is important to remember that the magnitude of disturbances differs between the two vehicle types, as do the trajectory tracking errors.

### 3.8. Simulation Scenario: Constant Curved trajectory

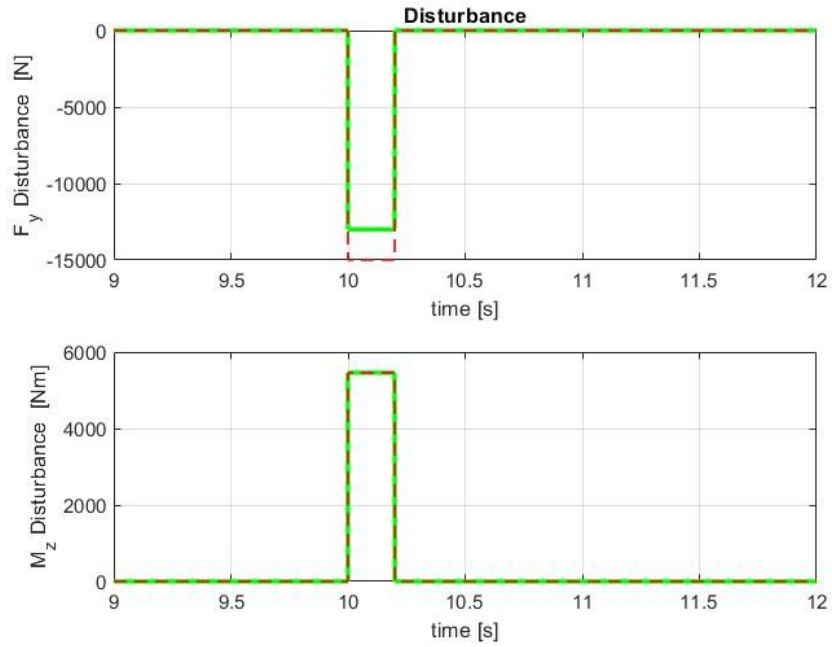
The implemented simulation scenario involves a curvilinear trajectory (and thus a curvilinear reference trajectory for the controller) with a constant radius, traveled at a constant speed of  $V = 120 \text{ km/h}$ . The goal of this second type of maneuver is to evaluate the stability zone, starting from a condition of non-zero lateral acceleration. By maintaining the vehicle at a constant speed and testing various turning radius, it is clearly possible to begin with different lateral acceleration conditions.



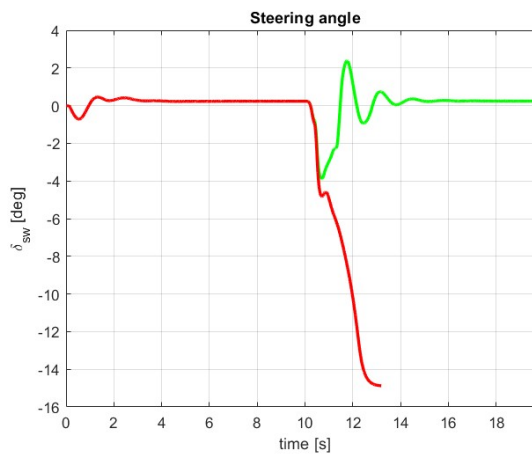
The disturbance was implemented as described earlier, with the precaution this time of disturbing the system only once a steady-state condition has been reached. Nonetheless, the duration of the disturbance remains the same as in the previous cases, equal to  $\Delta t = 0.2\text{s}$ .

### 3.8.1. "Slow Steering" Results

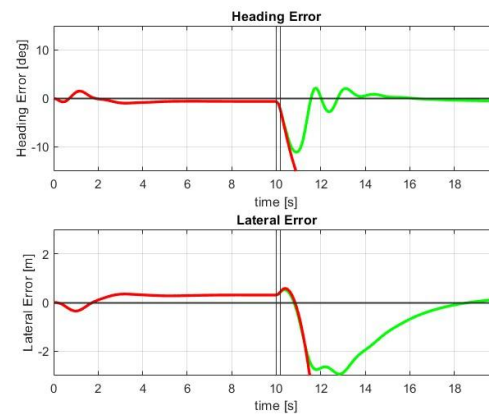
Input: Disturbance



Steering Angle and Errors

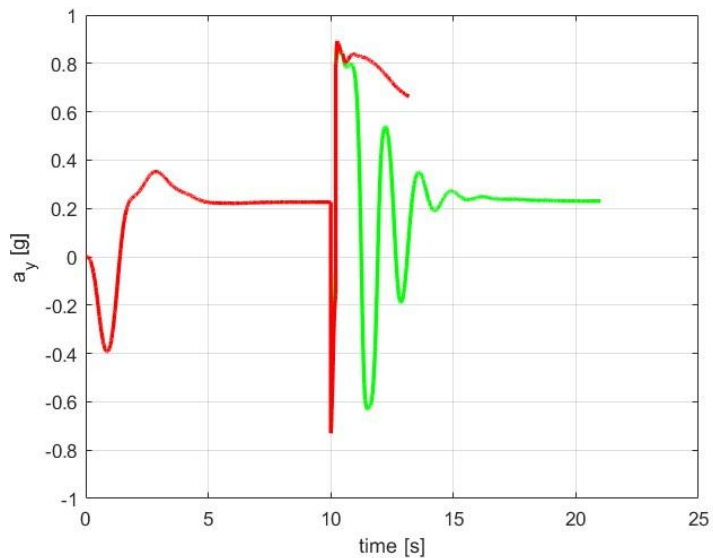


(a)

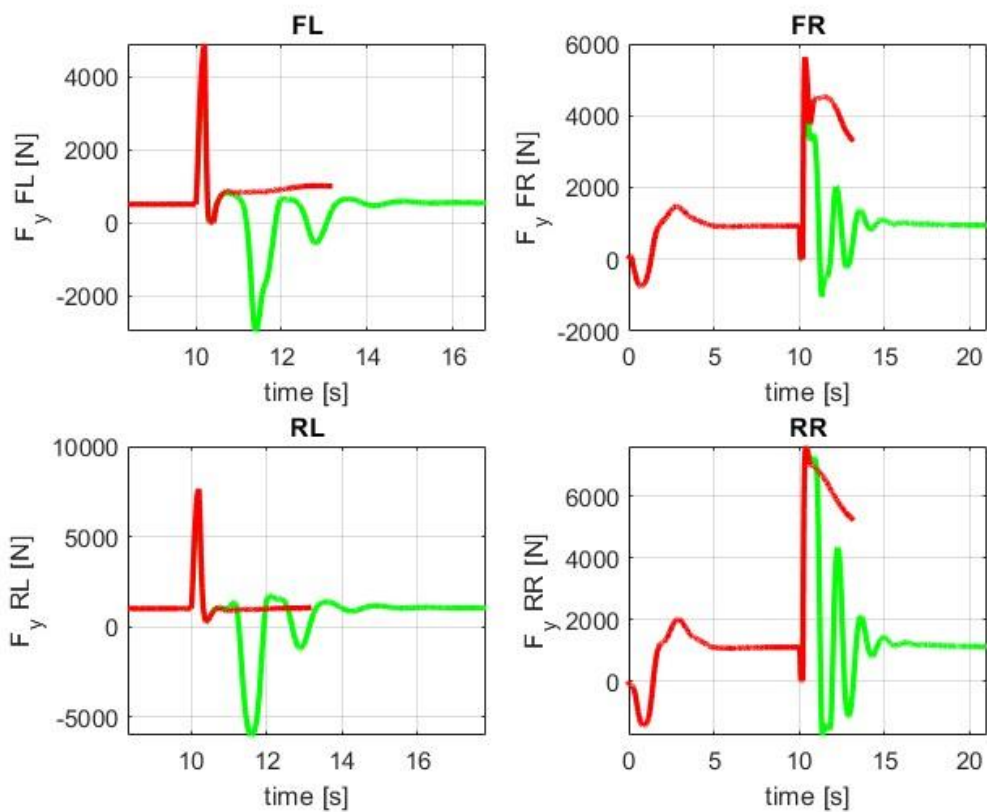


(b)

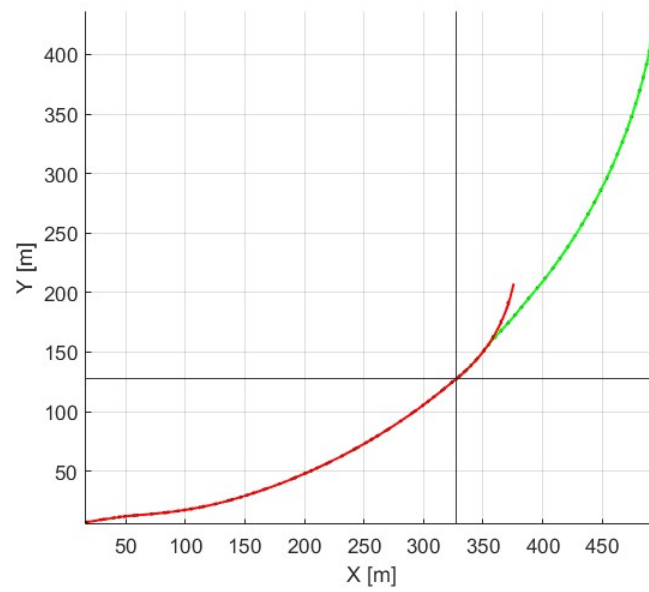
Lateral Acceleration



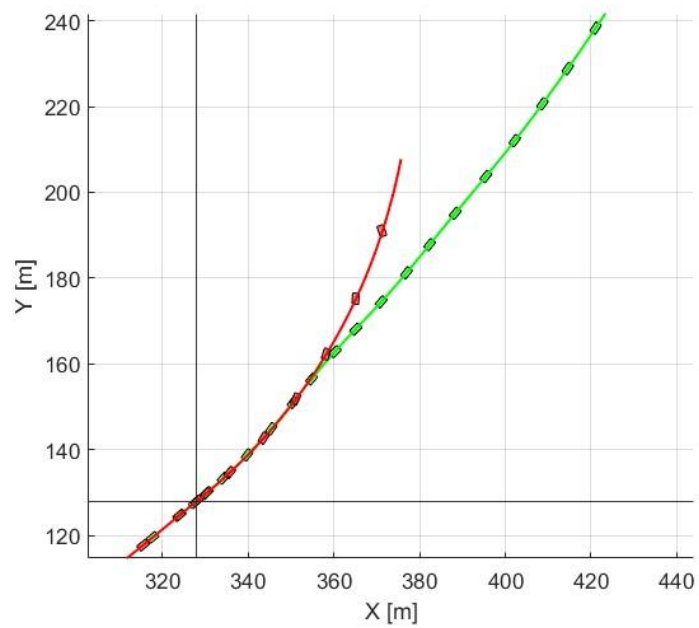
Force



## Trajectory

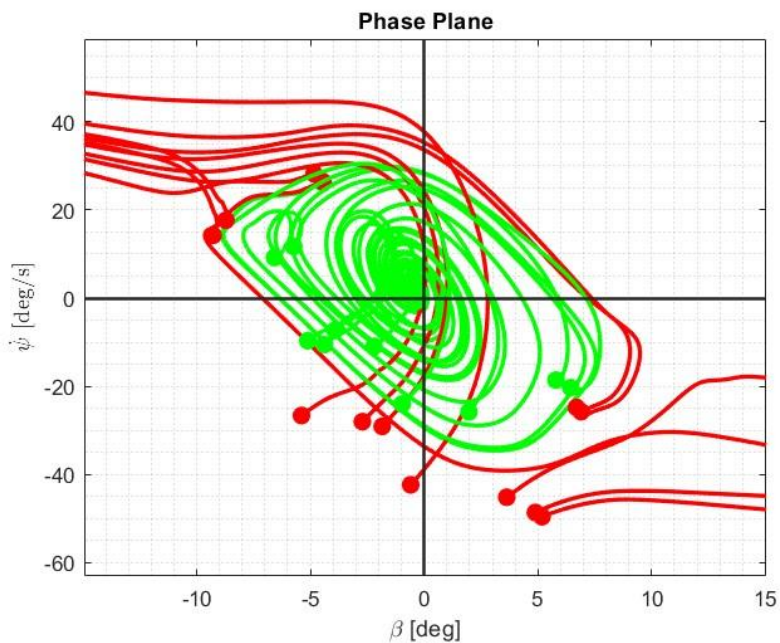


A zoom of the trajectory after the disturbance application is reported in the following graph.

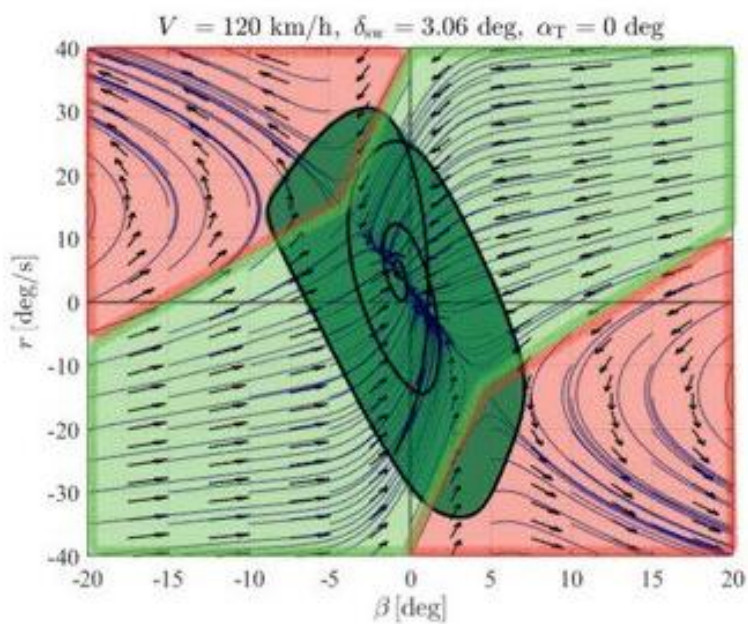


## Phase Plane

By performing a series of simulations, like those whose results are shown in the previous graphs, it is possible to represent the closed-loop stability region of the vehicle in the phase plane.



### 3.8.2. Comparison of vehicle stability zone in closed loop and open loop



## 4 Complete Model performance

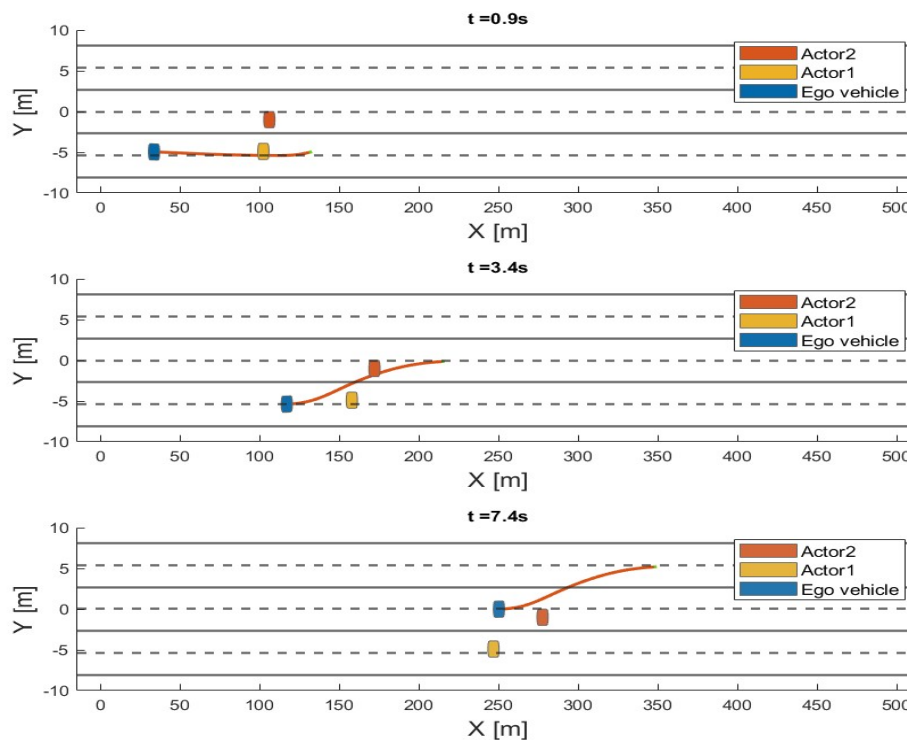
In order to highlight the importance of the analyses carried out in this text, a critical simulation scenario for the complete autonomous driving model has been analysed.

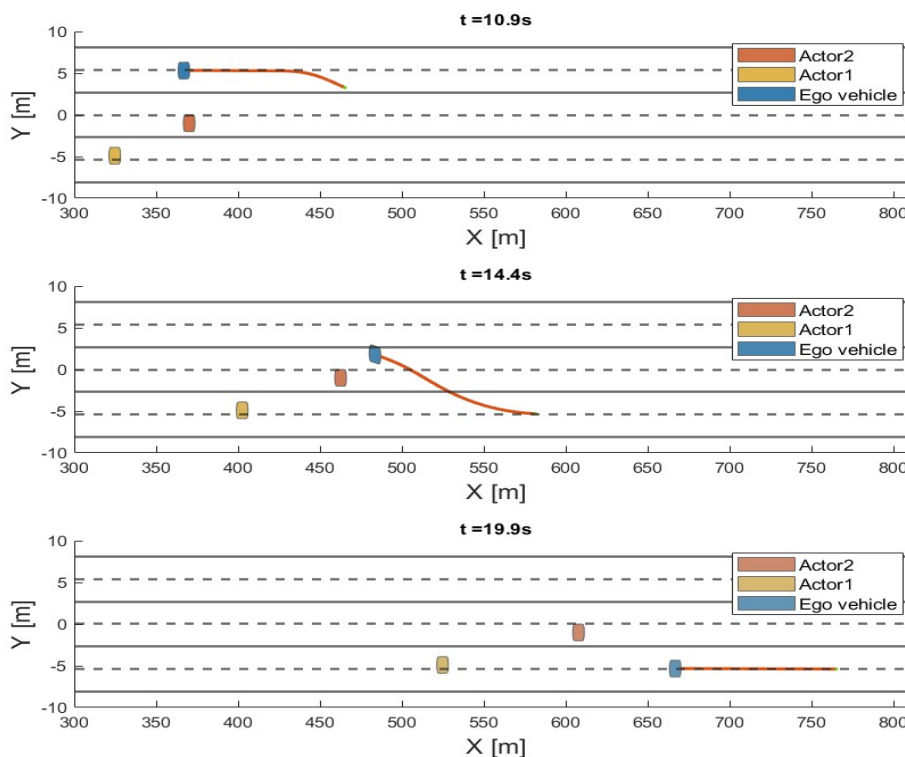
First, the simulation scenario under examination will be presented. Secondly, the cases examined will be highlighted, and finally, a comparison of the controller's performance in the various cases will be conducted.

### 4.1. Scenario: Straight road double overtaking

#### 4.1.1. Scenario description

The scenario under consideration consists of a straight trajectory on a highway with three lanes. There are three actors: an Ego vehicle, represented in blue, which serves as the reference vehicle for the analysis, and two Actor vehicles. To better understand the temporal evolution of the maneuver, several frames of the maneuver are shown in the following figures.





Referring to the previous figures, the Ego vehicle begins its maneuver ( $t = 0.9s$ ) in the right lane at a constant speed of 120 km/h. Along its path, it will encounter two vehicles: Actor1, represented in orange, which is in the same lane at a speed of 80 km/h, and Actor2, represented in red, positioned in the middle lane at a speed of 90 km/h. The third lane is left clear to allow the Ego vehicle to perform a double overtaking maneuver by executing two consecutive lane changes.

After overtaking both vehicles ( $t = 3.4s$ ,  $t = 7.4s$ ), the Ego vehicle will proceed with the maneuver to return to its original right lane ( $t = 14.4s$ ).

## 4.2. Analysed cases

To evaluate the system's performance, three cases will be analyzed. As widely highlighted in the conclusions of the previous chapters, the vehicle's operating conditions play a crucial role in stability. In this analysis, we will focus on the importance and effect of introducing variable axle characteristic maps depending on the examined conditions.

The parameter that will be varied is the road inclination, and two cases with a non-zero inclination will be examined. Specifically:

- **Case 1 (as shown in the table):** The controller is unaware of the vehicle's current operating conditions and thus bases its command

execution dynamics on nominal axle cornering stiffness values, assuming a flat road.

- **Case 2 (as shown in the table):** The road still has a non-zero inclination, but the controller is assumed to have sensors capable of evaluating the road inclination parameter. Additionally, it is considered sufficiently fast to update the axle characteristic maps accordingly.

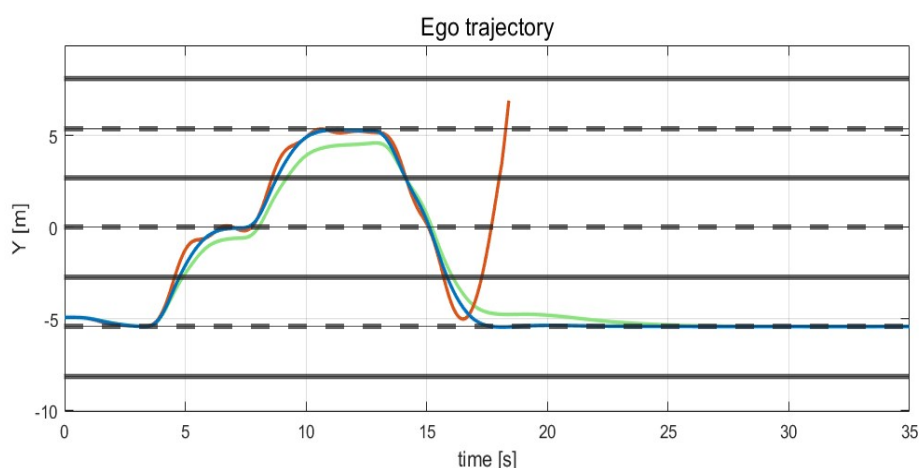
A summary table of the analyzed cases is presented below. The last column of this table also shows the reference colors for each case, which correspond to the colors used in the graphs in the next section where the results will be presented.

	$i$ [%]	Corn. Stiff. Update	Reference Color
<i>Case 0</i>	0	nominal	Blue
<i>Case 1</i>	-30	NO	Red
<i>Case 2</i>	-30	YES	Green

### 4.3. Results

The results for the three previously described cases are presented in this section.

#### Trajectory

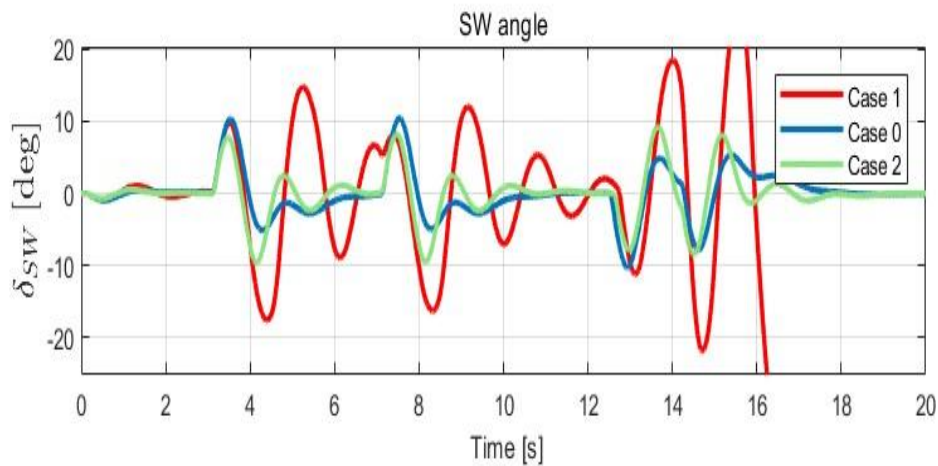


### Steering wheel Angle

From the steering angle graph for the three cases, it is evident that in **Case 1**, where the controller does not receive an update on the road inclination value, the initial steering angle is the same as in **Case 0**. Since the controller follows the same trajectory at the same speed while being unaware of the new inclination conditions, it applies the same steering input as in the flat road scenario.

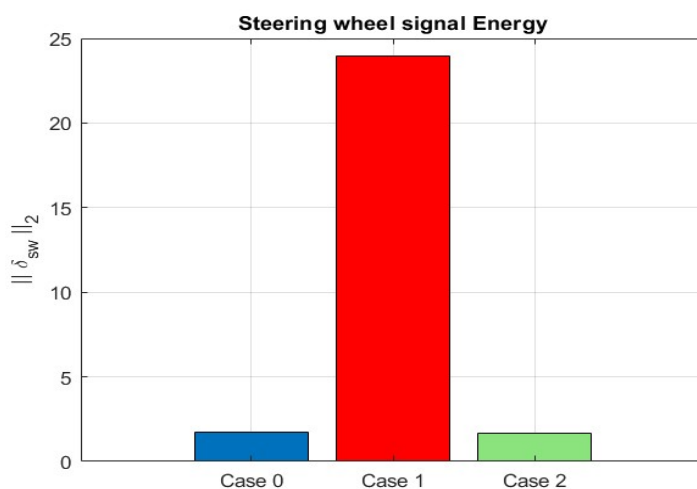
However, in **Case 1**, a non-zero road inclination is introduced—specifically, an inclination that significantly reduces the vehicle's stability zone, as previously discussed. As a result, the chosen steering angle induces oscillations that are not present in the reference case (**Case 0**).

In contrast, in **Case 2**, where the axle cornering stiffness values are updated to match the vehicle's operating conditions, the controller can anticipate the increased instability of the vehicle. Given the same reference trajectory and speed, it applies a lower steering angle. This approach allows the controller to keep the vehicle within a stable operating zone, despite the highly critical scenario under consideration.



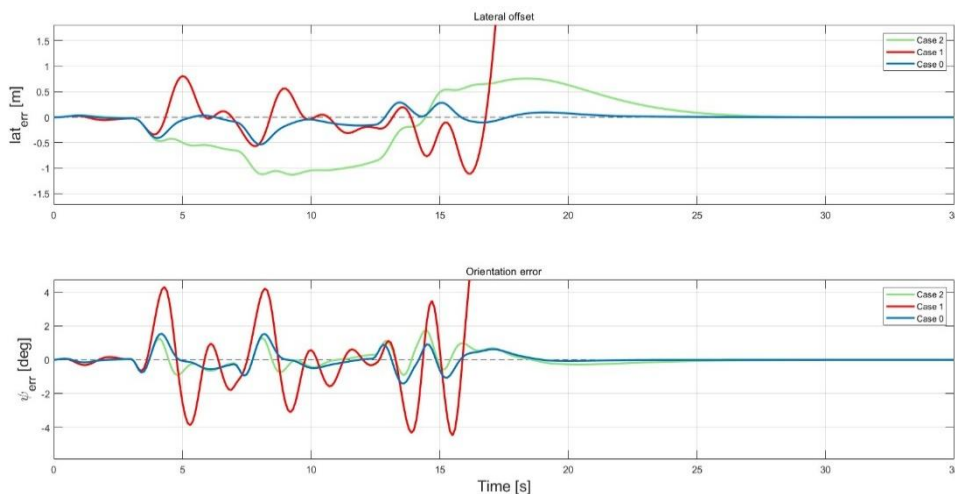
The L2 norm of the signal is also reported, where the result represents the energy of the signal itself. In the case of the steering angle, a lower energy value is beneficial both in terms of driver comfort and in terms of the energy required for steering actuation.

By updating the axle stiffness maps, it is possible not only to maintain the maneuver within a stable execution range but also to make the required energy comparable between the less critical case (with zero road inclination) and the more critical case (with a non-zero road inclination).



### Lateral and Orientation Errors

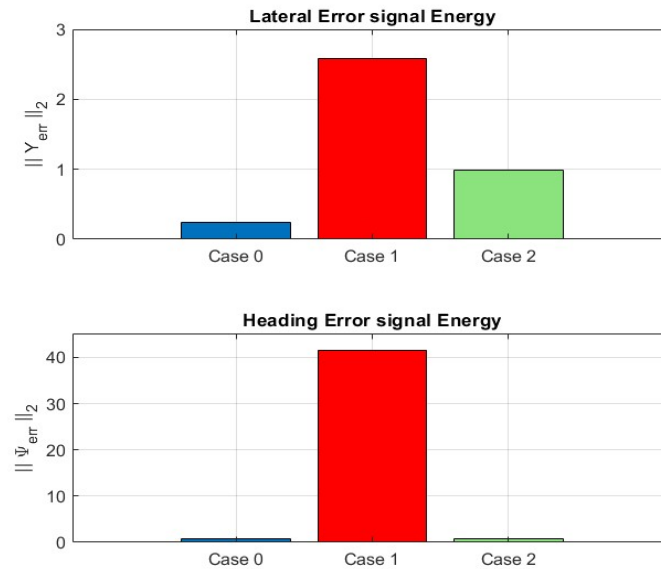
Comparing the errors relative to the reference trajectory, we observe that in the case of updated maps, maintaining vehicle stability requires accepting a higher lateral error relative to the reference trajectory. However, this comes with the advantage of a reduced orientation error, as its oscillations remain more controlled compared to the instability scenario (Case 1).



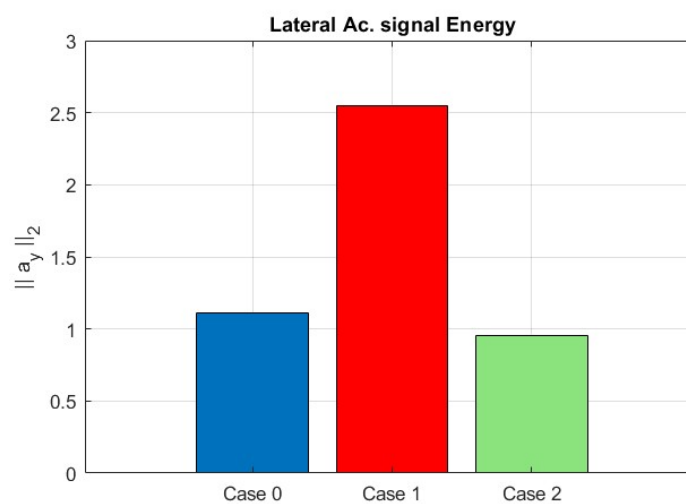
In this case as well, the energy values of both signals are reported to compare the controller's performance in terms of error relative to the reference trajectory.

As seen in the lateral error diagram, the signal energy in Case 2 is still higher than in Case 0, but remains lower than in the unstable scenario (Case 1).

Regarding the vehicle orientation error, the improvements introduced in Case 2 result in energy values comparable to the reference case (Case 0) and significantly lower than in the unstable case.



An additional interesting analysis is presented in the following graph, where the energy of the lateral acceleration signal is examined. This signal serves as an indicator of passenger comfort during the maneuver.



## Stability

It is also interesting to focus on the vehicle's stability zone. Consistent with what was discussed in the previous chapter, the phase diagrams obtained in Case 1 and Case 2 are presented below. Additionally, the zone defined as the vehicle's stability zone in the previous chapter is highlighted.

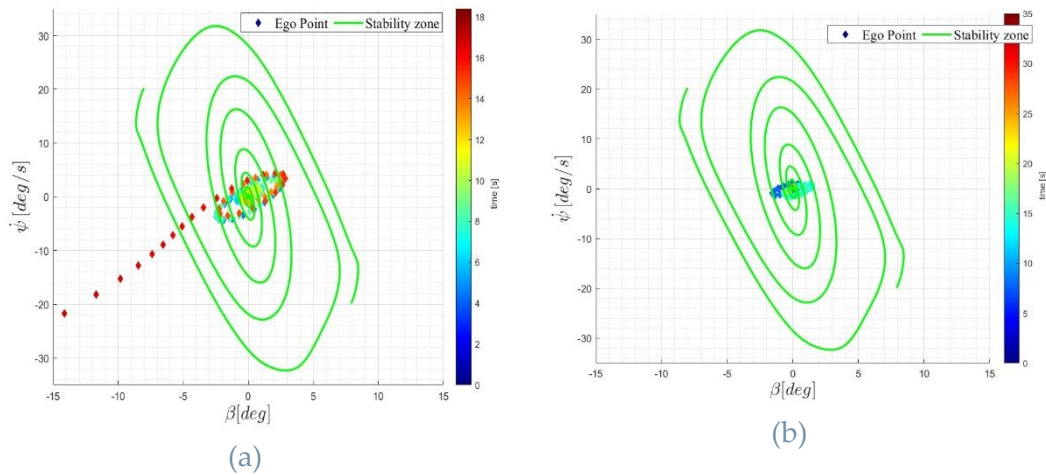


Figure 4.1 : Phase plane Case 1 (a) Case 2 (b)

From this last analysis, updating the axle Cornering stiffness maps input to the controller is of relevant importance for the maneuver's stability. It allows the controller to implement commands that are consistent with the vehicle's stability zone.

In Case 1, at a certain point during the maneuver, the vehicle's state conditions fall outside the closed-loop stability zone. From that moment onward, the controller is no longer able to stabilize the vehicle.

## 5 Conclusions

In this work, a comprehensive analysis of the vehicle's behavior across its entire operating range has been conducted. The importance of characterizing vehicle dynamics was further validated through the graphical phase-plane method, which proved to be an effective tool for studying nonlinear phenomena.

By combining these two elements, it became possible to better predict the vehicle's response under varying operating conditions. Specifically, by generating and updating axle stiffness maps as inputs to a model-based predictive controller, significant improvements were achieved in terms of stability, passenger comfort, and actuation energy efficiency.

Additionally, the study emphasized the critical influence of the driver (or alternatively, the controller) on the vehicle's stability zone. It was shown that even inherently stable vehicles in open-loop conditions—such as understeering vehicles—can exhibit instability depending on the controller's behavior. This finding highlights the crucial role of both controller responsiveness and driver skill in ensuring safe operation. A sufficiently fast and well-calibrated controller is necessary to compensate for instability phenomena, which is fundamental from a safety perspective.

Summary of the Thesis Contributions:

- Linearized models remain valuable tools for understanding local stability and developing real-time control strategies.
- Phase-plane analysis provides a graphical representation of vehicle stability and instability regions, offering insights into how external disturbances or extreme maneuvers push the vehicle beyond safe limits.
- Bifurcation analysis helps identify critical stability thresholds, revealing transition points between controllable and uncontrollable behavior.
- The stability of a vehicle in open-loop conditions is significantly influenced by the driver or controller, making closed-loop analysis essential for realistic stability assessments, particularly in the development of autonomous driving systems.

## 5.1. Future developments

The limitations encountered in this study provide valuable insights into potential future developments, including:

- **Refinement of Simulation Models:** While the models used in this work are expected to provide good approximation compared to multibody simulations, conducting the same analyses using more detailed simulation models could offer further validation. Comparing the results obtained in this study with those from high-fidelity simulations would help emphasize the relevance of the proposed methods.
- **Improved Bifurcation Analysis Methodology:** A more precise methodology for bifurcation analysis could be explored, such as dynamically updating the equilibrium search starting point at each iteration. This could be guided by the insights gained from phase-plane trajectory representations, potentially improving the identification of stability transition points.
- **Extension of Closed-Loop Stability Zones:** The closed-loop stability zones could be further expanded by considering additional phase-plane representations that incorporate different system states alongside those analyzed in this study. Additionally, the validity of these stability zones could be strengthened through track tests or high-fidelity driving simulators, providing real-world validation of the theoretical findings.
- **Evaluation of Controller Performance Without V2X Infrastructure:** In the vehicle simulations with a controller, a V2X infrastructure was assumed to enable communication between the vehicle and its environment. However, it would be valuable to assess the feasibility and effectiveness of the controller performance improvement methods presented in this study without this assumption. By integrating onboard sensors instead of V2X connectivity, it would be possible to evaluate whether real-time map updates for axle cornering stiffness adaptation are practically achievable within the system constraints.





## Bibliography

- [1] W. F. a. D. L. M. Milliken, *Race Car Vehicle Dynamics*. Warrendale, SAE, 1995. Print., 1995.
- [2] G. a. A. G. Genta, *Road Vehicle Dynamics : Fundamentals of Modeling and Simulation.*, Hackensack, NJ: World Scientific Publishing,, 2017.
- [3] E. G. M. M. G. V. M. Galvagno, “ “A Methodology for Parameter Estimation of Nonlinear Single Track Models from Multibody Full Vehicle Simulation,”,” *SAE Technical Paper*, 2021.
- [4] S. H. Strogatz, *Non Linear dynamics and Chaos*, Taylor & Francis, 2015.
- [5] L. X.-s. S. S.-m. L. H.-f. G. R. & L. L. Zhang Hao, “Phase Plane Analysis for Vehicle Handling and Stability, *International Journal of Computational Intelligence Systems*,” 2011.
- [6] X. Wang, W. Li, F. Zhang, Z. Li and W. Bao, “Research on the Vehicle Steering and Braking Stability Region,” *Appl. Sci.* , 2023.
- [7] Zhewei Zhu, Xiaolin Tan, Yechen Qin, Yiwei Huang e Ehsan Hashemi, “A survey of Lateral Stability Criterion and Control application for Autonomous Vehicles,” *Ott.* 2023.
- [8] G. M. & C. P. Fabio Della Rossa, “Bifurcation analysis of an automobile model negotiating a curve,” *Vehicle System Dynamics*,, 2012.
- [9] G. P. G. D. R. F. G. M. Mastinu, “How Drivers Lose Control of the Car,” *SAE Int. J. Veh. Dyn., Stab.*, 2024.
- [10] G. E. ., Z. L. Vella L., *Simulazione di scenari di guida complessi per lo studio di un sistema ADAS di sorpasso automatico*, Torino, 2024.
- [11] G. Rill and A. A. Castro, *Road Vehicle Dynamics : Fundamentals and Modeling whit MATLAB*, Taylor & Francis Group, 2020.

- [12] K. S. & T. T. Y. SHIBAHATA Chief Engineer, "Improvement of Vehicle Maneuverability by Direct Yaw Moment Control," 1993.
- [13] A. S. a. P. G. Leonardo De Novellis, "Design and comparison of the handling performance of different electric vehicle layouts".
- [14] Jazar, Vehicle dynamics: Theory and application, Springer.
- [15] G. Tian, Y. Jia, Z. Chen, Y. Gao, S. Wang, Z. Wei, Y. Chen and T. Zhang, "Evaluation on Lateral Stability of Vehicle: Impacts of Pavement Rutting, Road Alignment, and Adverse Weather," *Appl. Sci.*, p. 13, 2023.
- [16] M. R. R. R. M. T. & F. T. Flavio Farroni, "A combined use of phase plane and handling diagram method to study the influence of tyre and vehicle characteristics on stability," *Vehicle System Dynamics*, 2013.
- [17] F. D. R. . G. P. . M. G. . Fainello, "Global stability of road vehicle motion with driver control. Gianpiero Mastinu".









## List of Figures

Figure 0.1:Flow chart cornering stiffness computation.....	16
Figure 0.2: Flow chart equilibrium points open-loop stability analysis .....	17
Figure 1.1: Free-body diagram of the single-track model.....	18
Figure 1.2 : Simulation Model Block Diagram.....	25
Figure 1.3 : Relaxation Length block Diagram .....	28
Figure 1.4 : Flow Chart Controller Model .....	29
Figure 1.5 :Adaptive MPC flow chart .....	30
Figure 1.6:Example of non-linear tire characteristics .....	32
Figure 1.7 : <i>Pacejka 96</i> model .....	33
Figure 1.8: Fixed Point Classification.....	38
Figure 2.1: Input Ramp Steer.....	40
Figure 2.2: (a) Yaw rate (b) Side slip as function of $ay$ .....	41
Figure 2.3: Side Slip vs Kinematic Side Slip.....	41
Figure 2.4: (a) Lateral Forces (b) Slip Angle as function of time.....	42
Figure 2.5:(a) Lateral Forces (b) Slip Angle as function of $ay$ .....	42
Figure 2.6: Cornering Stiffness.....	43
Figure 2.7: Root-Locus dependent on vehicle speed .....	44
Figure 2.8: Steering angle: Compare whit kinematic value.....	45
Figure 2.9: Understeering and Sideslip Characteristics .....	46
Figure 2.10: Gain .....	47
Figure 2.11:Cornering stiffness .....	49
Figure 2.12: Real part eigenvalues of matrices $A$ .....	49
Figure 2.13: Critical Speed affected by lateral acceleration. ....	50
Figure 2.14: Input.....	51
Figure 2.15: Longitudinal Rear Forces .....	52
Figure 2.16: (a) Front Lateral Forces (b) Rear Lateral Forces.....	52

Figure 2.17 : Slip Angle (a) stable - (b) unstable .....	53
Figure 2.18 : Longitudinal Slip Ratio (a) stable - (b) unstable .....	53
Figure 2.19: (a) lateral acceleration (b) side slip angle.....	54
Figure 2.20:(a) lateral acceleration (b) side slip angle.....	54
Figure 2.21:(a) lateral acceleration (b) side slip angle.....	55
Figure 2.22:(a) lateral acceleration (b) side slip angle.....	55
Figure 2.23: Free body diagram .....	56
Figure 2.24: Normal forces computation, Block diagram .....	57
Figure 2.25: Critical Speed affected by road inclination .....	58
Figure 2.26: Cornering stiffness affected by negative road inclination .....	59
Figure 2.27: Cornering stiffness: Effect in terms of percentage variation.....	59
Figure 2.28:Characteristic curves affected by road inclination .....	60
Figure 2.29: Understeering gradient: effect in terms of percentage variation	60
Figure 2.30: Critical speed affected by road inclination.....	61
Figure 2.31:Critical speed: effect in terms of percentage variation .....	61
Figure 2.32: understeering vehicle root-locus.....	62
Figure 2.33:Understeering to oversteering.....	63
Figure 2.34: Cornering stiffness affected by ax.....	64
Figure 2.35: Cornering stiffness percentage variation.....	65
Figure 2.36:Characteristic curves affected by long. accel.....	65
Figure 2.37: Critical speed affected by long. accel. ....	66
Figure 2.38 : Combinate effect of deceleration and negative road inclination. .....	67
Figure 2.39:Cornering stiffness affected by friction coefficient.....	68
Figure 2.40:Cornering stiffness: Effect in terms of percentage variation.....	69
Figure 2.41:Characteristic curves affected by friction coefficient .....	69
Figure 2.42:Understeering gradient: effect in terms of percentage variation	70
Figure 2.43: Yaw rate characteristic affected by friction coefficient .....	70
Figure 2.44:Critical speed affected by friction coefficient .....	71
Figure 2.45:Critical speed: effect in terms of percentage variation .....	71
Figure 2.46 : Single tyre Lateral Front Forces affected by load transfer.....	72

Figure 2.47 : Single tyre Lateral Rear Forces affected by load transfer .....	72
Figure 2.48 : $F_y \Delta F_z$ compare between nonlinear and tyre model.....	73
Figure 2.49 : Computation of the Front Axle characteristic.....	74
Figure 2.50 : Computation of the Rear Axle characteristic .....	74
Figure 2.51 : Front (a) and Rear (b) Tyre characteristic .....	75
Figure 2.52 : Cornering Stiffness compare between non-linear and tyre model .....	75
Figure 2.53 : (a) Front (b) Rear Cornering Stiffness affected by longitudinal slip .....	76
Figure 2.54 : Sign convention for toe angle. Left: Toe-in, right: Toe-out .....	77
Figure 2.55 : (a) Front (b) Rear Cornering Stiffness affected by toe angle .....	77
Figure 2.56 : Sign convention for camber angle .....	78
Figure 2.57 : (a) Front (b) Rear Cornering Stiffness affected by camber angle .....	78
Figure 2.58 : Global Reference frame (X,Y), Vehicle reference frame (x,y) and Tyre reference frame $x_i, y_i$ .....	80
Figure 2.59: Simulink.....	81
Figure 2.60: $(\beta, \psi)$ .....	82
Figure 2.61: $M_z - (\beta - \beta_0)$ .....	83
Figure 2.62: $M_z - ay$ .....	84
Figure 2.63: Results Comparison between single-track and dual-track .....	86
Figure 3.1: Critical speed affected by lateral acceleration.....	87
Figure 3.2 : Phase Portrait at $V=89$ km/h for two value of steering angle .....	88
Figure 3.3 : Phase Portrait at $V = 155$ km/h for two value of steering angle ...	88
Figure 3.4 : bifurcation analysis stable fixed point (black solid line) unstable fixed point (red and blue dashed line).....	89
Figure 3.5 : Steering Angle bifurcation analysis.....	90
Figure 3.6 : Equilibrium points affected by steering angle .....	90
Figure 3.7 : Equilibrium Point affected by road inclination .....	91
Figure 3.8 : Equilibrium points affected by longitudinal acceleration.....	92
Figure 3.9 : Equilibrium points affected by longitudinal acceleration.....	92
Figure 3.10: Equilibrium Point affected by adherence coefficient .....	93

Figure 3.11 : Adhesion coefficient Bifurcation Analysis .....	93
Figure 3.12 : Example of Stability area previously considered .....	95
Figure 3.13 : Example of stability area definition.....	96
Figure 3.14 : Example of stability area over vector field .....	96
Figure 3.15: Closed loop phase plane .....	104
Figure 3.16 : Closed loop phase plane .....	106
Figure 3.17 : Effect of steering actuation delay .....	107
Figure 3.18 : State behaviour compare between different steering actuation delay.....	108
Figure 3.19: Error compare between different steering angle actuation delay .....	109
Figure 3.20 : Open-loop vs Closed-loop stability zone.....	110
Figure 3.21 : Effect of steering actuation delay .....	116
Figure 3.22 : Open-loop vs Closed loop stability compare .....	117
Figure 3.23 : Oversteering vs Understeering stability zone.....	118
Figure 4.1 : Phase plane Case 1 (a) Case 2 (b) .....	130

## List of Tables

Table 2.1: Vehicle Data .....	39
Table 2.2: Ramp Steer parameters. ....	40
Table 2.3: Cornering stiffness affected by road inclination .....	57
Table 2.4: understeering to oversteering .....	63
Table 5 . Steering actuation delay .....	101









